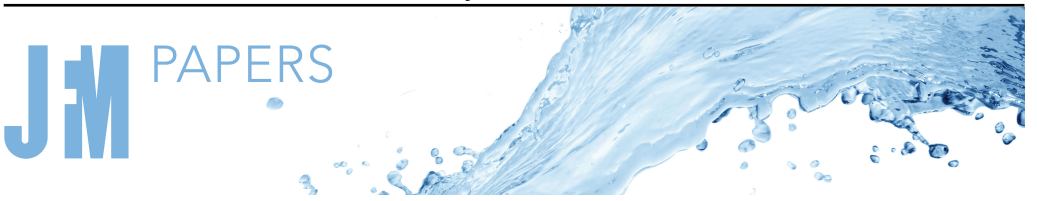
J. Fluid Mech. (2026), *vol.* 1028, A27, doi:10.1017/jfm.2025.11051



On the algebraic stretching dynamics of variable-density mixing in shock–bubble interaction

Xu Han[1], **Bin Yu**[1,2,3] **and Hong Liu**[1,3]

[1]School of Aeronautics and Astronautics, Shanghai Jiao Tong University, Shanghai 200240, PR China

[2]Sichuan Research Institute, Shanghai Jiao Tong University, Sichuan 100190, PR China

[3]J.C. Wu Center for Aerodynamics, School of Aeronautics and Astronautics, Shanghai Jiao Tong University, Shanghai 200240, PR China

Corresponding authors: Bin Yu, kianyu@sjtu.edu.cn; Hong Liu, hongliu@sjtu.edu.cn

(Received 16 January 2025; revised 24 October 2025; accepted 8 December 2025)

The mixing mechanism within a single vortex has been a theoretical focus for decades, while it remains unclear especially under the variable-density (VD) scenario. This study investigates canonical single-vortex VD mixing in shock–bubble interactions (SBI) through high-resolution numerical simulations. Special attention is paid to examining the stretching dynamics and its impact on VD mixing within a single vortex, and this problem is investigated by quantitatively characterising the scalar dissipation rate (SDR), namely the mixing rate, and its time integral, referred to as mixedness. To study VD mixing, we first examine single-vortex passive-scalar (PS) mixing with the absence of a density difference. Mixing originates from diffusion and is further enhanced by the stretching dynamics. Under the axisymmetry and zero diffusion assumptions, the single-vortex stretching rate illustrates an algebraic growth of the length of scalar strips over time. By incorporating the diffusion process through the solution of the advection–diffusion equation along these stretched scalar strips, a PS mixing model for SDR is proposed based on the single-vortex algebraic stretching characteristic. Within this framework, density-gradient effects from two perspectives of the stretching dynamics and diffusion process are discovered to challenge the extension of the PS mixing model to VD mixing. First, the secondary baroclinic effect increases the VD stretching rate by the additional secondary baroclinic principal strain, while the algebraic stretching characteristic is still retained. Second, the density source effect, originating from the intrinsic nature of the density difference in the multi-component transport equation, suppresses the diffusion process. By accounting for both the secondary baroclinic effect on stretching and the density source effect on diffusion, a VD mixing model for SBI is further modified. This model establishes a quantitative relationship between the stretching dynamics and the evolution of the mixing rate and mixedness for single-vortex VD mixing over a broad range of Mach

© The Author(s), 2026. Published by Cambridge University Press.

https://doi.org/10.1017/jfm.2025.11051 Published online by Cambridge University Press

numbers. Furthermore, the essential role of the stretching dynamics on the mixing rate is demonstrated by the derived dependence of the time-averaged mixing rate $\overline{\langle\chi\rangle}$ on the Péclet number Pe, which scales as $\overline{\langle\chi\rangle} \sim Pe^{2/3}$.

Key words: mixing enhancement, vortex dynamics, shock waves

1. Introduction

Variable-density (VD) mixing, which occurs in fluids with varying densities, is a fundamental phenomenon observed in various contexts, such as the mixing of fluids with different densities in gravitational fields, exemplified by Rayleigh–Taylor instability (Rayleigh 1882; Taylor 1950), the formation of supernova remnants (Kifonidis *et al.* 2006; Müller 2020) and the irreversible transport of salt or pollutants in density-stratified oceanic and atmospheric circulations (Fernando 1991; Wunsch & Ferrari 2004; Caulfield 2021). A notable form of VD mixing occurs at the interface of fluids with different densities when subjected to shock waves, identified as the Richtmyer–Meshkov instability (RMI) (Richtmyer 1960; Meshkov 1969; Brouillette 2002; Zhou 2017*a*,*b*). One typical RMI scenario involves the interaction between a shock wave and a circular gas bubble with a density contrast relative to the ambient gas. Unlike classical single-mode RMI, the high curvature of the density interface introduces strong nonlinear effects, complicating the extension of RM linear theory to such shock–bubble interactions (SBI) (Ranjan, Oakley & Bonazza 2011). As SBI serves as the intrinsic mechanism for supersonic mixing enhancement strategies (Marble 1985; Marble *et al.* 1990; Yang *et al.* 1993, 1994; Yu *et al.* 2020), and has significant applications in areas such as inertial confinement fusion (ICF) (Lindl, McCrory & Campbell 1992) and supernova explosions (Klein, McKee & Colella 1994), understanding SBI has become a central focus in VD mixing research.

With regard to the evolution of flow structures in SBI, Haas & Sturtevant (1987) conducted early experimental studies in a shock tube, revealing that vortex structures in SBI tend to evolve into symmetric or axisymmetric forms at the later stages. Jacobs (1992) utilised planar laser-induced fluorescence (PLIF) to visualise the interaction between a shock wave and a hydrogen gas column, focusing on the resulting flow structures and mixing dynamics. Ranjan *et al.* (2007) systematically investigated SBI at a higher Mach number ($Ma = 2.88$), identifying the formation of secondary vortex rings, which are absent in low Mach number scenarios. Zhai *et al.* (2014) conducted a carefully designed experiment to study shock–interface interactions and successfully captured three distinct types of Mach stem reflections, along with a detailed analysis of the corresponding shock wave system evolution. Ding *et al.* (2017, 2018) examined the morphology of a three-dimensional gas cylinder following interaction with a planar shock. In addition, Liang, Zhai & Luo (2018) investigated the interaction between a strong converging shock wave and an SF_6 gas bubble inside a converging shock tube. From a numerical standpoint, Picone & Boris (1988) performed detailed two-dimensional simulations of SBI, demonstrating flow structures that closely resembled those observed in the experiments by Haas & Sturtevant (1987). With the advancement of numerical techniques such as adaptive mesh refinement and high-order accurate schemes, numerical investigations of SBI have significantly improved in terms of resolution and physical fidelity. Zabusky & Zeng (1998) simulated SBI at $Ma = 5$ and identified the generation of secondary baroclinic vortices. Furthermore, Niederhaus *et al.* (2008) showed that for shock Mach numbers exceeding 5 and Atwood numbers greater than 0.5, the post-shock flow field within SBI transitions into turbulence, rather than remaining governed by vortex structures.

https://doi.org/10.1017/jfm.2025.11051 Published online by Cambridge University Press

In the context of circulation models for SBI, early studies on vorticity distribution led to the development of the first circulation model by Hawley & Zabusky (1989). Building on this foundational research, subsequent studies introduced four types of circulation models: the 'PB model' (Picone & Boris 1988), the 'Yang model' (Yang, Kubota & Zukoski 1994), the 'SZ model' (Sandoval 1995) and the '1D model' (Niederhaus *et al.* 2008). These circulation models were later extended to more complex bubble shapes, including elliptical (Zhang *et al.* 2019), triangular (Zeng *et al.* 2018) and square bubbles (Igra & Igra 2018). Furthermore, these circulation models do not account for viscous effect (Wang *et al.* 2018). By incorporating viscosity into the vorticity transport equation, more accurate vortex models can be developed for complex configurations (Liu *et al.* 2020).

From the perspective of mixing, the mixing evolution in SBI can be conceptually outlined as follows: following shock interaction, the formation of a large-scale primary vortex benefits from the baroclinic vorticity deposition originating from misalignment of the pressure gradient ∇p of the shock and density gradient $\nabla \rho$ from the light/heavy density bubble. Driven by this main vortex, the initially concentrated bubble is tangentially stretched along the interface with the ambient air, leading to an increase in material line length. Simultaneously, as the interface undergoes stretching, the scalar gradient deposited along it is amplified, thereby intensifying molecular diffusion until the bubble is completely mixed with the surrounding air (Ranjan *et al.* 2011). This simplified mixing process reveals that mixing is governed by the coupled actions of stretching and diffusion processes, which is consistent with the one proposed by Meunier & Villermaux (2003) and Villermaux (2019). According to this simplified mixing concept, the material line stretching rate and bubble area serve as the critical parameters characterising mixing, and have been widely used in SBI mixing research. Early experiments conducted by Jacobs (1992) utilised the bubble area to depict the extent of mixing and revealed a constant mixing rate by investigating the temporal derivative of the bubble area ratio. Yang, Kubota & Zukoski (1993) employed the material line stretching rate to characterise the mixing rate, and discovered an exponential stretching of the material line in the early stage of SBI mixing. Subsequent experiments on SBI of SF_6 cylinders using the PLIF technique observed a strong dependence of the exponential stretching rate on the configuration and orientation of the cylinders (Kumar *et al.* 2005), while numerical simulations of mixing in three-dimensional shock spherical interactions employed the bubble volume fraction to describe the evolution of mixedness (Niederhaus *et al.* 2008).

Moreover, mixing is characterised by the molecular diffusion of the mass fraction Y. Therefore, in addition to the material line stretching rate, mixing indicators can also be directly defined in terms of the mass fraction. In a study of single-vortex mixing, Cetegen & Mohamad (1993) introduced the mixedness parameter

$$f = 4Y(1-Y), \tag{1.1}$$

to quantify the extent of mixing, which reaches its maximum when the bubble and surrounding air are in a 1:1 state. The evolution of mixedness f in passive-scalar (PS) mixing, where the density difference is absent, is governed by the following equation:

$$\left(\frac{\partial}{\partial t} + u_j \frac{\partial}{\partial x_j} - \mathcal{D}\frac{\partial^2}{\partial x_j^2}\right) f = 8\mathcal{D}\frac{\partial Y}{\partial x_j}\frac{\partial Y}{\partial x_j}. \tag{1.2}$$

The presence of $\chi = \nabla Y \cdot \nabla Y$ on the right-hand side term of this equation $8\mathcal{D}(\partial Y/\partial x_j)(\partial Y/\partial x_j)$ leads to the definition of the scalar dissipation rate (SDR) (Buch & Dahm 1996)

$$\chi = \nabla Y \cdot \nabla Y, \tag{1.3}$$

https://doi.org/10.1017/jfm.2025.11051 Published online by Cambridge University Press

which represents the mixing rate, and ∇Y denotes the scalar gradient. Subsequent PLIF experiments investigated SDR in shock interactions with SF_6 cylinders, revealing that SDR is primarily concentrated in the bridge structure (Tomkins *et al.* 2008). Li *et al.* (2020) developed a Gaussian model to predict the late-time evolution of SBI based on the mixedness definition. Recognising the differences between VD and PS mixing, Yu, Liu & Liu (2021) introduced the density-accelerated mixing rate. Through an investigation of the scaling behaviour of this mixing rate with respect to the Reynolds number $Re = \Gamma_t/\nu$ and Schmidt number $Sc = \nu/\mathcal{D}$, where Γ_t is the total circulation of the primary vortex, ν is the kinematic viscosity and $\mathcal{D}$ is the Fickian diffusivity, it was discovered that, at a constant Péclet number $Pe = \Gamma_t/\mathcal{D}$, the mixing rate experiences minimal variation with increasing Reynolds number once Re reaches a sufficiently large value. This scaling behaviour was further confirmed in homogeneous isotropic turbulence mixing (Buaria *et al.* 2021). Therefore, extensive research in the field of SBI has provided valuable insights into characterising stretching behaviour and diffusion states from two key perspectives of the mixing process. Despite the widely acknowledged opinion that the stretching process plays the critical role in mixing, the precise connection between the stretching dynamics and VD mixing in SBI has not been established rigorously.

It is necessary to define the stretching rate within a reasonable framework supported by the governing equation for SDR. This equation, derived by Corrsin (1953), Batchelor (1959) and Buch & Dahm (1996), has been widely used to study PS mixing, which involves the mixing of fluids with uniform density. The governing equation is expressed as

$$\left(\frac{\partial}{\partial t} + u_j\frac{\partial}{\partial x_j} - \mathcal{D}\frac{\partial}{\partial x_j^2}\right)\chi = -2\frac{\partial Y}{\partial x_i}S_{ij}\frac{\partial Y}{\partial x_j} - 2\mathcal{D}\frac{\partial}{\partial x_i}\left(\frac{\partial Y}{\partial x_j}\right)\frac{\partial}{\partial x_i}\left(\frac{\partial Y}{\partial x_j}\right), \tag{1.4}$$

where $S_{ij} = 1/2(\partial u_i/\partial x_j + \partial u_j/\partial x_i)$ is the symmetric strain-rate tensor. The two terms on the right-hand side of the equation are referred to as the stretching term and the diffusion term, respectively. The stretching term reflects the intrinsic mechanism by which the strain field stretches the magnitude of the scalar gradient ∇Y, thereby driving SDR evolution. This term can be further investigated by its orthogonal decomposition form (Ashurst *et al.* 1987; Vincent & Meneguzzi 1991; Dresselhaus & Tabor 1992), given by

$$T^{\chi}_{stretch} = -2\frac{\partial Y}{\partial x_i}S_{ij}\frac{\partial Y}{\partial x_j} = -2\chi s_i\lambda_i^2 = \chi R_{stretch}, \tag{1.5}$$

where s_i is the eigenvalue of the symmetric strain-rate tensor S_{ij}, referred to as the principal strain rate, and $\boldsymbol{e}_i$ is the corresponding eigenvector. The alignment of the scalar gradient with $\boldsymbol{e}_i$ is given by $\lambda_i = \nabla Y \cdot e_i/|\nabla Y|$. Therefore, the suitable definition of stretching rate is expressed as the combination of principal strain rate and alignment of scalar gradient (Han, Yu & Liu 2024)

$$R_{stretch} = -2s_i\lambda_i^2. \tag{1.6}$$

As demonstrated in various mixing scenarios, such as homogeneous isotropic turbulence (Girimaji & Pope 1990; Vincent & Meneguzzi 1991; Danish, Suman & Girimaji 2016), shock–turbulence interaction (Tian *et al.* 2017; Gao, Bermejo-Moreno & Larsson 2020) and turbulent combustion (Swaminathan & Grout 2006; Zhao *et al.* 2018), the stretching rate remains positive in value in general cases. Consequently, the stretching term is typically considered as the primary source of SDR growth.

Given the significance of the stretching term, the stretching mechanism has been primarily investigated from two perspectives. The first approach involves statistical analysis. Based on the persistent straining hypothesis, the stretching of the scalar gradient is treated as a series of independent, sequential stretching processes with short correlation

https://doi.org/10.1017/jfm.2025.11051 Published online by Cambridge University Press

time (Townsend 1951; Batchelor 1952; Cocke 1969). Under this assumption, the turbulent stretching rate is modelled as a Gaussian distribution, leading to the well-known exponential stretching observed in isotropic turbulence. This statistical framework has been extended to other types of flows, such as porous medium mixing (Le Borgne *et al.* 2013) and sheared particulate suspensions (Souzy *et al.* 2018). The second perspective examines the influence of local velocity gradients on the stretching mechanism. As expressed in (1.5), the stretching rate is the product of the principal strain rate and alignment, both of which are closely related to local velocity gradients. By decomposing the velocity gradient and scalar gradient equations on the frame composed of the eigenvectors of the symmetric strain-rate tensor, She, Jackson & Orszag (1991) and Dresselhaus & Tabor (1992) derived the principal strain rate and alignment equations. These governing equations demonstrate that both the principal strain rate and alignment are influenced by self-interaction, pressure Hessian and viscous effects (Nomura & Post 1998; Lapeyre *et al.* 1999, 2001; Tom, Carbone & Bragg 2021). Since these quantities are critical to characterising small-scale flow structures, the dynamics of stretching rate within various flow structures, such as flow topologies, has attracted significant attention (Brethouwer, Hunt & Nieuwstadt 2003; Danish *et al.* 2016; Zhao *et al.* 2018). Specifically, for the single vortex, it has been revealed that the axisymmetric distribution of the velocity gradients and pressure Hessian matrix lead to its algebraic stretching characteristic (Lapeyre, Klein & Hua 1999). These comprehensive investigations have deepened our understanding of the stretching mechanism in various types of flow. It is also noteworthy that the exponential stretching characteristic identified in SBI (Yang *et al.* 1993; Kumar *et al.* 2005) contradicts the algebraic stretching characteristic in a single vortex (Lapeyre *et al.* 1999), a contradiction that will be further explored in the subsequent sections of this study.

In contrast to the relatively well-developed understanding of the stretching mechanism, the relationship between SDR and the stretching dynamics has been addressed qualitatively. It is generally concluded that flow structures with high stretching rates promote the formation of scalar structures with high values of SDR (Boukharfane, Bouali & Mura 2018; Gao *et al.* 2020). The primary obstacle to developing a quantitative theory for SDR lies in the insufficient understanding of the nonlinear diffusion term in (1.4), specifically $(-2\mathcal{D})\partial/\partial x_i(\partial Y/\partial x_j)\partial/\partial x_i(\partial Y/\partial x_j)$. This term is strictly negative, representing the reduction in SDR due to the diffusional cancellation of gradients in the scalar field. Since the mathematical expression of the diffusion term involves the scalar gradient $\partial Y/\partial x_i$, the diffusion process is also influenced by the stretching dynamics. The pioneering work by Ranz (1979) states that the relationship between the diffusion process and stretching rate in PS mixing can be established analytically. By solving the advection–diffusion equation for deforming scalar strips, the diffusion of the mass fraction Y, enhanced by the stretching rate, can be analytically described. This approach has led to key concepts such as the mixing time (Meunier & Villermaux 2003) and the Batchelor mixing scale (Souzy *et al.* 2018). Villermaux's review (Villermaux 2019) provides a comprehensive overview of the theoretical methodology, which has been widely applied to characterise the distribution of the mass fraction Y in ideal vortices (Villermaux & Duplat 2003), turbulent jets (Duplat & Villermaux 2008; Duplat, Innocenti & Villermaux 2010), porous media (Le Borgne *et al.* 2013) and stratified shear flows (Petropoulos *et al.* 2023). Liu *et al.* (2022) firstly extended this framework to describe the diffusion process in VD SBI. They proposed a model for the mixing time by quantitatively expressing the VD stretching rate, which is enhanced by secondary baroclinic vorticity. This model offers a reliable prediction for the mixing time, defined as the time required to achieve a steady mixing state in VD SBI, and highlights the significant challenges posed by the inherent density variations in exploring the diffusion process in VD mixing. However, the analysis

https://doi.org/10.1017/jfm.2025.11051 Published online by Cambridge University Press

of mixing time only necessitates the local stretching rate at the characteristic location. Therefore, the stretching rate in this theory was not analysed from the perspective of the stretching dynamics, which limits its predictive capability for mixing time in VD SBI. Consequently, a comprehensive quantitative theory that elucidates the role of the stretching rate across the entire flow field in the evolution of the mixing process, as reflected by SDR within VD mixing, remains to be developed.

In summary, the intrinsic mechanism of VD mixing in SBI, particularly from the perspective of the stretching dynamics and its role in mixing, remains insufficiently understood. This study aims to elucidate this mechanism by providing a quantitative description of the evolution of the mixing rate SDR and mixedness, as a significant advancement of our previous work on the VD mixing time in SBI (Liu *et al.* 2022). Beginning with the relatively simple case of PS SBI, the stretching rate within a single vortex is firstly explored from the standpoint of the stretching dynamics, leading to the identification of an algebraic stretching characteristic. Based on the analytical expression of this stretching rate, a PS mixing model for SDR is proposed by considering the diffusion process on a series of stretched scalar strips. Within this framework, by integrating two density-gradient effects, referred to as the secondary baroclinic effect on the stretching dynamics and the density source effect on the diffusion process, the rigorous relationship between the stretching dynamics and the mixing rate SDR (mixedness) in VD mixing is established through a well-developed VD mixing model. Moreover, the critical role of the stretching dynamics in the mixing rate can be demonstrated through the scaling behaviour of the time-averaged mixing rate with the dimensionless Péclet number.

The organisation of this paper is as follows: § 2 provides an overview of the numerical method and case set-up. In § 3, we outline the framework of the stretching dynamics, and introduce the simplest case of the stretching dynamics, specifically, the stretching process within a single vortex, as the foundation for subsequent analysis. Based on the analytical expression of the single-vortex stretching rate, a relatively simplified model of PS mixing is proposed in § 4. Section 5 discusses two density-gradient effects influencing VD mixing, which inspire the development of the VD mixing model. In § 6, the VD mixing model is validated through its application to the prediction of the evolution of SDR and mixedness in VD SBI across a wide range of Mach numbers. The crucial role of the stretching rate in VD mixing is also demonstrated using a scaling analysis of the time-averaged SDR with respect to the Péclet number. Finally, our study is summarised and potential future research directions are discussed in § 7.

2. Numerical method and set-up

2.1. *Numerical method*

In this study, the governing equations used for simulating PS and VD SBI are the compressible Navier–Stokes equations with multiple components, expressed as

$$\begin{cases} \dfrac{\partial \rho}{\partial t} + \dfrac{\partial (\rho u_i)}{\partial x_i} = 0, \\ \dfrac{\partial\,(\rho u_i)}{\partial t} + \dfrac{\partial (\rho u_i u_j)}{\partial x_j} = -\dfrac{\partial p}{\partial x_i} + \dfrac{\partial \sigma_{ij}}{\partial x_j}, \\ \dfrac{\partial (\rho E)}{\partial t} + \dfrac{\partial (\rho u_i H)}{\partial x_i} = -\dfrac{\partial q_i}{\partial x_i} + \dfrac{\partial (u_j \sigma_{ij})}{\partial x_i}, \\ \dfrac{\partial (\rho Y_m)}{\partial t} + \dfrac{\partial (\rho u_i Y_m)}{\partial x_i} = \dfrac{\partial}{\partial x_i}\left(\rho \mathcal{D} \dfrac{\partial Y_m}{\partial x_i}\right), \\ m = 1, 2, \cdots, s-1. \end{cases} \tag{2.1}$$

https://doi.org/10.1017/jfm.2025.11051 Published online by Cambridge University Press

Here, the symbols ρ, p, E and $H = E + p/\rho$ denote the mixture's density, pressure, total energy per unit mass and total enthalpy per unit mass, respectively, u_i is the velocity of the mixture in the ith direction, Y_m refers to the mass fraction of species m with $\sum_{m=1}^{s} Y_m = 1$ and s is labelled as the total number of species. With the ideal gas hypothesis and Dalton's law of partial pressures, the system of (2.1) is closed by the ideal gas state equation

$$p = \sum_{m=1}^{s} p_m = \sum_{m=1}^{s} \rho_m \frac{\mathcal{R}_0}{M_m} T = \rho \mathcal{R} T = (\gamma - 1)\, \rho e, \tag{2.2}$$

where $\mathcal{R} = \mathcal{R}_0/M$ and $\mathcal{R}_0 = 8.314$ J(mol K)$^{-1}$ are the gas constant and universal gas constant, respectively; $M = (\sum_{m=1}^{s} Y_m/M_m)^{-1}$ and T are the molar mass and temperature of mixture respectively; p_m, $\rho_m = \rho Y_m$ and M_m represent the partial pressure, density and molar mass of the component m, respectively. The relation of the total energy per unit mass E and the specific internal energy e is given by

$$E = e + \frac{1}{2} u_i u_i = h - \frac{p}{\rho} + \frac{1}{2} u_i u_i. \tag{2.3}$$

Here, h is the enthalpy of the gas mixture

$$h = \sum_{m=1}^{s} Y_m h_m = \sum_{m=1}^{s} Y_m \left(h_{fm}^0 + \int_{T_0}^{T} \frac{C_{pm}}{M_m} dT \right), \tag{2.4}$$

in which h_{fm}^0 is the heat generated by the component m at the reference temperature T_0. The constant-pressure specific heat value C_{pm} is fitted by the following temperature-dependent polynomial function:

$$C_{pm} = \mathcal{R}_0 (a_{1m} + a_{2m} T + a_{3m} T^2 + a_{4m} T^3 + a_{5m} T^4), \tag{2.5}$$

where the coefficients $a_{1m}, \ldots, a_{5m}$ are obtained from the NASA thermochemical polynomial fit coefficient data (Kee *et al.* 1996).

With the definition of the constant-volume specific heat

$$C_{pm} - C_{vm} = \frac{\mathcal{R}_0}{M_m}, \tag{2.6}$$

the constant-pressure specific heat and constant-volume specific heat of the gas mixture are $C_p = \sum_{m=1}^{s} Y_m C_{pm}$ and $C_v = \sum_{m=1}^{s} Y_m C_{vm}$, and the specific heat ratio of the gas mixture is $\gamma = C_p/C_v$.

For the Newtonian fluid considered in this work, the viscous stress tensor and heat flux are defined as

$$\begin{cases} \sigma_{ij} = \mu \left(\dfrac{\partial u_i}{\partial x_j} + \dfrac{\partial u_j}{\partial x_i} - \dfrac{2}{3} \delta_{ij} \dfrac{\partial u_k}{\partial x_k} \right), \\ q_i = -\lambda \dfrac{\partial T}{\partial x_i}. \end{cases} \tag{2.7}$$

Here, δ_{ij} refers to the Kronecker delta. Based on the observation that the transport coefficients converge to nearly steady values after shock interaction (Liu *et al.* 2022), constant transport coefficients are employed in the numerical simulations to simplify

https://doi.org/10.1017/jfm.2025.11051 Published online by Cambridge University Press

the expression of the mixing model in the subsequent sections. Specifically, the viscous stress tensor σ_{ij} is calculated by the constant dynamic viscosity $\mu = 125 \times 10^{-6}$ Pa • s. The mass diffusion is simplified by ignoring pressure and temperature diffusion, and the Fickian diffusivity is assumed to be constant for different components, with a value of $\mathcal{D} = 355 \times 10^{-6}$ m^2 s^{-1}. Setting the diffusivity $\mathcal{D}$ as a constant does not accurately reflect the true physical situation. Assigning a constant value to $\mathcal{D}$ is typically used when designing SBI cases with varying Péclet numbers, which has also been employed in our previous studies (Yu *et al.* 2021, 2022). The heat flux q_i is calculated by the Fourier's law of heat conduction, and the heat conduction coefficient $\lambda = C_p \mu / Pr$ is calculated using a constant Prandtl number $Pr = 0.72$. After the mathematical model is constructed, the compressible Navier–Stokes equations are numerically solved using an in-house high-resolution code, *ParNS3D*, which has undergone extensive validation (Wang *et al.* 2018; Liang *et al.* 2019; Yu *et al.* 2022; Liu *et al.* 2022). Temporal discretisation is performed using the third-order total variation diminishing Runge–Kutta method. The fifth-order weighted essentially non-oscillatory (WENO) scheme (Liu *et al.* 1994; Jiang & Shu 1996) is employed for the discretisation of convection terms, while the second-order central difference method discretises the viscous terms.

2.2. *Initial conditions for VD and PS SBI*

This section presents the initial conditions for the numerical simulation of VD and PS SBI, using a case with a shock strength of $Ma = 2.4$ as an example. The case settings for other simulations, covering a broad range of Mach numbers from 1.22 to 4, are provided in Appendix A. The configuration for VD SBI settings is depicted in figure 1(*a*). The computation domain encompasses a two-dimensional space in a Cartesian coordinate system, with $X \times Y = [0, L_x] \times [0, L_y]$, where the length is $L_x = 30$ mm and the height is $L_y = 5.5$ mm. The shock is positioned at $x_{shock} = 0.7$ mm. The pre-shock air has the same thermodynamic states of 1 atm pressure and 293 K temperature prior to being impacted by the shock. The detailed initial conditions for post-shock air (u_1', ρ_1', P_1' and T_1') are calculated from the Rankine–Hugoniot equation. To avoid spurious vorticity arisen from the mesh discretisation (Niederhaus *et al.* 2008), the helium bubble, centred at the position $x_{bubble} = 4.5$ mm, consists of a core region with a radius of $R = 2.5$ mm and a diffusive layer with a width of δ. The diffusive layer is positioned at the edge of the core region, as illustrated in the inset in figure 1(*a*). Based on this configuration, the distribution of mass fraction of helium is set as

$$Y_{He}(r) = \begin{cases} Y_{max}, & r < R, \\ Y_{max} \mathrm{e}^{-\alpha[(r-R)/\delta]^2}, & R \leqslant r < R + \delta, \\ 0, & r \geqslant R + \delta, \end{cases} \tag{2.8}$$

where $Y_{max} = 1.0$, $\alpha = 5$ and $\delta = 5$. Using these parameters, the mass fraction distribution across the bubble is shown in figure 1(*b*). It can be observed that, with the selected parameters in (2.8), the mass fraction within the thin diffusive layer smoothly connects the mass fraction inside and outside the bubble, which is consistent with the results reported in our previous studies (Wang *et al.* 2018; Liu *et al.* 2022; Yu *et al.* 2022). To simplify subsequent expressions, the helium mass fraction Y_{He} is denoted as Y.

Since the influence of the reflected pressure wave on mixing is not considered in this study, the left boundary is set as an inlet, while the upper and right boundaries utilise a fourth-order extrapolation to prevent interference from pseudo-pressure reflection waves affecting the flow structures of interest. A symmetric boundary condition is applied at the bottom of the computational domain. The grid resolution study, detailed in Appendix B,

https://doi.org/10.1017/jfm.2025.11051 Published online by Cambridge University Press

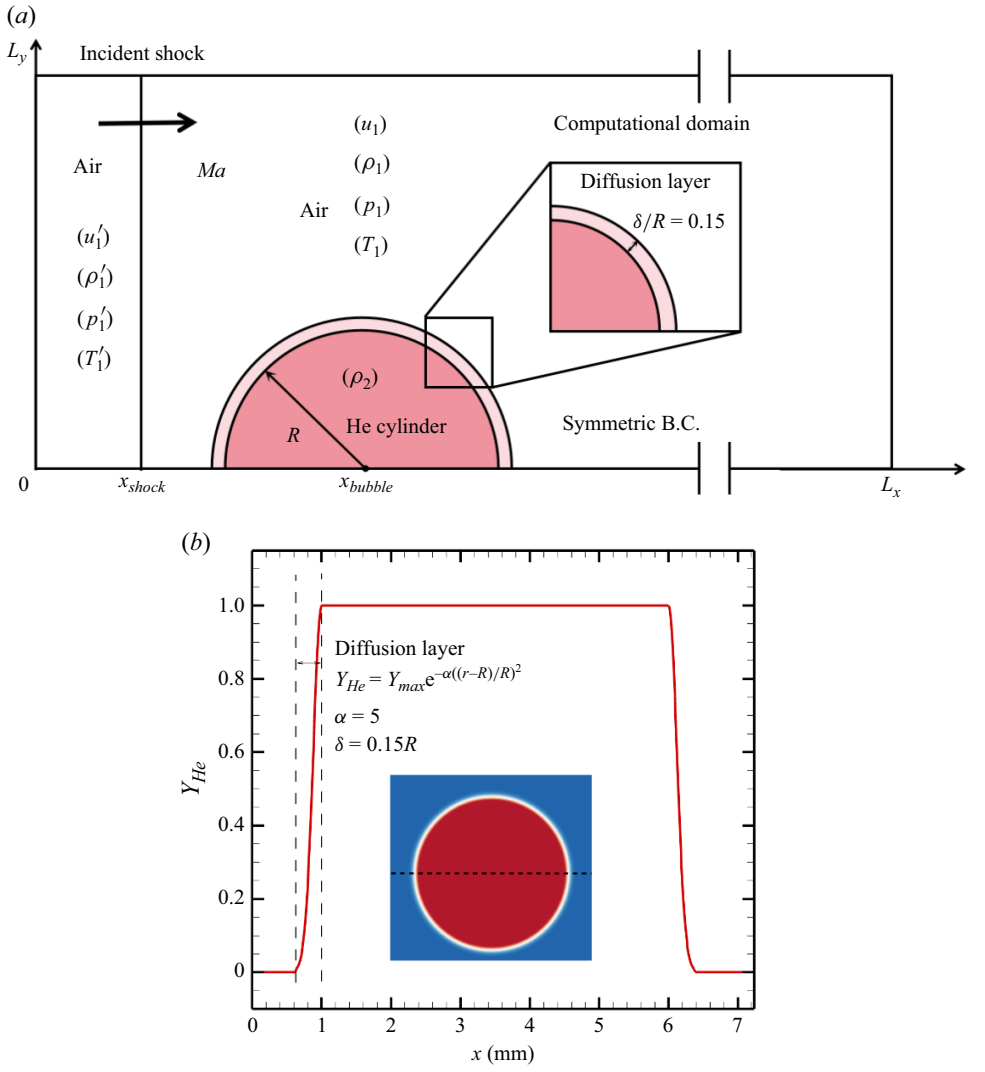


Figure 1. (*a*) Schematic of the initial conditions for VD SBI. (*b*) Distribution of the initial mass fraction of helium Y_{He} across the diameter of the bubble.

demonstrates that a uniform grid with a spacing of $\Delta = 1.25 \times 10^{-5}$ m is sufficient to accurately resolve the mixing process for the VD SBI case. Accordingly, the time step for the numerical simulation is selected as $\Delta t = 2 \times 10^{-9}$ s to ensure the Courant-Friedrichs-Lewy number satisfies the condition

$$\mathrm{CFL} = \frac{\Delta t}{\Delta/u_{max}} \approx \frac{\Delta t}{\Delta/u_2'} < 1. \tag{2.9}$$

Here, u_2' indicates the post-shock velocity of the helium bubble, which approximates the maximum velocity within the computation domain.

To investigate the stretching dynamics and its impact on mixing in VD SBI, we begin by developing a quantitative mixing model using a relatively simple PS SBI case. In this scenario, the density difference between the post-shock bubble and the ambient air is

https://doi.org/10.1017/jfm.2025.11051 Published online by Cambridge University Press

eliminated, specifically, by setting the post-shock Atwood number $At^+ = (\rho_2' - \rho_1')/(\rho_2' + \rho_1') \approx 0$, where ρ_2' and ρ_1' represent the post-shock bubble density and ambient air density, respectively. This adjustment allows the density effects to be effectively neglected as the vortex develops, ensuring that the mixing process does not influence the flow dynamics, as expected in PS mixing (Dimotakis 2005). However, the formation of the primary vortex depends on the baroclinic vorticity generated by the cylindrical interface of fluids with different densities subjected to a shock. If the density of the original bubble matches that of the ambient air, no vorticity is deposited along the bubble interface. Therefore, an artificial density adjustment method is applied to complete the set-up of the initial conditions for the PS SBI. On the basis of the VD SBI case with the shock Mach number $Ma = 2.4$, the cylindrical bubble's mass fraction is adjusted artificially soon after the shock interaction

$$\begin{cases} Y_{He}^{ps} = 0.0001 \times Y_{He}^{VD}, \\ Y_{O_2}^{ps} = 0.233 \times \left(1 - Y_{He}^{ps}\right), \\ Y_{N_2}^{ps} = 0.767 \times \left(1 - Y_{He}^{ps}\right), \end{cases} \tag{2.10}$$

where a small amount of component is maintained to display the mixing process. With the pressure and temperature identical to those in VD SBI

$$\begin{cases} p^{ps} = p^{VD}, \\ T^{ps} = T^{ps}, \end{cases} \tag{2.11}$$

the density of the bubble after the shock interaction will increase to the value of post-shock air

$$\begin{cases} \rho^{ps} = \dfrac{p^{ps}}{\mathcal{R}T^{ps}} \approx \rho^{air}, \\ \mathcal{R} = \mathcal{R}_0 \displaystyle\sum_{m=1}^{s} \dfrac{Y_m^{ps}}{M_m}. \end{cases} \tag{2.12}$$

To ensure comparability of the mixing indicators between PS SBI and VD SBI, the mass fraction in PS SBI, denoted Y^{ps}, is normalised by the initial maximum mass fraction Y_0^{max} in the following context, such that $Y = Y^{ps}/Y_0^{max}$. This method increases the bubble's density to match that of the post-shock air, as outlined in our prior research (Liu *et al.* 2022). It is worth noting that this artificial density adjustment, achieved through modification of the mass fraction, is a general technique. It has been widely employed in the set-up of various PS mixing scenarios, including PS SBI (Liu *et al.* 2022), PS shock–turbulence interaction (Tian *et al.* 2017, 2019) and PS mixing induced by random weak shock waves (Jossy & Gupta 2025).

The numerical simulation results of the VD and PS SB, based on the set-up described above, are presented in figure 2, which depicts the time evolution of both density and vorticity contours. In the VD SBI case, positive primary baroclinic vorticity is generated due to the misalignment between the density gradient of the bubble and the pressure gradient induced by the shock. This primary vorticity drives the formation of a large-scale main vortex, as shown in the lower half of figure 2. As the main vortex develops, a vortex-bilayer structure emerges, characterised by dominant negative vorticity that intensifies and rolls up the positive vorticity. This structure, identified as secondary baroclinic vorticity (SBV), is consistent with previous studies (Gupta, Zhang & Zabusky 2003; Peng, Zabusky & Zhang 2003) and is recognised as a classical phenomenon in VD RMI (Peng *et al.* 2021*a*,*b*). In contrast, the density contour of the PS SBI case shows that the artificial density adjustment method effectively removes the density difference between the bubble

https://doi.org/10.1017/jfm.2025.11051 Published online by Cambridge University Press

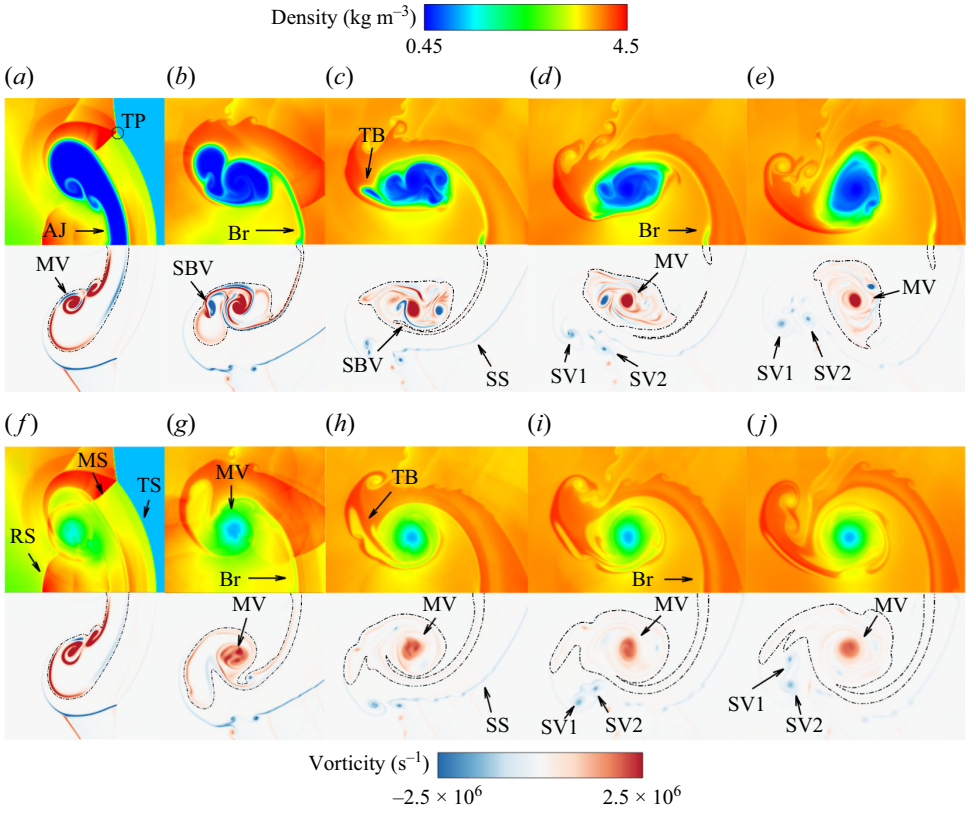


Figure 2. Time evolution of the density contour (top) and the vorticity contour (bottom) for VD SBI case with shock Mach number 2.4 at (*a*) $t = 10.8$ μs; (*b*) $t = 21.6$ μs; (*c*) $t = 32.4$ μs; (*d*) $t = 43.2$ μs; and (*e*) $t = 54.0$ μs. The PS SBI case is presented at the same moments as those of VD SBI on the bottom from (*f*) to (*j*). Dashed-dot line indicates the isoline of $Y = 0.01Y_{max}$($Y_{max} = 1.0$ for VD SBI and $Y_{max} = 0.0001$ for PS SBI). Here, AJ, air jet; TP, triple point; MV, main vortex; MS, Mach stem; TS, transmitted shock; RS, reflected shock; Br, bridge; SBV, secondary baroclinic vorticity; TB, trailing bubble; SS, slip stream; SV1 and SV2, secondary vortex 1 and secondary vortex 2.

and ambient air. Consequently, the SBV vanishes, and only the main vortex is preserved. In both the PS SBI and VD SBI cases, the formation of a nearly steady single vortex is observed. Accordingly, the total circulation Γ_t and the compression rate η are examined. These two parameters are defined as

$$\begin{cases} \Gamma_t = \displaystyle\int_{Y > Y_{threshold}} \omega \, \mathrm{dV}, \\ \eta = \dfrac{\mathcal{V}_b}{\mathcal{V}_0} = \dfrac{\int_{Y > Y_{threshold}} \mathrm{dV}}{\mathcal{V}_0}, \end{cases} \tag{2.13}$$

where ω is the magnitude of the vorticity vector $\boldsymbol{\omega} = \nabla \times \boldsymbol{u}$, $\mathcal{V}_0$ is the initial volume of the helium bubble, $\mathcal{V}_b$ is the volume of the compressed bubble following the shock interaction and the threshold is chosen as $Y_{threshold} = 1\,\%Y_{max}$ to obtain stable values of the total circulation Γ_t and the compression rate η in the later stage of VD SBI. Figure 3 illustrates the evolution of Γ_t and η in both VD and PS SBI cases. Following the shock interaction with the bubble, both the total circulation Γ_t and the compression

https://doi.org/10.1017/jfm.2025.11051 Published online by Cambridge University Press

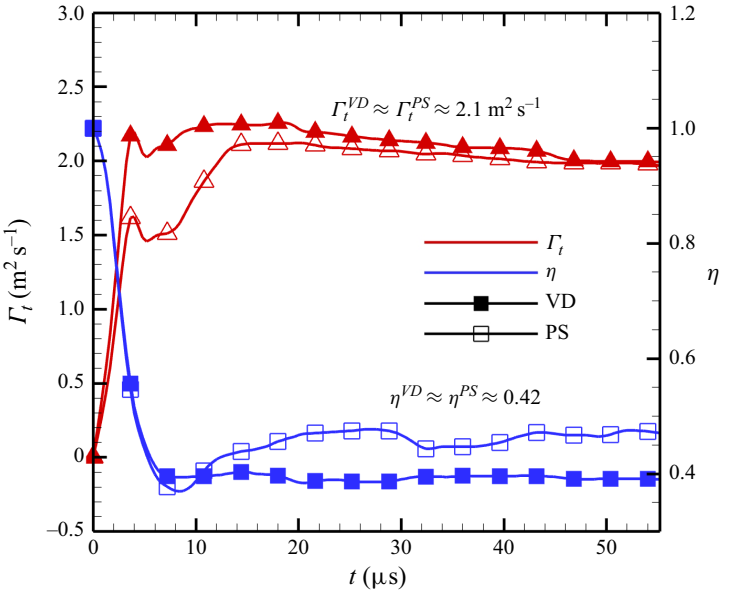


Figure 3. Comparison of the total circulation Γ_t and compression rate η between the PS and VD SBI cases at a shock Mach number of 2.4.

	Ma	p_1' (Pa)	T_1' (K)	u_1' (m s^{-1})	W_t (m s^{-1})	At^+ (−)	μ (*Pa* s)	Γ_t (m^2 s^{-1})	*Re* (−)	*Pe* (−)
VD	2.4	667391.3	596.87	568.31	1678.08	−0.845	125.0×10^{-6}	2.09	38446.2	5887.3
PS	2.4	667391.3	596.87	568.31	1678.08	0.0	230.9×10^{-6}	2.09	38446.2	5887.3

Table 1. The set-up for the PS SBI case based on the VD SBI case with a shock Mach number of $Ma = 2.4$. Compared with VD SBI, the post-shock parameters p_1', T_1', u_1' and T_1' in PS SBI remain unchanged, while the Atwood number, reflecting the post-shock density difference, is set to zero ($At^+ = 0$). With the total circulation Γ_t preserved, the Péclet number is maintained, and the Reynolds number *Re* is held constant by adjusting the dynamic viscosity μ in the PS SBI case.

rate η converge to nearly constant values, indicating the formation of a nearly steady single vortex. It is also observed that the total circulation Γ_t in both the PS and VD SBI cases is nearly identical. Although the compression rate in the PS SBI case is approximately 20% greater than in the VD SBI case, the impact of this small difference in η on the subsequent discussions is negligible. Therefore, the compression rate η can be considered a consistent value of 0.42 for both the PS and VD SBI cases. Consequently, both the total circulation Γ_t and the compression rate η are unaffected by the specific settings of the PS SBI case. Furthermore, due to the conservation of the total circulation Γ_t and the alteration in bubble density in the PS SBI, the dynamic viscosity is adjusted to maintain the same dimensionless Reynolds number $Re = \Gamma_t/\nu$. This modification is expressed as $\mu^{ps} = \mu^{VD}(2\rho_2'/(\rho_1' + \rho_2'))$, ensuring the kinematic viscosity $\nu = \mu/\overline{\rho'}$ remains constant. The maintenance of $Pe = \Gamma_t/\mathcal{D}$ is achieved by keeping the same Fickian diffusivity $\mathcal{D}$. The set-up for the PS SBI case is summarised in table 1.

The reduction of SBV due to the absence of density differences is a primary characteristic of PS mixing. Another feature of PS mixing is that the evolution of the

https://doi.org/10.1017/jfm.2025.11051 Published online by Cambridge University Press

mass fraction Y follows the advection–diffusion equation (Warhaft 2000), expressed as

$$\frac{\partial Y}{\partial t} + \frac{\partial (u_i Y)}{\partial x_i} = \mathcal{D}\frac{\partial^2 Y}{\partial {x_j}^2}. \tag{2.14}$$

Here, the absence of density differences also leads to the reduction of the multi-component transport equation in (2.1) to the advection–diffusion equation, indicating a shift from a VD mixing characteristic to a PS mixing characteristic. As shown in (2.1), the multi-component transport equation for the mass fraction of helium Y is expressed as

$$\frac{\partial (\rho Y)}{\partial t} + \frac{\partial (\rho u_i Y)}{\partial x_i} = \frac{\partial}{\partial x_j}\left(\rho \mathcal{D}\frac{\partial Y}{\partial x_j}\right). \tag{2.15}$$

Since the Fickian diffusivity $\mathcal{D}$ is treated as constant in our numerical simulations, this equation can be rewritten in the form VD advection–diffusion equation

$$\frac{\partial Y}{\partial t} + \frac{\partial (u_i Y)}{\partial x_i} = \frac{\mathcal{D}}{\rho}\left(\frac{\partial \rho}{\partial x_j}\frac{\partial Y}{\partial x_j}\right) + \mathcal{D}\frac{\partial^2 Y}{\partial x_j^2}. \tag{2.16}$$

When the density gradient $\partial\rho/\partial x_j$ vanishes in the PS SBI, this equation reduces to the standard advection–diffusion equation.

In summary, the PS SBI set-up transforms the VD SBI into a system with two key PS mixing characteristics: (i) the disappearance of SBV during the development of the single vortex, and (ii) the reduction of the multi-component transport equation to the advection–diffusion equation. These two features facilitate the development of a quantitative theory for describing the stretching dynamics and its impact on mixing, which will be presented in the following sections.

3. The SDR evolution of SBI: an analogy to single-vortex dynamics

In this section, we present the preliminaries for analysing the stretching dynamics. By examining the temporal evolution of SDR in both PS and VD SBI, the fundamental role of stretching dynamics in governing mixing is highlighted. Utilising the precise definition of the stretching rate in (1.5), the framework for the stretching dynamics is developed within the eigenframe of the strain-rate tensor. This framework comprises the stretching dynamics governing equations for the principal strain (SDGE-s_i) and for the scalar gradient alignment (SDGE-λ_i). Considering that the formation of a nearly steady single vortex is observed in both PS and VD SBI cases, as shown in figure 2, the mixing in SBI is reasonable to be assumed to be governed by the large-scale single vortex. Therefore, SDGE-s_i and SDGE-λ_i are analytically solved under single-vortex assumptions. The section concludes by exploring the interpretation of the stretching rate from the geometric viewpoint, providing the foundation for developing a quantitative model to describe the mixing rate in both PS and VD SBI.

3.1. *Importance of the stretching term to SDR evolution in SBI*

To explore the role of the stretching dynamics in mixing for PS and VD SBI, it is essential to define the stretching rate within an appropriate framework. Following previous studies on PS mixing (Cetegen & Mohamad 1993; Buch & Dahm 1996), the SDR, denoted as χ and defined in (1.3), serves as a suitable mixing indicator for this purpose. The definition and physical interpretation of SDR stem from another mixing indicator, the mixedness parameter f defined in (1.1). This parameter quantifies the extent of mixing,

https://doi.org/10.1017/jfm.2025.11051 Published online by Cambridge University Press

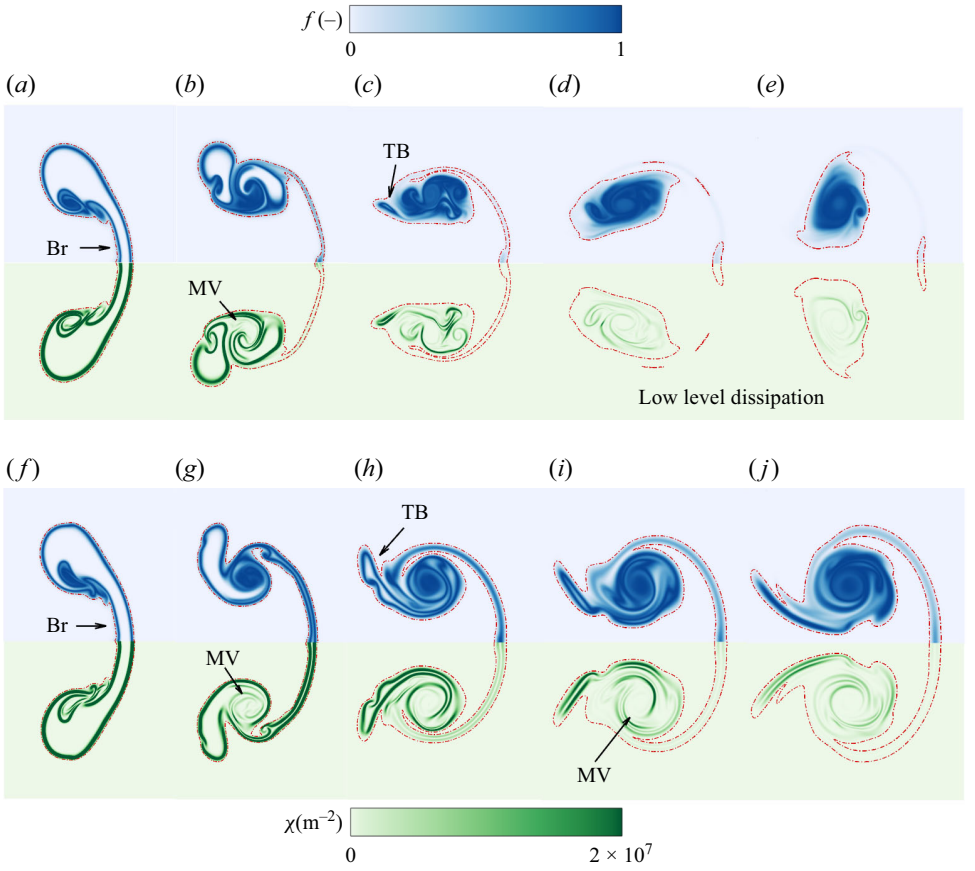


Figure 4. Time evolution of the mixedness contour (top) and the SDR contour (bottom) for VD SBI case with shock Mach number 2.4 at (*a*) $t = 10.8$ μs; (*b*) $t = 21.6$ μs; (*c*) $t = 32.4$ μs; (*d*) $t = 43.2$ μs; and (*e*) $t = 54.0$ μs. The PS SBI case is presented at the same moments as those of VD SBI in the bottom from (*f*) to (*j*). Red dashed-dot line indicates the isoline of $Y = 0.01$.

and reaches its maximum when the mass fractions of the bubble's relevant component and the surrounding air are equal.

Following the definition of mixedness and based on (2.15), the behaviour of mixedness f is governed by the following equation:

$$\left(\frac{\partial}{\partial t} + u_j \frac{\partial}{\partial x_j} - \mathcal{D}\frac{\partial^2}{\partial x_j^2}\right) f = 8\mathcal{D}\frac{\partial Y}{\partial x_j}\frac{\partial Y}{\partial x_j} + 4\,(1-2Y)\,\frac{\mathcal{D}}{\rho}\frac{\partial \rho}{\partial x_j}\frac{\partial Y}{\partial x_j}. \tag{3.1}$$

The first term on the right-hand side is strictly positive, representing the growth rate of mixedness. Thus the definition of SDR $\chi = (\partial Y/\partial x_i)(\partial Y/\partial x_i)$ reflects the physical meaning of mixing rate. The second term originates from the density gradient $\partial\rho/\partial x_i$, and vanishes in PS SBI due to the disappearance of density difference.

Figure 4 illustrates the temporal evolution of both mixedness and SDR in PS and VD SBI. As the initially concentrated bubble undergoes the stretching process, the SDR initially increases, subsequently decreases at the later stages and ultimately dissipates, indicating the achievement of a well-mixed state. Different from the behaviour of SDR, the general trend of the mixedness is monotonically increasing. The evolution processes of these two mixing indicators (1.1 and (1.3)) can be described in detail by examining their

https://doi.org/10.1017/jfm.2025.11051 Published online by Cambridge University Press

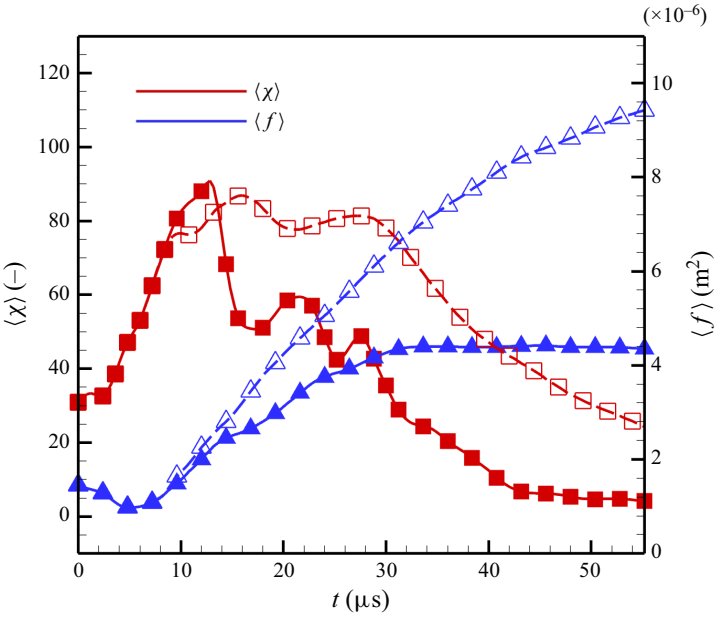


Figure 5. Time evolution of the total mixedness (blue) and SDR (red) for PS and VD SBI cases demonstrated in figure 4, respectively. The solid line labels the VD SBI, while the dashed line indicates the PS SBI.

total values, which are defined by the corresponding volume integrations

$$\begin{cases} \langle f \rangle = \iiint_{\mathcal{V}} f \,\mathrm{dV}, \\ \langle \chi \rangle = \iiint_{\mathcal{V}} \chi \,\mathrm{dV}. \end{cases} \tag{3.2}$$

As shown in figure 5, the mixedness in both PS and VD SBI increases monotonically. In contrast, the SDR initially increases and then decreases after a certain moment. Another notable observation from this figure is that, despite the total circulation Γ_t and compression rate η being consistent between PS SBI and VD SBI, there is a significant difference in the total mixedness $\langle f \rangle$ and the total SDR $\langle \chi \rangle$ between the two cases. This phenomenon arises from the discrepancy between the mixing mechanism in PS and VD mixing flow, which will be exhibited further in the following sections.

To gain further insight into the underlying mechanisms driving these two mixing indicators, it is necessary to derive the corresponding governing equations. For the mixedness equation, using the mathematical expression for the time derivative of the volumetric mean value (Yu *et al.* 2021), we have

$$\frac{\mathrm{D}\langle f \rangle}{\mathrm{D}t} = \left\langle \frac{\mathrm{D}f}{\mathrm{D}t} \right\rangle + \left\langle \left(\frac{\partial u_i}{\partial x_i} \right) f \right\rangle, \tag{3.3}$$

which leads to the governing equation for the total mixedness $\langle f \rangle$ as

$$\frac{\mathrm{D}\langle f \rangle}{\mathrm{D}t} = \left\langle 8\mathcal{D} \frac{\partial Y}{\partial x_j} \frac{\partial Y}{\partial x_j} \right\rangle + \left\langle 4\,(1-2Y)\,\frac{\mathcal{D}}{\rho} \frac{\partial \rho}{\partial x_j} \frac{\partial Y}{\partial x_j} \right\rangle + \left\langle -\left(\frac{\partial u_i}{\partial x_i} \right) f \right\rangle. \tag{3.4}$$

Subsequently, the source of total mixedness growth $\Delta \langle f \rangle = \langle f \rangle|_t - \langle f \rangle|_0$ can be decomposed by considering the absence of mixedness transport across the boundaries of the integration region, specifically $\langle \mathcal{D}(\partial^2 f / \partial x_j^2) \rangle = 0$. This decomposition is described as

https://doi.org/10.1017/jfm.2025.11051 Published online by Cambridge University Press

follows:

$$\begin{cases} \Delta\langle f\rangle = \left\langle T^f_{SDR}\right\rangle + \left\langle T^f_{den}\right\rangle + \left\langle T^f_{divU}\right\rangle, \\ \left\langle T^f_{SDR}\right\rangle = \displaystyle\int_0^t \left\langle 8\mathcal{D}\frac{\partial Y}{\partial x_j}\frac{\partial Y}{\partial x_j}\right\rangle \mathrm{d}t', \\ \left\langle T^f_{den}\right\rangle = \displaystyle\int_0^t \left\langle 4\,(1-2Y)\,\frac{\mathcal{D}}{\rho}\frac{\partial \rho}{\partial x_j}\frac{\partial Y}{\partial x_j}\right\rangle \mathrm{d}t', \\ \left\langle T^f_{divU}\right\rangle = \displaystyle\int_0^t \left\langle -\left(\frac{\partial u_i}{\partial x_i}\right) f\right\rangle \mathrm{d}t', \end{cases} \tag{3.5}$$

where $\langle T^f_{SDR}\rangle$ is the SDR source term, $\langle T^f_{den}\rangle$ is the density-gradient source term and $\langle T^f_{divU}\rangle$ is the velocity-divergence source term. Similar to the total mixedness equation in (3.4), the governing equation for the total SDR can also be derived based on (2.15) as

$$\begin{cases} \dfrac{\mathrm{D}\,\langle\chi\rangle}{\mathrm{D}t} = \langle T^\chi_{stretch}\rangle + \left\langle T^\chi_{diff}\right\rangle + \langle T^\chi_{source}\rangle + \langle T^\chi_{divU}\rangle, \\ \langle T^\chi_{stretch}\rangle = \left\langle -2\dfrac{\partial Y}{\partial x_i}S_{ij}\dfrac{\partial Y}{\partial x_j}\right\rangle, \\ \left\langle T^\chi_{diff}\right\rangle = \left\langle -2\mathcal{D}\dfrac{\partial}{\partial x_i}\left(\dfrac{\partial Y}{\partial x_j}\right)\dfrac{\partial}{\partial x_i}\left(\dfrac{\partial Y}{\partial x_j}\right)\right\rangle, \\ \langle T^\chi_{source}\rangle = \left\langle 2\mathcal{D}\dfrac{\partial Y}{\partial x_i}\dfrac{\partial}{\partial x_i}\left(\dfrac{1}{\rho}\dfrac{\partial \rho}{\partial x_j}\dfrac{\partial Y}{\partial x_j}\right)\right\rangle, \\ \langle T^\chi_{divU}\rangle = \left\langle -\left(\dfrac{\partial u_i}{\partial x_i}\right)\chi\right\rangle, \end{cases} \tag{3.6}$$

where $\langle T^\chi_{stretch}\rangle$ is the stretching term expressed as the combination of the scalar gradient $\partial Y/\partial x_i$ and the symmetric strain-rate tensor $S_{ij} = 1/2(\partial u_i/\partial x_j + \partial u_j/\partial x_i)$, $\langle T^\chi_{diff}\rangle$ is the diffusion term, $\langle T^\chi_{source}\rangle$ is the density-gradient source term and $\langle T^\chi_{divU}\rangle$ is the velocity-divergence source term.

We begin by analysing the decomposition of the total mixedness growth $\Delta\langle f\rangle$ as expressed in (3.5). As shown in figure 6, the initial decrease in total mixedness $\Delta\langle f\rangle$ arises from the velocity-divergence source term $\langle T^f_{divU}\rangle$ in both PS and VD SBI cases, reflecting the effect of shock compression. The primary driver of the monotonic increase in total mixedness, however, is the SDR source term $\langle T^f_{SDR}\rangle$. These findings from the decomposition of total mixedness growth confirm that the SDR χ accurately represents the physical mixing rate and underscore that the growth of mixedness can be almost represented by the SDR source term, which is defined by the time integration of the SDR.

Furthermore, the governing equation for the SDR in (3.6) is analysed in figure 7. Consistent with previous studies (Danish *et al.* 2016; Tian *et al.* 2017; Gao *et al.* 2020), the stretching term $\langle T^\chi_{stretch}\rangle$ serves as the primary contributor to SDR growth, while the strictly negative diffusion term $\langle T^\chi_{diff}\rangle$ is the predominant factor in SDR reduction. In comparison, the effects of the density-gradient source term $\langle T^\chi_{source}\rangle$ and the velocity-divergence source term $\langle T^\chi_{divU}\rangle$ on SDR are nearly negligible. This observation highlights that the evolution of SDR is governed by the coupled interaction of stretching dynamics and diffusion processes. Therefore, understanding the SDR necessitates a focus on the

https://doi.org/10.1017/jfm.2025.11051 Published online by Cambridge University Press

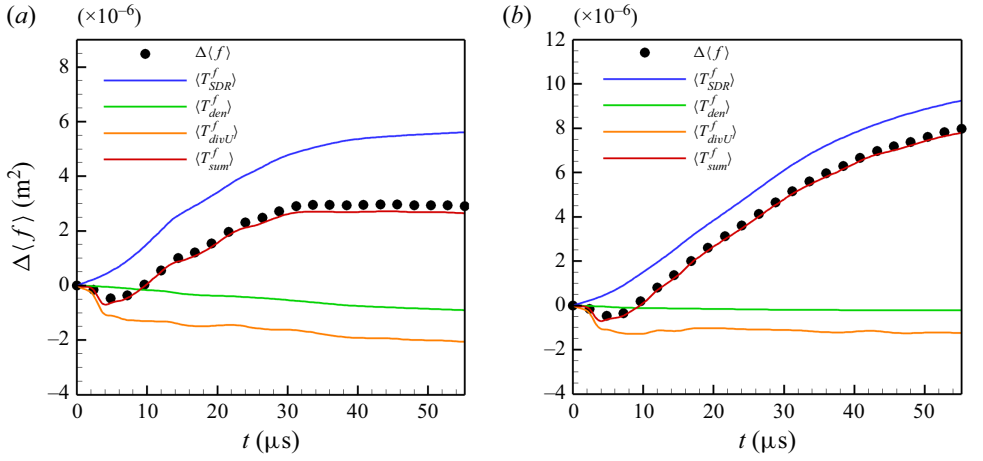


Figure 6. The decomposition of the total mixedness growth $\Delta\langle f\rangle$ in (3.5) for (*a*) VD SBI and (*b*) PS SBI. The black symbols refers to the increment of the total mixedness $\Delta\langle f\rangle$, which is calculated from the corresponding evolution of $\langle f\rangle$ in figure 5. The red solid line indicates the summation of the terms on the right side of (3.5) $\langle T^f_{sum}\rangle$.

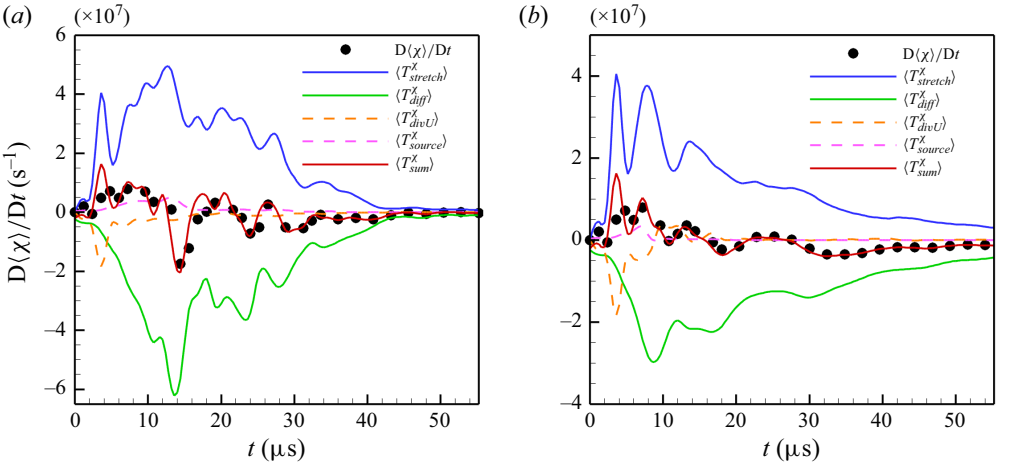


Figure 7. The decomposition of the material derivative of the total SDR growth $\mathrm{D}\langle\chi\rangle/\mathrm{D}t$ in (3.6) for (*a*) VD SBI and (*b*) PS SBI. The black symbols refers to the material derivative of the total SDR growth $\mathrm{D}\langle\chi\rangle/\mathrm{D}t$, which is obtained from the evolution of $\langle\chi\rangle$ in figure 5. The red solid line indicates the summation of the terms on the right side of (3.6) $\langle T^\chi_{sum}\rangle$.

stretching dynamics, with the stretching term defined rigorously within this framework: $T^\chi_{stretch} = -2(\partial Y/\partial x_i)S_{ij}(\partial Y/\partial x_j)$.

3.2. *Stretching dynamics governing equations (SDGEs)*

To further explore the stretching dynamics, according to the symmetry of the strain-rate tensor S_{ij}, the stretching term can be decomposed within an orthogonal strain-rate eigenframe, which consists of the principal strain rates s_i and their corresponding eigenvectors $\boldsymbol{e}_i$. The orthogonal expression of the stretching term is provided by (1.5): $T^\chi_{stretch} = -2\chi s_i\lambda_i^2$, indicating that the stretching term $T^\chi_{stretch}$ is influenced by both the principal strain rates s_i and the alignment of the scalar gradient with the corresponding

https://doi.org/10.1017/jfm.2025.11051 Published online by Cambridge University Press

eigenvectors $\lambda_i = \nabla Y \cdot \boldsymbol{e}_i / |\nabla Y|$. Consequently, the stretching rate is defined as the product of the principal strain rate s_i and the scalar gradient alignment λ_i as described in (1.6): $R_{stretch} = -2 s_i \lambda_i^2$.

Analysing the stretching rate $R_{stretch}$ from the perspective of the stretching dynamics requires the governing equations for the principal strain rate s_i and the alignment of the scalar gradient λ_i. These two equations can be derived by taking the gradient of the momentum equation in (2.1) and the multi-component transport equation in (2.15), and projecting them onto the strain-rate eigenframe (Dresselhaus & Tabor 1992; Ohkitani & Kishiba 1995; Tom *et al.* 2021; Han *et al.* 2024). Details of these derivations are provided in the supplementary material are available at https://doi.org/10.1017/jfm.2025.11051. We refer to the principal strain-rate equations as the SDGEs for s_i (SDGE-s_i), which are expressed as follows:

$$\begin{cases} \dfrac{\mathrm{d}}{\mathrm{d}t} s_i = -s_i^2 - \dfrac{1}{4}\left(\widetilde{\omega_i}^2 - \omega^2\right) + \widetilde{H_{ii}^p} + \widetilde{H_{ii}^b} + \widetilde{H_{ii}^v}, \\ \left(s_j - s_i\right) \widetilde{W}_{ij} = -\dfrac{1}{4}\widetilde{\omega_i}\widetilde{\omega_j} + \widetilde{H_{ij}^p} + \widetilde{H_{ij}^b} + \widetilde{H_{ij}^v}, \\ \dfrac{\mathrm{d}}{\mathrm{d}t}\widetilde{\omega_i} = s_i \widetilde{\omega_i} - \left(\dfrac{\partial u_i}{\partial x_i}\right) \widetilde{\omega_i} + \widetilde{B}_i + \widetilde{T_i^v} - \widetilde{\omega_j} \widetilde{W}_{ij}, \end{cases} \tag{3.7}$$

In the first of these equations, s_i represents the principal strain rate, $\widetilde{\omega_i} = \boldsymbol{e}_i^T \cdot \boldsymbol{\omega}$ are the vorticity components in the strain eigenframe, where $\boldsymbol{\omega} = \nabla \times \boldsymbol{u}$ is the vorticity vector. The norm of the vorticity vector is given by $\omega = ||\boldsymbol{\omega}||$. The terms $H_{ij}^p = -1/\rho(\partial^2 p/\partial x_i \partial x_j)$, $H_{ij}^b = 1/(2\rho^2)((\partial\rho/\partial x_i)(\partial p/\partial x_j) + (\partial\rho/\partial x_j)(\partial p/\partial x_i))$ and $H_{ij}^v = 1/2[\partial/\partial x_j((1/\rho)\partial\sigma_{ik}/\partial x_k) + \partial/\partial x_i((1/\rho)\partial\sigma_{jk}/\partial x_k)]$ correspond to the pressure Hessian, baroclinic strain and viscous stress matrix, respectively. The notation $\widetilde{()}$ denotes the projection of these matrices onto the strain eigenframe, calculated as

$$\widetilde{H_{ij}^p} = \boldsymbol{e}_i^T \boldsymbol{H}^p \boldsymbol{e}_j, \qquad \widetilde{H_{ij}^b} = \boldsymbol{e}_i^T \boldsymbol{H}^b \boldsymbol{e}_j, \qquad \widetilde{H_{ij}^v} = \boldsymbol{e}_i^T \boldsymbol{H}^v \boldsymbol{e}_j. \tag{3.8}$$

In the second equation, $\widetilde{W}_{ij}$ characterises the rate of rotation within the plane formed by two eigenvectors about the axis of the third one, that is $\widetilde{W}_{ij} = (\mathrm{d}/\mathrm{d}t)\boldsymbol{e}_j \cdot \boldsymbol{e}_i$. The third equation pertains to the vorticity dynamics, where $\widetilde{B}_i$ and $\widetilde{T_i^v}$ represent the projections of the baroclinic vorticity $B_i = \epsilon_{ijk}(1/\rho^2)(\partial\rho/\partial x_j)(\partial p/\partial x_k)$ and the viscous contribution $T_i^v = \epsilon_{ijk}(\partial/\partial x_j)((1/\rho)(\partial\sigma_{kn}/\partial x_n))$ onto the strain eigenframe, expressed as

$$\widetilde{B}_i = \boldsymbol{e}_i^T \boldsymbol{B}, \qquad \widetilde{T_i^v} = \boldsymbol{e}_i^T \boldsymbol{T^v}, \tag{3.9}$$

where ϵ_{ijk} is the permutation symbol.

The SDGE for λ_i (SDGE-λ_i) pertains to the alignment of the scalar gradient λ_i, and is formulated as follows:

$$\frac{\mathrm{d}}{\mathrm{d}t}\lambda_i = -s_i\lambda_i + \xi_{stretch}\lambda_i - \widetilde{W}_{ij}\lambda_j + \frac{1}{2}\epsilon_{ijk}\widetilde{\omega_j}\lambda_k + \frac{1}{\sqrt{\chi}} T_i^{others}, \tag{3.10}$$

where $\xi_{stretch} = s_i\lambda_i^2$ represents the stretching contribution, and $(1/\sqrt{\chi})T_i^{others}$ characterises the diffusion effect. Due to the presence of the square root of SDR in the denominator of the diffusion effect, $(1/\sqrt{\chi})T_i^{others}$ can generally be neglected in the context of flow structures with a large SDR value. This simplification is justified and demonstrated in Appendix C.

By focusing on the principal strain s_i and the scalar gradient alignment λ_i, the framework for the stretching dynamics, which centres on the stretching rate

https://doi.org/10.1017/jfm.2025.11051 Published online by Cambridge University Press

$R_{stretch} = -2s_i\lambda_i^2$, can be comprehensively described through the combination of SDGE-s_i and SDGE-λ_i. The validity of the framework is corroborated through Lagrangian methods, as detailed in Appendix C.

3.3. *Analytical solution of SDGEs in a single vortex*

Motivated by the formation of a nearly steady single vortex following the shock's interaction with the bubble, as depicted in figure 2, this subsection investigates the stretching dynamics within a single vortex. This research is conducted by solving the SDGEs analytically in a cylindrical coordinate system (r, φ), where the centre of the main vortex serves as the origin. In this context, r represents the radial direction, while φ indicates the azimuthal direction. To facilitate the simplification of the SDGEs, several assumptions and observations regarding vortex morphology for PS mixing are introduced:

Assumption PS.(i) The single vortex is axisymmetric in the azimuthal direction φ, with negligible radial velocity, implying $\partial/\partial\varphi = 0$ and $u_r = 0$. This assumption simplifies the momentum equation in (2.1) to $-u_\varphi^2/r = -(1/\rho)\partial p/\partial r$.

Assumption PS.(ii) Following the shock interaction, the single vortex is considered incompressible, aligning with previous research on RMI (Peng *et al.* 2021*a*).

Assumption PS.(iii) The density gradient within the single vortex is negligible, i.e. $\boldsymbol{\nabla}\rho = 0$.

Assumption PS.(iv) The mixing of PS SBI can be approximated as the mixing of a compressed semicircle composed of a series of scalar strips, each undergoing deformation due to the continuous stretching effect of the single vortex.

The validation of these assumptions is provided in the supplementary materials. Under assumptions PS.(i) and two-dimensional flow conditions, the SDGE-s_i presented in (3.7) can be simplified by expressing these equations in cylindrical coordinates as follows:

$$\begin{cases} \dfrac{\mathrm{d}}{\mathrm{d}t}s_1 = -\dfrac{1}{2\rho^2}\dfrac{1}{r}\dfrac{\partial\rho}{\partial\varphi}\dfrac{\partial p}{\partial r} + \nu\left(\dfrac{\partial^2 s_1}{\partial r^2} + \dfrac{1}{r}\dfrac{\partial s_1}{\partial r}\right), \\ \dfrac{\mathrm{d}}{\mathrm{d}t}s_2 = \dfrac{1}{2\rho^2}\dfrac{1}{r}\dfrac{\partial\rho}{\partial\varphi}\dfrac{\partial p}{\partial r} + \nu\left(\dfrac{\partial^2 s_2}{\partial r^2} + \dfrac{1}{r}\dfrac{\partial s_2}{\partial r}\right), \\ \widetilde{W_{12}} \approx \dfrac{\widetilde{H_{12}^p} + \widetilde{H_{12}^b}}{s_2 - s_1} = -\dfrac{u_\varphi}{r}, \\ \dfrac{\mathrm{d}}{\mathrm{d}t}\omega = -\dfrac{1}{2\rho^2}\dfrac{1}{r}\dfrac{\partial\rho}{\partial\varphi}\dfrac{\partial p}{\partial r} + \nu\left(\dfrac{\partial^2 s_1}{\partial r^2} + \dfrac{1}{r}\dfrac{\partial s_1}{\partial r}\right). \end{cases} \tag{3.11}$$

In these equations, with assumption PS.(ii), s_1 and s_2, representing the positive and negative principal strain rate, respectively, satisfy the relation $s_1 + s_2 = 0$. Additionally, ω denotes the vorticity magnitude perpendicular to the plane of the two-dimensional single vortex. Furthermore, these equations can be further simplified under assumption PS.(iii) by ignoring the density gradient $\boldsymbol{\nabla}\rho$

$$\begin{cases} \dfrac{\mathrm{d}}{\mathrm{d}t}s_1 = \nu\left(\dfrac{\partial^2 s_1}{\partial r^2} + \dfrac{1}{r}\dfrac{\partial s_1}{\partial r}\right), \\ \dfrac{\mathrm{d}}{\mathrm{d}t}s_2 = \nu\left(\dfrac{\partial^2 s_2}{\partial r^2} + \dfrac{1}{r}\dfrac{\partial s_2}{\partial r}\right), \\ \widetilde{W_{12}} \approx \dfrac{\widetilde{H_{12}^p} + \widetilde{H_{12}^b}}{s_2 - s_1} = -\dfrac{u_\varphi}{r}, \\ \dfrac{\mathrm{d}}{\mathrm{d}t}\omega = \nu\left(\dfrac{\partial^2 s_1}{\partial r^2} + \dfrac{1}{r}\dfrac{\partial s_1}{\partial r}\right). \end{cases} \tag{3.12}$$

https://doi.org/10.1017/jfm.2025.11051 Published online by Cambridge University Press

These equations suggest that the principal strain rate s_i and the associated parameters are primarily governed by the viscous effects.

Given the constant total circulation Γ_t depicted in figure 3, the analytical solution of (3.12) can be expressed as

$$\begin{cases} s_1 = \dfrac{1}{2}\left(-\dfrac{\partial u_\varphi}{\partial r} + \dfrac{u_\varphi}{r}\right) = \dfrac{\Gamma_t}{2\pi r^2}\left(1 - \exp\left(-\dfrac{r^2}{4\nu t}\right)\right) - \dfrac{\Gamma_t}{8\pi \nu t}\exp\left(-\dfrac{r^2}{4\nu t}\right), \\ \widetilde{W_{12}} = -\dfrac{u_\varphi}{r} = -\dfrac{\Gamma_t}{2\pi r^2}\left(1 - \exp\left(-\dfrac{r^2}{4\nu t}\right)\right), \\ \omega = \dfrac{\partial u_\varphi}{\partial r} + \dfrac{u_\varphi}{r} = \dfrac{\Gamma_t}{4\pi \nu t}\exp\left(-\dfrac{r^2}{4\nu t}\right), \\ \boldsymbol{e}_1 = \left(\cos\left(-\dfrac{\pi}{4} + \varphi\right), \sin\left(-\dfrac{\pi}{4} + \varphi\right)\right). \end{cases} \tag{3.13}$$

This solution derived for the principal strain rate s_i within a single vortex aligns well with the principal strain rate obtained from Saffman's viscous vortex ring model (Saffman 1970), given by

$$u_\varphi = \frac{\Gamma_t}{2\pi r}\left(1 - \exp\left(-\frac{r^2}{4\nu t}\right)\right). \tag{3.14}$$

For the scalar gradient alignment λ_i, SDGE-λ_i as represented in (3.10) can be firstly simplified under two-dimensional flow condition

$$\begin{cases} \dfrac{\mathrm{d}}{\mathrm{d}t}\lambda_1 = -(s_1 - s_2)\left(\lambda_1\lambda_2^2 + \dfrac{\widetilde{W_{12}} + \omega/2}{s_1 - s_2}\lambda_2\right) + \dfrac{1}{\sqrt{\chi}}T_1^{others}, \\ \dfrac{\mathrm{d}}{\mathrm{d}t}\lambda_2 = (s_1 - s_2)\left(\lambda_1^2\lambda_2 + \dfrac{\widetilde{W_{12}} + \omega/2}{s_1 - s_2}\lambda_1\right) + \dfrac{1}{\sqrt{\chi}}T_2^{others}. \end{cases} \tag{3.15}$$

Moreover, in a two-dimensional flow, the alignment of the scalar gradient λ_i satisfies the relation $\lambda_1^2 + \lambda_2^2 = 1$. Therefore, using the triangular transformation

$$\lambda_1 = \cos\theta, \qquad \lambda_2 = \sin\theta. \tag{3.16}$$

Equation (3.15) can be further simplified by neglecting the high-order terms $(1/\sqrt{\chi})T_i^{others}$ in the flow structures with a large SDR value, shown as

$$\frac{\mathrm{d}}{\mathrm{d}t}\theta = \frac{s_1 - s_2}{2}(\sin 2\theta + \xi), \tag{3.17}$$

where $\xi = (\widetilde{W_{12}} + \omega/2)(1/2(s_1 - s_2))$ is the essential parameter that determines the stability of this equation (Lapeyre *et al.* 1999). With the analytical expressions for the principal strain rate s_i and the related parameters given in (3.13), ξ satisfies the relationship

$$\xi = \frac{\widetilde{W_{12}} + \omega/2}{\dfrac{1}{2}(s_1 - s_2)} = -1. \tag{3.18}$$

By transforming the angle θ and time t with the following relationships:

$$\begin{cases} \zeta = -2\theta + \dfrac{\pi}{2}, \\ \tau = \displaystyle\int_0^t 2s_1\left(t'\right)\mathrm{d}t', \end{cases} \tag{3.19}$$

https://doi.org/10.1017/jfm.2025.11051 Published online by Cambridge University Press

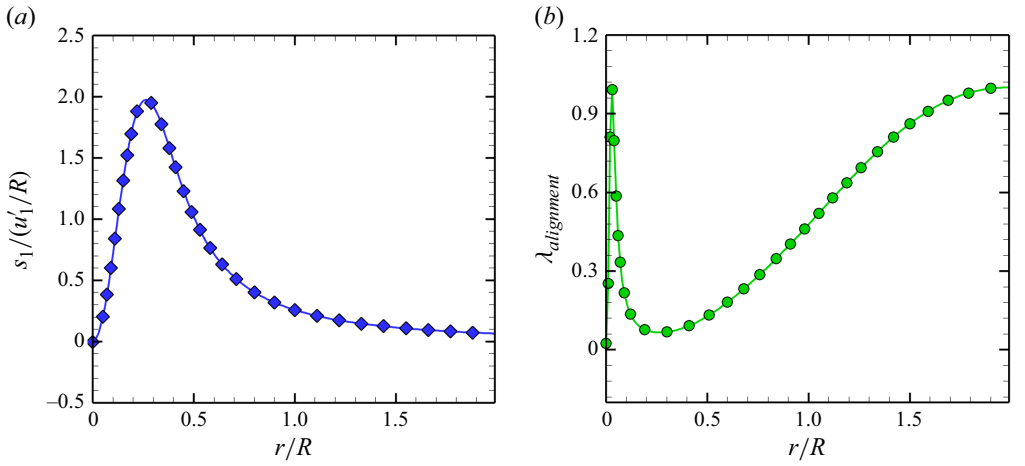


Figure 8. The examples for the distribution of (*a*) the principal strain rate and (*b*) the comprehensive alignment effect $\lambda_{alignment}$ along the radial axis in a single vortex as in (3.23). Here, the principal strain rate is normalised by the ratio between the post-shock air velocity u_1' and the radius of the helium bubble R.

then (3.17) can be can be reformulated into a simple ordinary differential equation (ODE)

$$\frac{\mathrm{d}}{\mathrm{d}\tau}\zeta = 1 - \cos\zeta. \tag{3.20}$$

The solution to this ODE is

$$\zeta = \pi + 2\arctan(\tau). \tag{3.21}$$

Thus, the analytical solution for the alignment of the scalar gradient λ_i in (3.10) is given by

$$\lambda_1 = \cos\left(-\frac{\pi}{4} + \arctan(\tau)\right), \qquad \lambda_2 = \sin\left(-\frac{\pi}{4} + \arctan(\tau)\right). \tag{3.22}$$

With the analytical solution of the SDGEs for the principal strain rate in (3.7) and the alignment of the scalar gradient in (3.10), the stretching rate, as defined in (1.5), can be determined within a single vortex as follows:

$$R_{stretch} = 2s_1\lambda_{alignment} = 4s_1\frac{\tau}{1+\tau^2}, \tag{3.23}$$

where

$$\lambda_{alignment} = 1 - 2\lambda_1^2 = 2\frac{\tau}{1+\tau^2}. \tag{3.24}$$

In this expression, $\lambda_{alignment}$ indicates the comprehensive effect of the scalar gradient alignment on the stretching rate. Examples for the distribution of the principal strain s_1 and the comprehensive alignment effect $\lambda_{alignment}$ along the radial axis under the condition of PS SBI are illustrated in figure 8. Notably, if the diffusion term in (3.6) is neglected, the analytical expression for the stretching rate in (3.23) corresponds to the algebraic growth of SDR χ

$$\frac{\mathrm{d}}{\mathrm{d}t}\chi = T^{\chi}_{stretch} = \chi R_{stretch} \quad \Rightarrow \quad \chi = \chi_0\left(1+\tau^2\right). \tag{3.25}$$

This algebraic stretching characteristic will be further elaborated on from a geometric perspective in the subsequent discussion.

https://doi.org/10.1017/jfm.2025.11051 Published online by Cambridge University Press

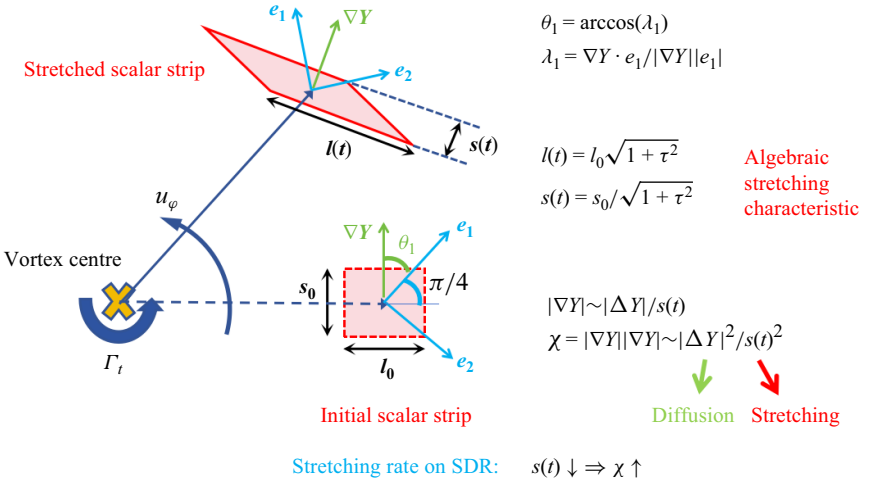


Figure 9. Schematic illustration of the impact of the stretching rate $R_{stretch}$ on SDR growth in a single vortex. Within this diagram, the area outlined by the red dashed line represents the initial scalar strip, while the area enclosed by the red solid line denotes the deformed scalar strip as influenced by the stretching effect of the single vortex. The line perpendicular to the scalar gradient represents the scalar strip length $l(t)$, while the parallel line represents the scalar strip width $s(t)$. According to the estimation for SDR $\chi \sim |\Delta Y|^2/s(t)^2$, the influence of the stretching rate on SDR growth is reflected in the continuous decrease in the scalar strip width $s(t)$.

3.4. *Physical meaning of the algebraic stretching rate: from the geometric view point*

This subsection elucidates the physical meaning of the analytical expression for the stretching rate R_{stetch} presented in (3.23) from the geometric viewpoint. Referring back to the governing equation for the SDR in (3.6), the stretching term $T^{\chi}_{stretch}$, from which the definition of the stretching rate $R_{stretch}$ is derived, describes the evolution of the scalar gradient magnitude ∇Y during a continuous stretching process without molecular diffusion. Figure 9 is the schematic illustrating the impact of the stretching rate $R_{stretch}$ on SDR within a single vortex.

As shown in figure 9, the initial scalar strip, with a length of l_0 and a width of s_0, undergoes deformation due to the continuous stretching effect of the single vortex. This stretching effect elongates the scalar strip to a new length $l(t)$, while compressing its width to $s(t)$ in accordance with the conservation of the scalar strip's area. The definition of the SDR, $\chi = |\nabla Y||\nabla Y|$, suggests that the essence of SDR is the square of the magnitude of the scalar gradient. Considering that the SDR for the scalar strip can be approximated by the ratio of the mass fraction difference ΔY to the width $s(t)$, expressed as $\chi \sim |\Delta Y|^2/s(t)^2$, an increase in SDR appears to stem from the reduction in the width of the deformed scalar strip $s(t)$ with a constant mass fraction difference ΔY when the diffusion process is neglected. This observation indicates how the stretching term $T^{\chi}_{stretch}$ drives the growth of SDR.

Under this schematic, the stretching of SDR can be transformed to the reduction in the width of the scalar strip. If the diffusion term T^{χ}_{diff} is neglected, the governing equation for SDR in (3.6) can be rewritten based on the estimation $\chi \sim 1/s(t)^2$

$$\frac{\mathrm{d}}{\mathrm{d}t}\chi = T^{\chi}_{stretch} = \chi R_{stretch} \quad \Rightarrow \quad \frac{\mathrm{d}}{\mathrm{d}t}\left(\frac{1}{s(t)}\right)^2 = \left(\frac{1}{s(t)}\right)^2 R_{stretch}. \tag{3.26}$$

https://doi.org/10.1017/jfm.2025.11051 Published online by Cambridge University Press

Applying the analytical expression of the stretching rate $R_{stretch}$ in (3.23), this equation becomes

$$\frac{\mathrm{d}}{\mathrm{d}t}\left(\frac{1}{s(t)}\right)^2 = \left(\frac{1}{s(t)}\right)^2 4s_1\frac{\tau}{1+\tau^2}, \tag{3.27}$$

with the analytical solution

$$s\,(t) = \frac{s_0}{\sqrt{1+\tau^2}}, \tag{3.28}$$

and the corresponding evolution of the elongation in the length of the scalar strip $l(t)$ is demonstrated by

$$l(t) = l_0\sqrt{1+\tau^2}. \tag{3.29}$$

These solutions reveal that the length $l(t)$ and the width $s(t)$ evolve in an algebraic form over time, indicating that the stretching within a single vortex displays an algebraic stretching characteristic.

Based on the derivation of the stretching behaviour of the scalar strip, the algebraic stretching characteristic is further validated using the Lagrangian method (Liang *et al.* 2019; Zhang *et al.* 2022). The morphological changes of the bubble following shock interaction, as shown in figure 4, support assumption PS.(iv), which approximates the mixing of the post-shock bubble as the mixing of a compressed semicircle composed of a series of scalar strips, as illustrated in figure 10(*a*). This approximation aligns with our previous investigation (Liu *et al.* 2022). For one of the initial scalar strips with a length l_0, perpendicular to the scalar gradient, and a width s_0, parallel to the scalar gradient, the Lagrangian particle movement results in figure 10(*c*) demonstrate the continuous elongation of the length $l(t)$ and reduction of the width $s(t)$. By comparing the lengths of the scalar strips at different radii, obtained according to the trajectories of the Lagrangian particles placed at the edge of semicircle, as shown in figure 10(*b*), with the predictions of the stretching dynamics derivation in (3.29), figure 11 demonstrates the good agreement between the Lagrangian particle movement results and theoretical predictions, thereby the algebraic stretching characteristic within a single vortex is confirmed.

4. The case of PS SBI mixing dominated by an algebraic stretching dynamics

In the previous section, the algebraic stretching characteristic within a single vortex was elucidated using the solution of the SDEGs as the preliminaries for analysing the stretching dynamics. To further investigate the role of the stretching dynamics in the context of mixing in SBI, we first examine the relatively simple scenario of mixing in PS SBI as a foundation for understanding VD mixing. In this section, the stretching dynamics of PS SBI is initially assessed. Furthermore, based on the analytical expression of the stretching rate, a PS mixing model for SDR is proposed by incorporating diffusion through the solution of the advection–diffusion equation in (2.14) along deformed scalar strips subjected to stretching, and this model is validated to accurately capture the evolution of the SDR in PS SBI. The close alignment between the SDR evolution and the model's predictions indicates that mixing in PS SBI is predominantly governed by an algebraic stretching dynamics within a single vortex.

4.1. *Verification of algebraic stretching in PS SBI*

After the shock interaction, the PS bubble attains a translational velocity V_v that is approximately equal to the post-shock velocity u_1'. By setting the origin of the cylindrical

https://doi.org/10.1017/jfm.2025.11051 Published online by Cambridge University Press

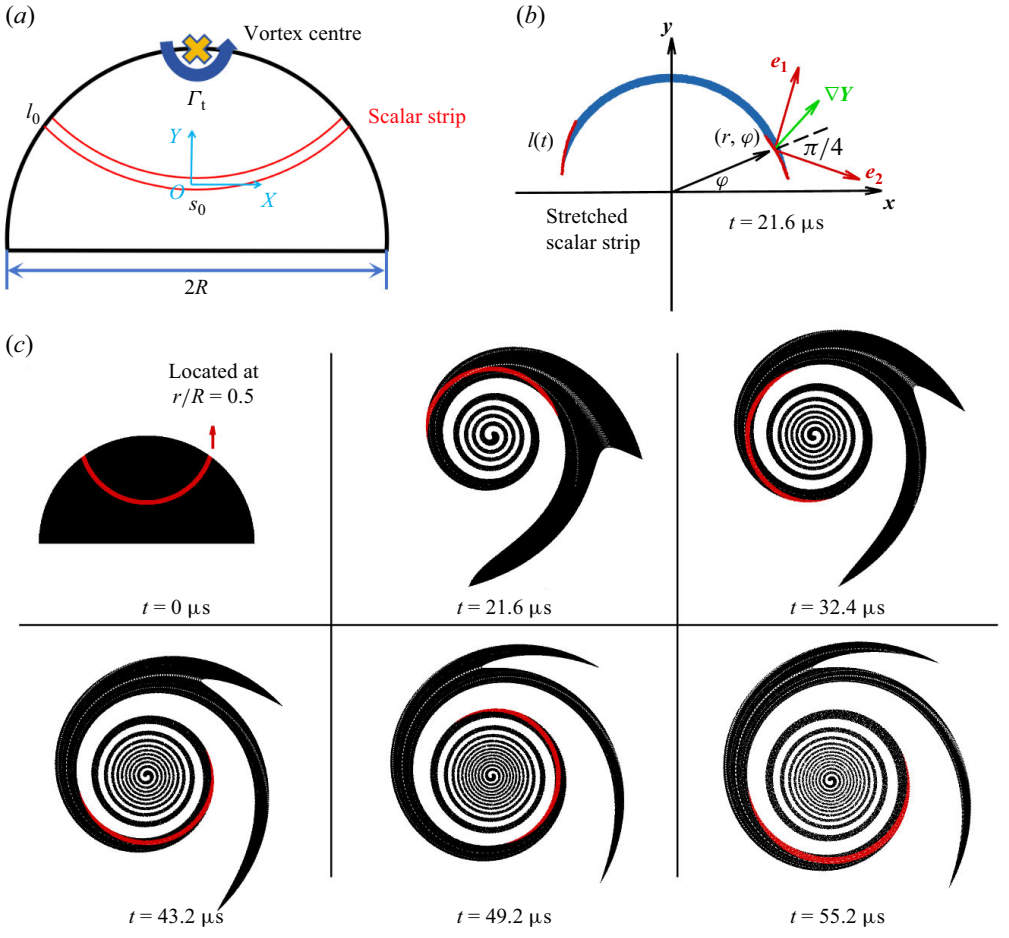


Figure 10. The schematic illustrating the validation of the algebraic stretching characteristic in a single vortex using the Lagrangian method. Referring to the previous investigation (Liu *et al.* 2022), the stretching of a post-shock bubble is approximated as a compressed semicircle composed of a series of scalar strips, each undergoing deformation due to the continuous stretching effect of the single vortex. (*a*) The distribution of initial scalar strips used to approximate the stretching process of the post-shock bubble. (*b*) An example of a stretched scalar strip, along with the corresponding strain eigenframe ($\boldsymbol{e}_1, \boldsymbol{e}_2$) and the scalar gradient. (*c*) The results of the Lagrangian particle movement for the scalar strip depicted in (*a*).

coordinates at the centre of the moving vortex (Shariff & Leonard 1992), the azimuthal velocity around the vortex can be expressed as $(u-V_v, v)$, where u represents the velocity in the x-direction and v denotes the velocity in the y-direction. In figure 12, mixing in PS SBI is passively governed by the large-scale main vortex. Given the reduction of the density difference, it is reasonable to assert that the stretching dynamics in PS SBI aligns with the single-vortex algebraic stretching discussed in § 3. This assumption is further validated by analysing the azimuthally averaged parameters along the radius

$$f\left(r,\ \varphi|_{avg}\right) = \frac{\int_{Y>0.01Y_{max}} f(r,\varphi)\mathrm{d}\varphi}{\int_{Y>0.01Y_{max}} \mathrm{d}\varphi}, \tag{4.1}$$

as illustrated by the blue circle in figure 12(*b*).

https://doi.org/10.1017/jfm.2025.11051 Published online by Cambridge University Press

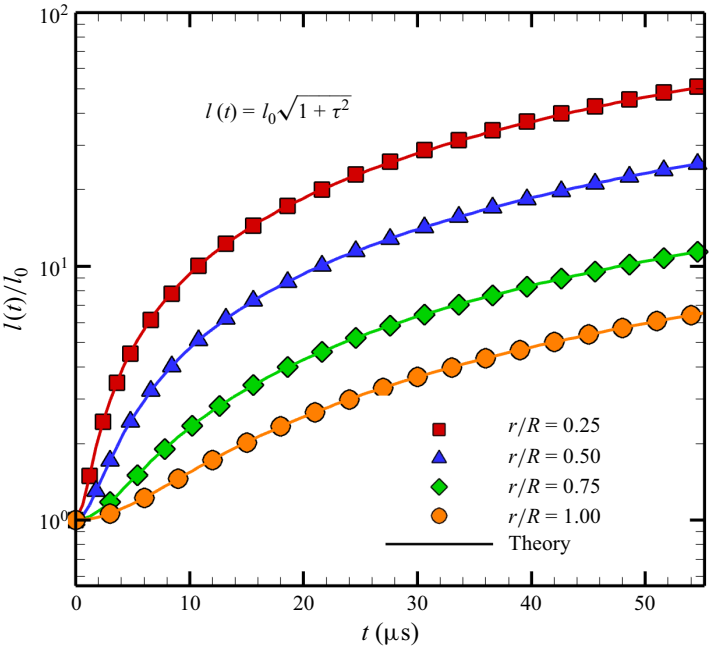


Figure 11. The comparison of the length of the scalar strip at different radii obtained from the Lagrangian particle movement results and prediction of the stretching dynamics derivation in (3.29).

Based on the single-vortex stretching dynamics described in (3.23), we first examine the principal strain rate in PS SBI. Figure 13 illustrates the distribution of the azimuthally averaged principal strain rate s_1 along the radial axis in PS SBI. With the total circulation of $\Gamma_t \approx 2.1\ \mathrm{m}^2\ \mathrm{s}^{-1}$, the analytical expression for the principal strain rate can be expressed as follows:

$$s_1 = \frac{\Gamma_t}{2\pi r^2}\left(1 - \exp\left(-\frac{r^2}{4\nu(t+t_0)}\right)\right) - \frac{\Gamma_t}{8\pi\nu(t+t_0)}\exp\left(-\frac{r^2}{4\nu(t+t_0)}\right), \tag{4.2}$$

where t_0 is estimated based on the scale of the vortex core (Saffman 1970)

$$\sqrt{4\nu t_0} = r(s_1^{max}) \approx 0.27R, \quad \Rightarrow \quad t_0 \approx 9.8 \times 10^{-4}\mathrm{s}. \tag{4.3}$$

Notably, since $t_0 \gg t$, the principal strain rate evolves as a nearly steady state, which corresponds with the observation of the nearly steady single vortex depicted in figure 12. The comparison shown in figure 13 demonstrates that the principal strain rate in PS SBI aligns closely with the theoretical distribution outlined in (4.2). This correspondence indicates that the stretching dynamics in PS SBI exhibits a characteristic consistent with single-vortex stretching from the first perspective of the principal strain rate.

Another important parameter for stretching dynamics is the alignment of the scalar gradient $\lambda_{alignment}$. Referring to the derivation of the SDGE-λ_i in (3.10), a significant result for the parameter $\xi = (\widetilde{W_{12}} + \omega/2)/((s_1 - s_2)/2)$, which determines the stability of SDGE-λ_i, is that ξ satisfies the relationship $\xi = -1$ within a single vortex (3.18).

The probability density function (PDF) of ξ in PS SBI is obtained from the region enclosed by the red dash-dot-dot line in figure 12, with the corresponding results shown in figure 14. Notably, the PDF curves exhibit pronounced peaks centred around $\xi = -1$. The deviations from the theoretical value of $\xi = -1$, such as the emergence of $\xi = 1$ in the early stages, can be attributed to the small discrepancies between PS SBI and an idealised

https://doi.org/10.1017/jfm.2025.11051 Published online by Cambridge University Press

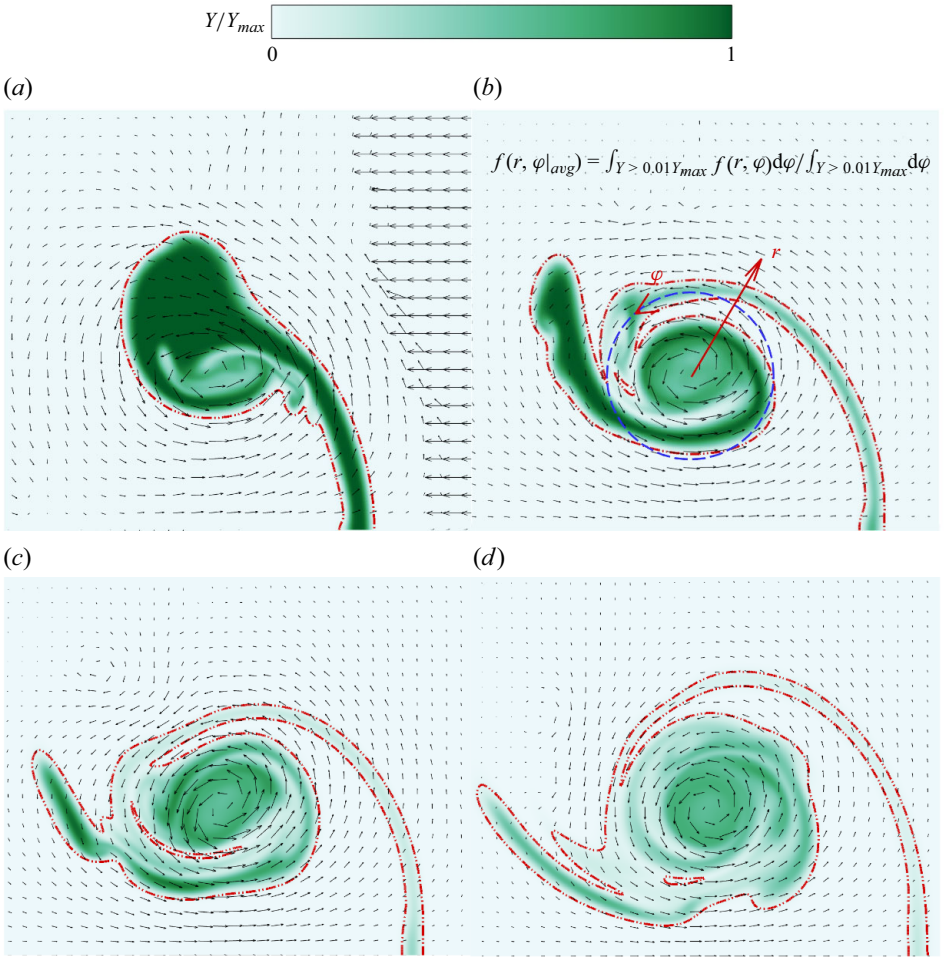


Figure 12. The distribution of the normalised mass fraction Y/Y_{max} and the relative azimuthal velocity around the vortex centre $(u - V_v, v)$ in PS SBI at (a) $t = 13.2$ µs, (b) $t = 26.4$ µs, (b) $t = 39.6$ µs, (d) $t = 52.8$ µs. The red dash-dot dot line represents the isoline where $Y = 0.01Y_{max}$.

single vortex. To evaluate whether the relationship given in (3.18) remains applicable in PS SBI, we examine if the solution of SDGE-λ_i as derived in § 3 based on (3.18), accurately describes the alignment of the scalar gradient $\lambda_{alignment}$. If (3.18) holds, the distribution of $\lambda_{alignment}$ should follow the theoretical prediction given in (3.24): $\lambda_{alignment} = 2\tau/(1+\tau^2)$, where τ is defined as $\tau = \int_0^t 2s_1(t')\mathrm{d}t'$, and the expression for s_1 is consistent with that provided in (4.2).

Figure 15 presents a comparison between the azimuthally averaged $\lambda_{alignment}$ in PS SBI and the theoretical prediction provided in (3.24). The distribution of $\lambda_{alignment}$ is accurately captured by the theory described in (3.24). The minor discrepancies observed are likely due to the intrinsic complexity of alignment dynamics described by SDGE-λ_i in (3.10), which incorporates the coupled effects of pressure and velocity gradients. These results support the validity of (3.18) in PS SBI, suggesting that the stretching dynamics within this flow exhibits characteristic consistent with single-vortex stretching from the second perspective of scalar gradient alignment.

https://doi.org/10.1017/jfm.2025.11051 Published online by Cambridge University Press

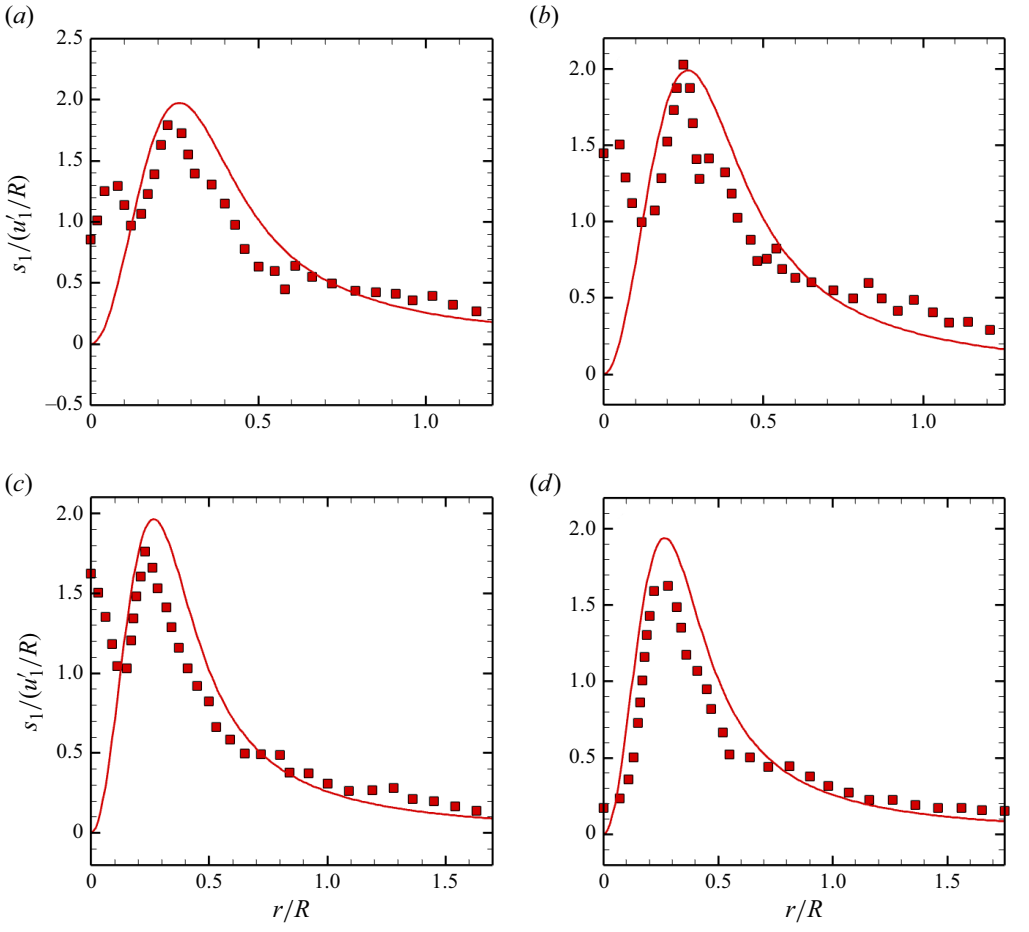


Figure 13. The distribution of the azimuthally averaged principal strain rate s_1 on the radial axis in PS SBI. The moments captured from (*a*) to (*d*) are the same as those of figure 12. The azimuthally averaged principal strain rate is plotted as the red dots, while the prediction of the theory in (4.2) is plotted as the red solid line.

4.2. *Incorporating diffusion process based on algebraic stretching rate*

The stretching dynamics in PS SBI has been shown to exhibit the characteristic of single-vortex stretching from two perspectives: the principal strain rate s_1 and the alignment of the scalar gradient $\lambda_{alignment}$. However, as indicated in the analysis of the decomposition of the material derivative of the total SDR $\mathrm{D}\langle\chi\rangle/\mathrm{D}t$ presented in figure 7, the diffusion term $\langle T^{\chi}_{diff}\rangle$ in (3.6) serves as another significant factor influencing the evolution of the SDR. Therefore, incorporating the diffusion process based on the algebraic stretching rate is essential for developing the PS mixing model for SDR $\langle\chi\rangle$.

As presented in figure 9, the estimation $\chi \sim |\Delta Y|^2/s(t)^2$ suggests that the diffusion effect reduces the SDR χ by altering the magnitude of the mass fraction difference $|\Delta Y|$. To model this diffusion effect within a post-shock cylindrical bubble, it is convenient to apply assumption PS.(iv) to assume that the mixing occurs on a compressed semicircle illustrated in figure 10. The radius of this semicircle is $\sqrt{\eta}R$, where $\eta \approx 0.42$ represents the compression rate of PS SBI. By transforming the advection–diffusion equation (2.14) into the coordinate system (O, X, Y) shown in figure 16, the equation can be

https://doi.org/10.1017/jfm.2025.11051 Published online by Cambridge University Press

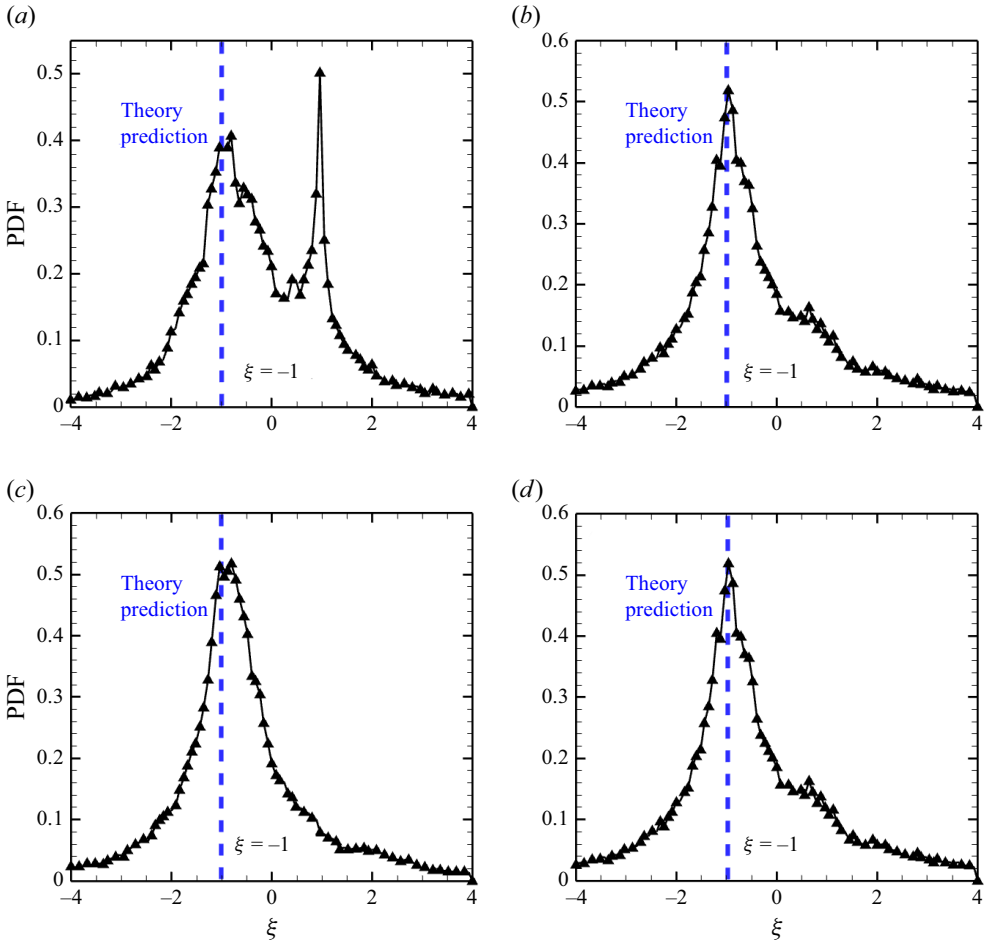


Figure 14. The probability density function (PDF) of the parameter $\xi = (\widetilde{W_{12}} + \omega/2)/((1/2)(s_1 - s_2))$ in PS SBI at the same moments as those of figure 12.

reformulated as

$$\frac{\partial Y}{\partial t} + U\frac{\partial Y}{\partial x} + V\frac{\partial Y}{\partial y} = \mathcal{D}\left(\frac{\partial^2 Y}{\partial x^2} + \frac{\partial^2 Y}{\partial y^2}\right), \tag{4.4}$$

where the origin of the (O, X, Y) system is a Lagrangian frame set on a moving scalar strip. The direction of this frame changes over time in response to the stretching motion.

On this moving coordinate, the relative velocity (U, V) can be expressed in terms of the deformation rate of the scalar strip, as described by (Villermaux 2019)

$$\begin{cases} U = \dfrac{\mathrm{d}x}{\mathrm{d}t} = \dfrac{\mathrm{d}x}{\mathrm{d}s(t)}\dfrac{\mathrm{d}s(t)}{\mathrm{d}t} = \dfrac{x}{s(t)}\dfrac{\mathrm{d}s}{\mathrm{d}t}, \\ V = \dfrac{\mathrm{d}y}{\mathrm{d}t} = \dfrac{\mathrm{d}y}{\mathrm{d}s(t)}\dfrac{\mathrm{d}s(t)}{\mathrm{d}t} = -\dfrac{y}{s(t)}\dfrac{\mathrm{d}s(t)}{\mathrm{d}t}, \end{cases} \tag{4.5}$$

where $s(t)$ denotes the instantaneous width of the scalar strip. Considering the mass fraction gradient ∇Y is predominantly aligned with the X-direction, i.e. $|\partial Y/\partial x| \gg$

https://doi.org/10.1017/jfm.2025.11051 Published online by Cambridge University Press

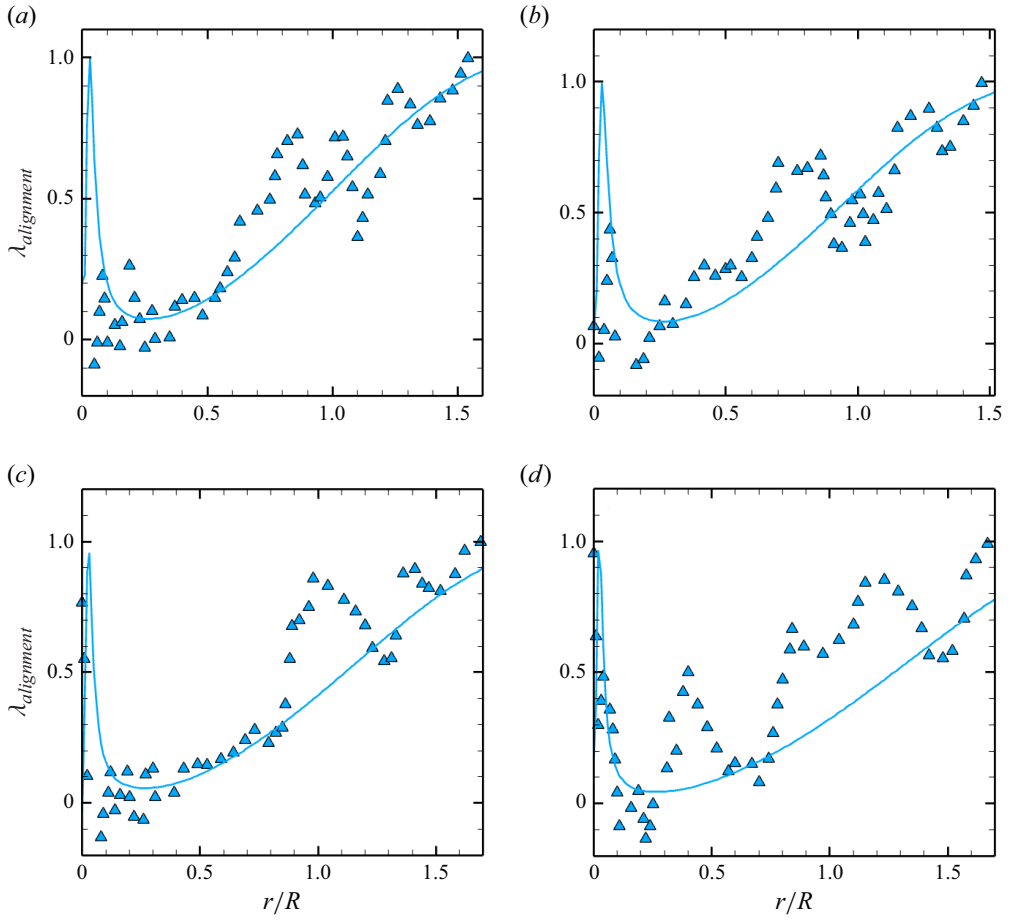


Figure 15. The distribution of the azimuthally averaged alignment of the scalar gradient $\lambda_{alignment}$ on the radial axis in PS SBI. The moments captured from (*a*) to (*d*) are the same as those of figure 12. The azimuthally averaged alignment is plotted as the blue dots, while the prediction of the theory in (3.24) is plotted as the blue solid line.

$|\partial Y/\partial y|$, (4.4) becomes

$$\frac{\partial Y}{\partial t}+\frac{x}{s(t)}\frac{\mathrm{d}s(t)}{\mathrm{d}t}\frac{\partial Y}{\partial x}=\mathcal{D}\frac{\partial^2 Y}{\partial x^2}. \tag{4.6}$$

Since the stretching dynamics is PS SBI is proved to exhibit the single-vortex stretching characteristic, the width $s(t)$ evolves algebraically as in (3.28). Using the canonical transformation introduced by Ranz (1979)

$$\begin{cases}\varsigma=\dfrac{x}{s(t)},\\ \tau^{\mathcal{D}}=\displaystyle\int_0^t\frac{\mathcal{D}\mathrm{d}t'}{s(t')^2},\end{cases} \tag{4.7}$$

then (4.6) is transformed into a simple Fourier equation

$$\frac{\partial Y}{\partial \tau^{\mathcal{D}}}=\frac{\partial^2 Y}{\partial \varsigma^2}, \tag{4.8}$$

https://doi.org/10.1017/jfm.2025.11051 Published online by Cambridge University Press

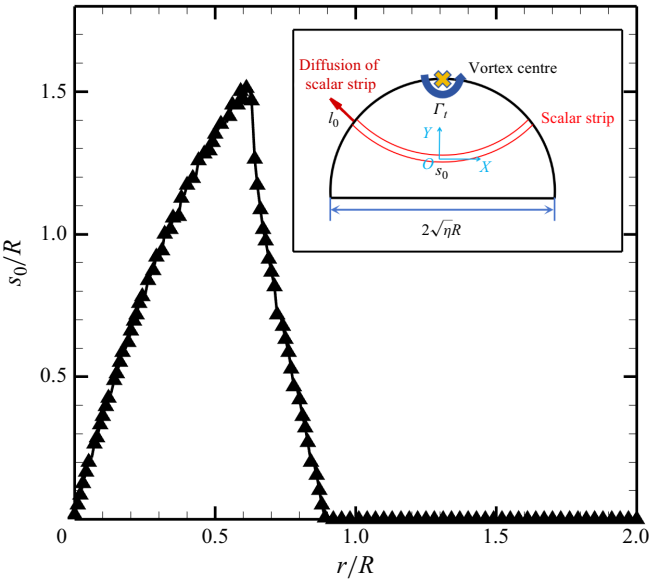


Figure 16. The schematic of the moving coordinate (O, X, Y) on the deformed scalar strips and the distribution of the related width s_0 of the initial scalar strips in the compressed semicircle depicted in figure 10.

with the initial condition specified as

$$Y(\tau^{\mathcal{D}}=0)=\begin{cases}1 & |\varsigma|\leqslant\dfrac{1}{2},\\ 0 & |\varsigma|>\dfrac{1}{2}.\end{cases} \tag{4.9}$$

Subsequently, the mass fraction in the moving coordinate frame will diffuse and spread according to the following solution:

$$Y\left(\varsigma,\tau^{\mathcal{D}}\right)=\frac{1}{2}\left[\operatorname{erf}\left(\frac{\varsigma+1/2}{2\sqrt{\tau^{\mathcal{D}}}}\right)-\operatorname{erf}\left(\frac{\varsigma-1/2}{2\sqrt{\tau^{\mathcal{D}}}}\right)\right]. \tag{4.10}$$

By considering the mass fraction difference ΔY alongside the mass fraction distribution from (4.10), the PS mixing model for the total SDR $\langle\chi\rangle$ can be proposed as

$$\langle\chi\rangle=\int\left(\int_{-\infty}^{+\infty}\left(\frac{\mathrm{d}Y}{\mathrm{d}x}\right)^2\mathrm{d}x\right)\mathrm{d}y=\int_0^{\sqrt{2\eta}R}\frac{1+\tau^2}{s_0}\frac{1}{\sqrt{2\pi\tau^{\mathcal{D}}}}\left(1-\mathrm{e}^{-\frac{1}{8\tau^{\mathcal{D}}}}\right)\mathrm{d}r. \tag{4.11}$$

In this model, $\tau=\int_0^t 2s_1(t')\mathrm{d}t'$ represents the transformed time corresponding to the stretching dynamics, while $\tau^{\mathcal{D}}=\int_0^t \mathcal{D}\mathrm{d}t'/s(t')^2=\int_0^t \mathcal{D}(1+\tau^2)\mathrm{d}t'/s_0^2$ indicates the transformed time according to the diffusion process.

The comparison shown in figure 17 indicates that the PS mixing model presented in (4.11) accurately predicts the evolution of the total SDR $\langle\chi\rangle$ during mixing in PS SBI, which proves that the mixing in PS SBI is predominantly governed by the algebraic stretching rate within a single vortex. Furthermore, we can notice the presence of the characteristic time t_{charac}, which delineates the mixing process into two distinct stages: when $t<t_{charac}$, the total SDR $\langle\chi\rangle$ increases to its peak value; subsequently, for $t\geqslant t_{charac}$, it transitions into the decay stage. The existence of this characteristic time and the two distinct mixing stages can be explained through two-stage approximation of (4.11).

https://doi.org/10.1017/jfm.2025.11051 Published online by Cambridge University Press

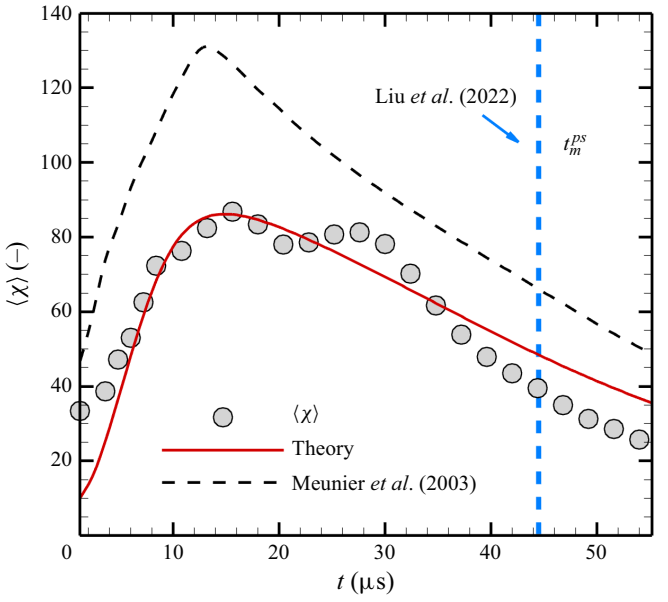


Figure 17. Comparison of the evolution of total SDR $\langle\chi\rangle$ in PS SBI with theoretical predictions: the red solid line represents the prediction from the PS mixing model in (4.11), and the black dashed line denotes the two-stage approximation from (4.15) and (4.16), which aligns with the approximation of SDR by Meunier & Villermaux (2003). The blue line indicates the PS mixing time t_m^{ps} obtained from the previous research (Liu *et al.* 2022).

In relation to the transformed time associated with the stretching dynamics, defined as $\tau = \int_0^t 2s_1(t')\mathrm{d}t'$, and given the nearly steady principal strain rate s_1 illustrated in figure 4.2, τ can be approximated as

$$\tau \approx 2s_1 t. \tag{4.12}$$

Consequently, the width of the scalar strips evolves according to

$$s(t) = \frac{s_0}{\sqrt{1+\tau^2}} = \frac{s_0}{\sqrt{1+4s_1^2t^2}}, \tag{4.13}$$

which simplifies the expression for the transformed time related to diffusion $\tau^{\mathcal{D}}$ as follows:

$$\tau^{\mathcal{D}} = \int_0^t \frac{\mathcal{D}\mathrm{d}t'}{s(t')^2} = \frac{\mathcal{D}}{s_0^2}\left(t + \frac{4}{3}s_1^2t^3\right) \approx \frac{4}{3}\frac{\mathcal{D}}{s_0^2}s_1^2t^3. \tag{4.14}$$

In the context of (4.11), if $\tau^{\mathcal{D}} < 1/8$, i.e. $t < t_{charac} = ((3/32)(s_0^2/(s_1^2\mathcal{D})))^{(1/3)}$, (4.11) can be modified to

$$\begin{aligned}\langle\chi\rangle &= \int_0^{\sqrt{2\eta}R} \frac{1+\tau^2}{s_0}\frac{1}{\sqrt{2\pi\tau^{\mathcal{D}}}}\left(1-\mathrm{e}^{-\frac{1}{8\tau^{\mathcal{D}}}}\right)\mathrm{d}r \\ &\approx \int_0^{\sqrt{2\eta}R} \frac{1+\tau^2}{s_0}\frac{1}{\sqrt{2\pi\tau^{\mathcal{D}}}}\mathrm{d}r \approx \int_0^{\sqrt{2\eta}R}\sqrt{\frac{6}{\pi\mathcal{D}}}s_1 t^{\frac{1}{2}}\mathrm{d}r,\end{aligned} \tag{4.15}$$

indicating the growth stage of $\langle\chi\rangle$. During this phase, the growth of $\langle\chi\rangle$ arises from the dominance of the stretching effect $(1+\tau^2)/s_0$ in the PS mixing process. Conversely, if $\tau^{\mathcal{D}} \geqslant 1/8$, i.e. $t \geqslant t_{charac} = ((3/32)(s_0^2/(s_1^2\mathcal{D})))^{(1/3)}$, the equation transforms to

https://doi.org/10.1017/jfm.2025.11051 Published online by Cambridge University Press

$$\begin{aligned}\langle\chi\rangle &= \int_0^{\sqrt{2\eta}R} \frac{1+\tau^2}{s_0}\frac{1}{\sqrt{2\pi\tau^{\mathcal{D}}}}\left(1-\mathrm{e}^{-\frac{1}{8\tau^{\mathcal{D}}}}\right)\mathrm{d}r \\ &\approx \int_0^{\sqrt{2\eta}R} \frac{1+\tau^2}{s_0}\frac{1}{\sqrt{2\pi\tau^{\mathcal{D}}}}\frac{1}{8\tau^{\mathcal{D}}}\mathrm{d}r \approx \int_0^{\sqrt{2\eta}R} \frac{3}{16}\sqrt{\frac{3}{2\pi}}\frac{s_0^2}{\mathcal{D}^{\frac{3}{2}}s_1 t^{\frac{5}{2}}}\mathrm{d}r,\end{aligned} \tag{4.16}$$

which characterises the decay stage of $\langle\chi\rangle$. In this phase, the decay of $\langle\chi\rangle$ stems from the predominance of the diffusion effect $1/\sqrt{2\pi\tau^{\mathcal{D}}}(1-\mathrm{e}^{-1/8\tau^{\mathcal{D}}})$ in the PS mixing process. The rationale of these equation simplifications is provided in the supplementary material. Notably, the two-stage approximations of the PS mixing model are consistent with the approximations for $\langle\chi\rangle$ in the previous study on single-vortex PS mixing (Meunier & Villermaux 2003). As shown in figure 17, the two-stage approximation of the PS mixing model in (4.15) and (4.16) accurately captures the trends of SDR evolution during both the growth and decay stages, while still overestimating the evolution of SDR. Compared with this previous estimation of SDR, the PS mixing model effectively synthesises the stretching dynamics and diffusion effects in (3.6), providing a robust predictive framework for the evolution of $\langle\chi\rangle$. Furthermore, compared with the mixing time for PS SBI predicted by the mixing time model in our earlier work (Liu *et al.* 2022), indicated by the blue line in figure 17, the PS mixing model offers a more detailed description of the evolution of mixing indicator, representing a significant advancement over the theory for mixing time prediction.

5. The case of VD SBI mixing modified by VD effects from perspectives of stretching and diffusion

According to the distribution of the azimuthal velocity around the vortex centre, figure 18 illustrates that the mixing in VD SBI is also predominantly governed by the large-scale primary vortex as in PS SBI. However, even with the nearly identical total circulation Γ_t and the compression rate η between VD and PS SBI shown in figure 3, significant difference remains in the evolution of the mean SDR $\langle\chi\rangle$, as depicted in figure 5. This suggests that, in comparison with PS mixing based on the single-vortex stretching dynamics, additional VD effects challenge the extension of the PS mixing model to VD mixing. The primary objective of this section is to investigate these VD effects from two perspectives of stretching and diffusion, and propose a VD mixing model capable of accurately capturing the evolution of SDR in VD SBI. Through the development of this VD mixing model, the quantitative relationship between the stretching dynamics and single-vortex VD mixing is established.

5.1. *Secondary baroclinic effect on stretching dynamics in VD SBI*

This section examines whether the stretching dynamics in VD SBI manifests the same single-vortex stretching characteristic as observed in PS SBI. Specifically, the azimuthally averaged principal strain rate s_1 in VD SBI is compared with the predictions of single-vortex stretching model as outlined in (4.2). As illustrated in figure 19, the current single-vortex stretching model underestimates s_1 in VD SBI. In deriving the distribution of s_1 for the single vortex, the application of assumption PS.(iii) neglected the density gradient $\nabla\rho$, leading to an oversimplified SDGE-s_i in (3.12), where only viscous effect is considered. Therefore, the inclusion of the baroclinic term, $(-1/2\rho)(1/r)(\partial\rho/\partial\varphi)(\partial p/\partial r)$, as outlined in (3.11), should be reconsidered in the analysis of VD SBI to provide a more accurate depiction of the principal strain rate s_1. Notably, the governing equation for s_1 shares the same mathematical structure as that for vorticity ω. Thus, the influence of

https://doi.org/10.1017/jfm.2025.11051 Published online by Cambridge University Press

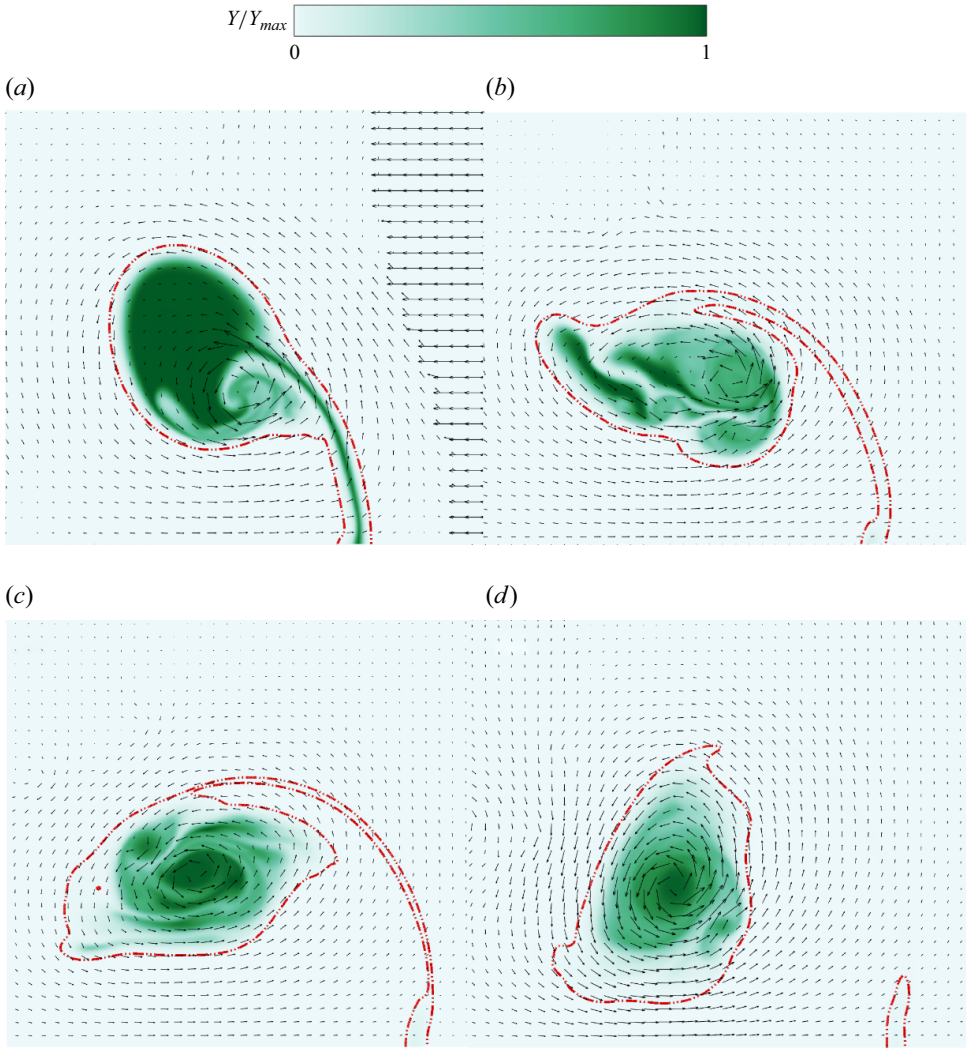


Figure 18. The distribution of the normalised mass fraction Y/Y_{max} and the relative azimuthal velocity around the vortex centre $(u - V_v, v)$ in VD SBI at same moments as those of PS SBI in figure 12.

the baroclinic term can be reflected by SBV, a canonical phenomenon in VD mixing, as reported in several studies (Peng *et al.* 2021*a*,*b*; Liu *et al.* 2022). As shown in figure 20, SBV manifests as a vortex-bilayer structure characterised by dominant negative vorticity and intensified positive vorticity. This structure is quantitatively described using the positive and negative circulation, defined as follows, consistent with prior investigations (Peng *et al.* 2003; Niederhaus *et al.* 2008):

$$\begin{cases} \Gamma^{+} = \iint_{\omega>0} \omega \mathrm{dV}, \\ \Gamma^{-} = \iint_{\omega<0} \omega \mathrm{dV}. \end{cases} \tag{5.1}$$

Figure 20(*b*) describes the evolution of positive and negative circulations: prior to the time $t_{sbv} \approx 7.2$ µs, the shock interaction with the bubble triggers the formation of the primary vortex. After $t > t_{sbv}$, the growth of positive and negative circulations Γ^{+} and Γ^{-} signifies

https://doi.org/10.1017/jfm.2025.11051 Published online by Cambridge University Press

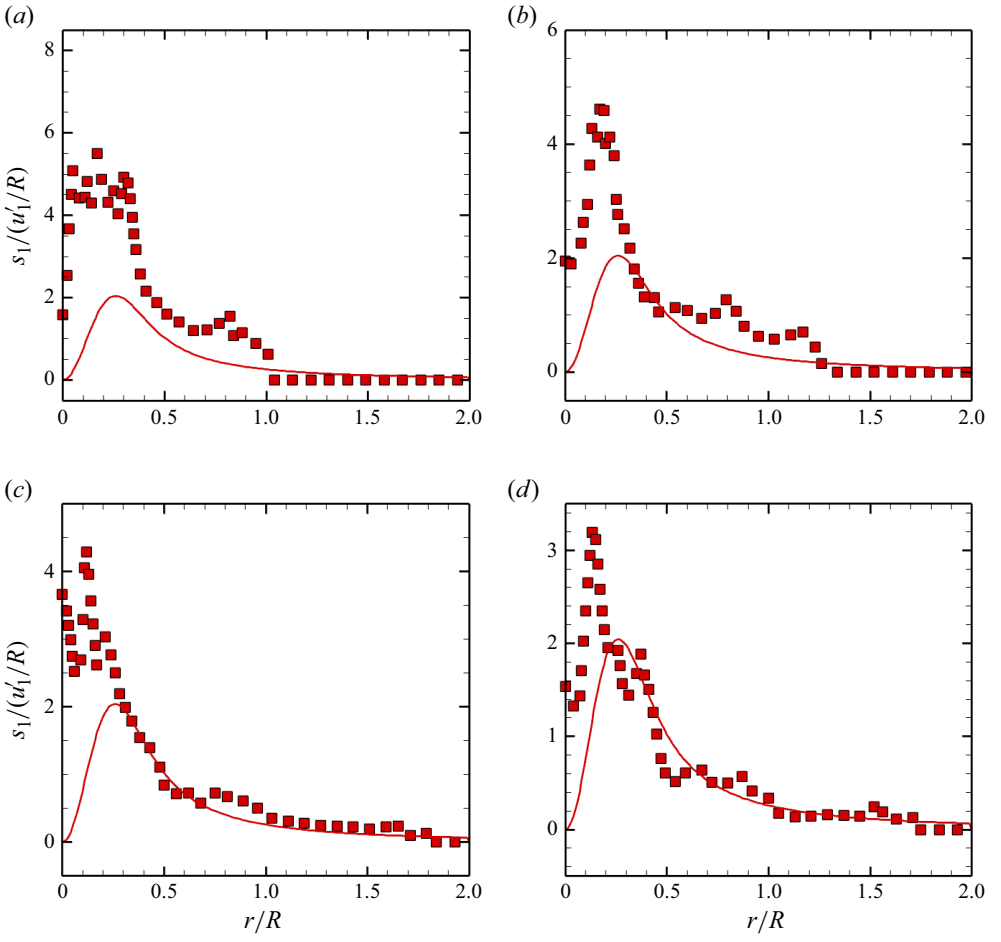


Figure 19. The distribution of the azimuthally averaged principal strain rate s_1 on the radial axis in VD SBI. The moments captured from (*a*) to (*d*) are the same as those of figure 18. The azimuthally averaged principal strain rate is plotted as the red dots, while the prediction of the single-vortex stretching theory in (4.2) is plotted as the red solid line.

the emergence of SBV. According to the fact that the positive circulation is the sum of the total circulation and the baroclinic circulation composed of SBV

$$\Gamma^{+} = \Gamma_t + \Gamma_{sbv}, \tag{5.2}$$

the principal strain rate s_1 in VD SBI can be characterised by the combination of the strain rate arising from the primary vortex s_1^{ps} and that induced by the secondary baroclinic effect $s_1^{b,v}$

$$s_1 = s_1^{ps} + s_1^{b,v}, \tag{5.3}$$

where s_1^{ps} is determined by the single-vortex principal strain rate as described in (4.2). Therefore, accurate modelling of $s_1^{b,v}$ is essential to providing a precise description of the principal strain rate s_1 in VD SBI.

https://doi.org/10.1017/jfm.2025.11051 Published online by Cambridge University Press

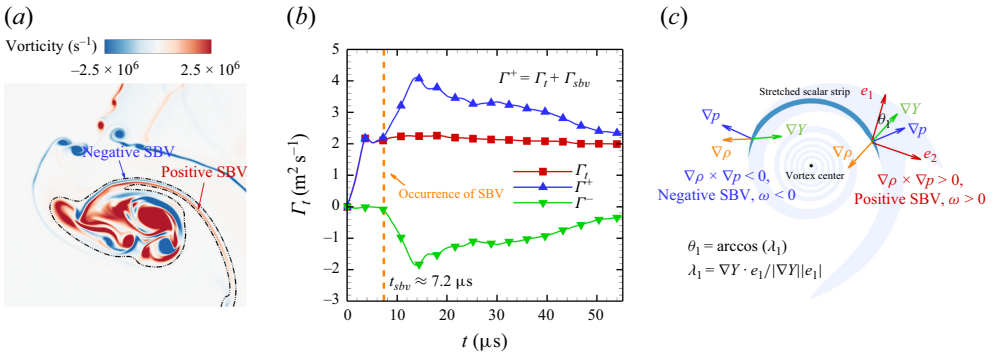


Figure 20. Schematic of the SBV in VD SBI, including (*a*) an example of the SBV distribution in VD SBI at $t = 21.6$ μs; (*b*) the evolution of the total circulation Γ_t, the positive circulation Γ^+, and negative circulation Γ^-; and (*c*) the geometric relationship related to the generation of SBV.

Considering the linearity of the governing equation for the principal strain rate as specified in (3.11), $s_1^{b,\nu}$ satisfies the following equation:

$$\frac{\mathrm{d}}{\mathrm{d}t}s_1^{b,\nu} = -\frac{1}{2\rho^2}\frac{1}{r}\frac{\partial\rho}{\partial\varphi}\frac{\partial p}{\partial r} + \nu\left(\frac{\partial^2 s_1^{b,\nu}}{\partial r^2} + \frac{1}{r}\frac{\partial s_1^{b,\nu}}{\partial r}\right), \tag{5.4}$$

indicating that $s_1^{b,\nu}$ is governed by the baroclinic term $-(1/2\rho^2)(1/r)(\partial\rho/\partial\varphi)(\partial p/\partial r)$ and viscous term $\nu((\partial^2 s_1^{b,\nu}/\partial r^2) + (1/r)(\partial s_1^{b,\nu}/\partial r))$. Equation (5.4) is relatively complex, and the modelling of the secondary baroclinic strain $s_1^{b,\nu}$ can be outlined as follows.

Firstly, to simplify the analysis, the derivation initially focuses solely on the baroclinic term $-(1/2\rho^2)(1/r)(\partial\rho/\partial\varphi)(\partial p/\partial r)$

$$\frac{\mathrm{d}}{\mathrm{d}t}s_1^{b} = -\frac{1}{2\rho^2}\frac{1}{r}\frac{\partial\rho}{\partial\varphi}\frac{\partial p}{\partial r} = \frac{1}{2\rho}\left(\frac{1}{\rho}\frac{\partial p}{\partial r}\right)\left(-\frac{1}{r}\frac{\partial\rho}{\partial\varphi}\right), \tag{5.5}$$

and the solution derived from this simplification is referred to as s_1^b.

Secondly, based on the expression for s_1^b, the effect of the viscous term $\nu((\partial^2 s_1^{b,\nu}/\partial r^2) + (1/r)(\partial s_1^{b,\nu}/\partial r))$ is incorporated through a viscous correction.

In the process of modelling of the secondary baroclinic strain $s_1^{b,\nu}$, three assumptions for VD mixing are introduced to simplify the equation. These include assumptions VD.(i) and VD.(ii) for modelling the density gradient $(1/r)(\partial\rho/\partial\varphi)$ in the baroclinic term $-(1/2\rho^2)(1/r)(\partial\rho/\partial\varphi)(\partial p/\partial r)$, and assumption VD.(iii) for the viscous correction:

Assumption VD.(i): similar to previous studies of SBI (Yu *et al.* 2021) and VD buoyancy-driven turbulence (Aslangil, Livescu & Banerjee 2020), the relationship between the post-shock density and mass fraction in VD SBI can be expressed as

$$\frac{1}{\rho} = \frac{1-Y}{\rho_1'} + \frac{Y}{\rho_2'}, \tag{5.6}$$

where ρ_1' represents the post-shock air density, and ρ_2' denotes the density of helium following the shock interaction.

Assumption VD.(ii): the distribution of the mass fraction along the scalar strips, $Y(\varsigma, \tau^{\mathcal{D}}) = (1/2)[\mathrm{erf}((\varsigma + 1/2)/(2\sqrt{\tau^{\mathcal{D}}})) - \mathrm{erf}((\varsigma - 1/2)/(2\sqrt{\tau^{\mathcal{D}}}))]$, informs

https://doi.org/10.1017/jfm.2025.11051 Published online by Cambridge University Press

the evolution of the diffusion scale $\lambda_{\mathcal{D}}$ (Souzy *et al.* 2018)

$$\lambda_{\mathcal{D}}(t) = \begin{cases} s(t) = \dfrac{s_0}{\sqrt{1+\tau^2}}, & \text{if } \tau^{\mathcal{D}} < \dfrac{1}{16}, \\ 4s(t)\sqrt{\tau^{\mathcal{D}}} = \dfrac{4s_0\sqrt{\tau^{\mathcal{D}}}}{\sqrt{1+\tau^2}}, & \text{if } \tau^{\mathcal{D}} \geqslant \dfrac{1}{16}. \end{cases} \tag{5.7}$$

Assumption VD.(iii): based on the solution for s_1^b, the viscous effect on the secondary baroclinic strain $s_1^{b,\nu}$ can be incorporated through a viscous correction (Petropoulos *et al.* 2023), which is given by

$$\begin{cases} s_1^{b,\nu} = s_1^b \operatorname{erf}\left(\dfrac{1}{4\sqrt{\tau^\nu}}\right), \\ \tau^\nu \approx \dfrac{\nu}{{s_0}^2}\left[\dfrac{4}{3}{s_1^{ps}}^2 (t - t_{sbv})^3\right]. \end{cases} \tag{5.8}$$

The validation of the assumptions for VD mixing is provided in the supplementary materials.

Here, we present the derivation of s_1^b. As shown in (5.5), the baroclinic term is the product of the pressure gradient $1/\rho(\partial p/\partial r)$ and the density gradient $-1/r(\partial\rho/\partial\varphi)$. The pressure gradient, which arises from the primary vortex, can be modelled by the azimuthal velocity as specified in (3.14)

$$\frac{1}{\rho}\frac{\partial p}{\partial r} = \frac{u_\varphi^2}{r} = \frac{\Gamma_t^2}{4\pi^2 r^3}\left(1 - \exp\left(-\frac{r^2}{4\nu(t+t_0)}\right)\right)^2 \approx \frac{\Gamma_t^2}{4\pi^2 r^3}\left(1 - \exp\left(-\frac{r^2}{4\nu t_0}\right)\right)^2. \tag{5.9}$$

This expression presents the steady pressure gradient due to the relationship $t_0 \gg t$.

The modelling of the azimuthal component of the density gradient $-1/r(\partial\rho/\partial\varphi)$ requires (5.6) from assumption VD.(i). Using this relationship, the density gradient $\nabla\rho$ is expressed in terms of the scalar gradient ∇Y

$$\nabla\rho = -\rho^2\frac{\rho_1' - \rho_2'}{\rho_1'\rho_2'}\nabla Y. \tag{5.10}$$

Owing to the distribution of $\nabla\rho$ across scalar strips as depicted in figure 20(*c*), this relationship can be simplified to

$$\nabla\rho \approx -{\rho_2'}^2\frac{\rho_1' - \rho_2'}{\rho_1'\rho_2'}\nabla Y = -\rho_2'(1-\sigma)\nabla Y, \tag{5.11}$$

where $\sigma = \rho_2'/\rho_1'$ denotes the density ratio between post-shock helium and post-shock air. By applying this expression of the density gradient and the geometric schematic depicted in figure 20(*c*), the azimuthal component of the density gradient $-1/r(\partial\rho/\partial\varphi)$ is derived by projecting the scalar gradient ∇Y onto the azimuthal direction

$$-\frac{1}{r}\frac{\partial\rho}{\partial\varphi} = \rho_2'(1-\sigma)|\nabla Y|\cos\left(\theta_1 + \frac{\pi}{4}\right). \tag{5.12}$$

Based on the solution of SDGE-λ_i detailed in (3.22), specified as $\theta_1 = -(\pi/4) + \arctan(\tau)$, the azimuthal density-gradient component can be refined further to

$$-\frac{1}{r}\frac{\partial\rho}{\partial\varphi} = \rho_2'(1-\sigma)|\nabla Y|\frac{1}{\sqrt{1+\tau^2}}. \tag{5.13}$$

https://doi.org/10.1017/jfm.2025.11051 Published online by Cambridge University Press

Moreover, the magnitude of the scalar gradient ∇Y in this formulation is expressed by the averaged SDR over the scalar strips

$$|\nabla Y| \approx \sqrt{\overline{\chi}}, \qquad \overline{\chi} = \int_{-\infty}^{+\infty} \left(\frac{\mathrm{d}Y}{\mathrm{d}x}\right)^2 \mathrm{d}x/\lambda_{\mathcal{D}} = \frac{1}{s(t)} \int_{-\infty}^{+\infty} \left(\frac{\mathrm{d}Y}{\mathrm{d}\varsigma}\right)^2 \mathrm{d}\varsigma/\lambda_{\mathcal{D}}. \tag{5.14}$$

Here, the mass fraction is presumed to follow the distribution described in (4.10) on the scalar strips, specified as: $Y(\xi, \tau^{\mathcal{D}}) = (1/2)[\mathrm{erf}(\xi + 1/2)/(2\sqrt{\tau^{\mathcal{D}}}) - \mathrm{erf}(\xi - 1/2)/(2\sqrt{\tau^{\mathcal{D}}})]$, and the diffusion scale $\lambda_{\mathcal{D}}$ is determined using (5.7) from assumption VD.(ii). With the expression of $\lambda_{\mathcal{D}}$ in (5.7), the averaged SDR on scalar strips can be rewritten as

$$\overline{\chi} = \begin{cases} \dfrac{1+\tau^2}{s_0^2} \dfrac{1}{\sqrt{2\pi\tau^{\mathcal{D}}}} \left(1 - \mathrm{e}^{-\frac{1}{8\tau^{\mathcal{D}}}}\right), & \text{if } \tau^{\mathcal{D}} < \dfrac{1}{16}, \\ \dfrac{1+\tau^2}{4s_0^2\tau^{\mathcal{D}}} \dfrac{1}{\sqrt{2\pi}} \left(1 - \mathrm{e}^{-\frac{1}{8\tau^{\mathcal{D}}}}\right), & \text{if } \tau^{\mathcal{D}} \geqslant \dfrac{1}{16}, \end{cases} \tag{5.15}$$

which can be further simplified considering the distinct stages of SDR evolution, following approximations similar to (4.15) and (4.16). The simplified form is given by

$$\overline{\chi} = \begin{cases} \dfrac{1+\tau^2}{s_0^2} \dfrac{1}{\sqrt{2\pi\tau^{\mathcal{D}}}}, & \text{if } \tau^{\mathcal{D}} < \dfrac{1}{8}, \\ \dfrac{1+\tau^2}{4s_0^2\tau^{\mathcal{D}}} \dfrac{1}{\sqrt{2\pi}} \dfrac{1}{8\tau^{\mathcal{D}}}, & \text{if } \tau^{\mathcal{D}} \geqslant \dfrac{1}{8}. \end{cases} \tag{5.16}$$

Combining the expressions for the pressure gradient from (5.9) and density gradient from (5.13), the baroclinic term specified in (5.5) can be reformulated using the approximation $\tau^{\mathcal{D}} = (\mathcal{D}/s_0^2)(4s_1^{ps2}t^3/3)$, yielding

$$\begin{aligned} &-\frac{1}{2\rho^2}\frac{1}{r}\frac{\partial\rho}{\partial\varphi}\frac{\partial p}{\partial r} \\ &= \begin{cases} \dfrac{\Gamma_t^2}{16\pi^2 r^3}\left(1 - \exp\left(-\dfrac{r^2}{4\nu t_0}\right)\right)^2 (1-\sigma) \dfrac{1}{\left(\dfrac{8\pi\mathcal{D}}{3}\right)^{\frac{1}{4}} \left(s_0 s_1^{ps}\right)^{\frac{1}{2}}} t^{-\frac{3}{4}}, & \text{if } t < t_{charac}, \\ \dfrac{3\Gamma_t^2}{256\sqrt{2}\pi^2 r^3}\left(1 - \exp\left(-\dfrac{r^2}{4\nu t_0}\right)\right)^2 (1-\sigma) \dfrac{s_0}{(2\pi)^{\frac{1}{4}}\mathcal{D} s_1^{ps2} t^3}, & \text{if } t \geqslant t_{charac}, \end{cases} \end{aligned} \tag{5.17}$$

where $t_{charac} = (3s_0/(32\mathcal{D}s_1^{ps2}))^{(1/3)}$ is determined from $\tau^{\mathcal{D}} = 1/8$.

Noticing that figure 20(*b*) illustrates the presence of SBV after $t > t_{sbv}$, the solution to the governing equation for s_1^b in (5.5) should consider the emergence time t_{sbv}:

if $t_{charac} < t_{sbv}$

$$s_1^b = \frac{3\Gamma_t^2}{512\sqrt{2}\pi^2 r^3}\left(1 - \exp\left(-\frac{r^2}{4\nu t_0}\right)\right)^2 (1-\sigma) \frac{s_0}{(2\pi)^{\frac{1}{4}}\mathcal{D} s_1^{ps2}} \left(\frac{1}{t_{sbv}^2} - \frac{1}{t^2}\right), \tag{5.18}$$

https://doi.org/10.1017/jfm.2025.11051 Published online by Cambridge University Press

if $t_{charac} \geqslant t_{sbv}$

$$s_1^b = \begin{cases} \dfrac{\Gamma_t^2}{4\pi^2 r^3}\left(1-\exp\left(-\dfrac{r^2}{4\nu t_0}\right)\right)^2 \dfrac{1}{\left(\dfrac{8\pi\mathcal{D}}{3}\right)^{\frac{1}{4}}\left(s_0 s_1^{ps}\right)^{\frac{1}{2}}}\left(t^{\frac{1}{4}}-t_{sbv}{}^{\frac{1}{4}}\right), & \text{if } t < t_{charac}, \\ s_1^b|_0 - \dfrac{3\Gamma_t^2}{512\sqrt{2}\pi^2 r^3}\left(1-\exp\left(-\dfrac{r^2}{4\nu t_0}\right)\right)^2 (1-\sigma)\dfrac{s_0}{(2\pi)^{\frac{1}{4}}\mathcal{D}s_1^{ps2}}\dfrac{1}{t^2}, & \text{if } t \geqslant t_{charac}, \end{cases} \tag{5.19}$$

where $s_1^b|_0$ is proposed to ensure the continuity of this solution. Following this solution for s_1^b, the viscous effect described in (5.4) is incorporated using the viscous correction from assumption VD.(iii). The rationale of the equation simplifications applied for deriving the secondary baroclinic principal strain $s_1^{b,\nu}$ is provided in the supplementary material.

Based on the analytical expressions for the principal strain induced by the secondary baroclinic effect $s_1^{b,\nu}$ and the principal strain induced by the primary vortex s_1^{ps}, the principal strain rate in VD SBI s_1 can be articulated as follows:

$$\begin{cases} s_1 = s_1^{ps} + s_1^{b,\nu}, \\ s_1^{ps} = \dfrac{\Gamma_t}{2\pi r^2}\left(1-\exp\left(-\dfrac{r^2}{4\nu(t+t_0)}\right)\right) - \dfrac{\Gamma_t}{8\pi\nu(t+t_0)}\exp\left(-\dfrac{r^2}{4\nu(t+t_0)}\right), \\ s_1^{b,\nu} = s_1^b \operatorname{erf}\left(\dfrac{1}{4\sqrt{\tau^\nu}}\right). \end{cases} \tag{5.20}$$

Figure 21 compares the azimuthally averaged principal strain rate s_1 in VD SBI with the prediction of single-vortex theory for s_1^{ps} from (4.2), alongside the prediction for s_1 from (5.20). This comparison underscores that (5.20) effectively captures the distribution of s_1 in VD SBI.

Following the examination of the principal strain rate s_1, the alignment of the scalar gradient $\lambda_{alignment}$ is further analysed with respect to the stretching dynamics in VD SBI. A critical observation in PS SBI is the behaviour of the parameter ξ (3.18): the distribution of ξ typically centres around -1, as illustrated in figure 14. This behaviour is similarly investigated in the context of VD SBI. The PDF of ξ in VD SBI is displayed in figure 22, it is evident that the peaks of the PDF curves cluster around $\xi = -1$. This consistency suggests that the $\xi = -1$ feature is not significantly altered by the baroclinic effect and remains applicable in VD SBI scenarios. Consequently, the derivation of SDGE-λ_i outlined in § 3 remains appropriate for analysing the alignment of the scalar gradient $\lambda_{alignment}$ in VD SBI. The distribution of $\lambda_{alignment}$ is expected to follow (3.24): $\lambda_{alignment} = 2\tau/(1+\tau^2)$, where the expression for s_1 is altered from s_1^{ps} in PS SBI to $s_1^{ps} + s_1^{b,\nu}$ in VD SBI

$$\begin{cases} \tau = \displaystyle\int_0^t 2s_1(t')\,\mathrm{d}t', \\ s_1 = s_1^{ps} + s_1^{b,\nu}. \end{cases} \tag{5.21}$$

Therefore, the secondary baroclinic effect on $\lambda_{alignment}$ is captured by the additional principal strain $s_1^{b,\nu}$ in VD SBI. Figure 23 compares the azimuthally averaged $\lambda_{alignment}$ in VD SBI with the predictions from the single-vortex theory in (3.24), as well as those

https://doi.org/10.1017/jfm.2025.11051 Published online by Cambridge University Press

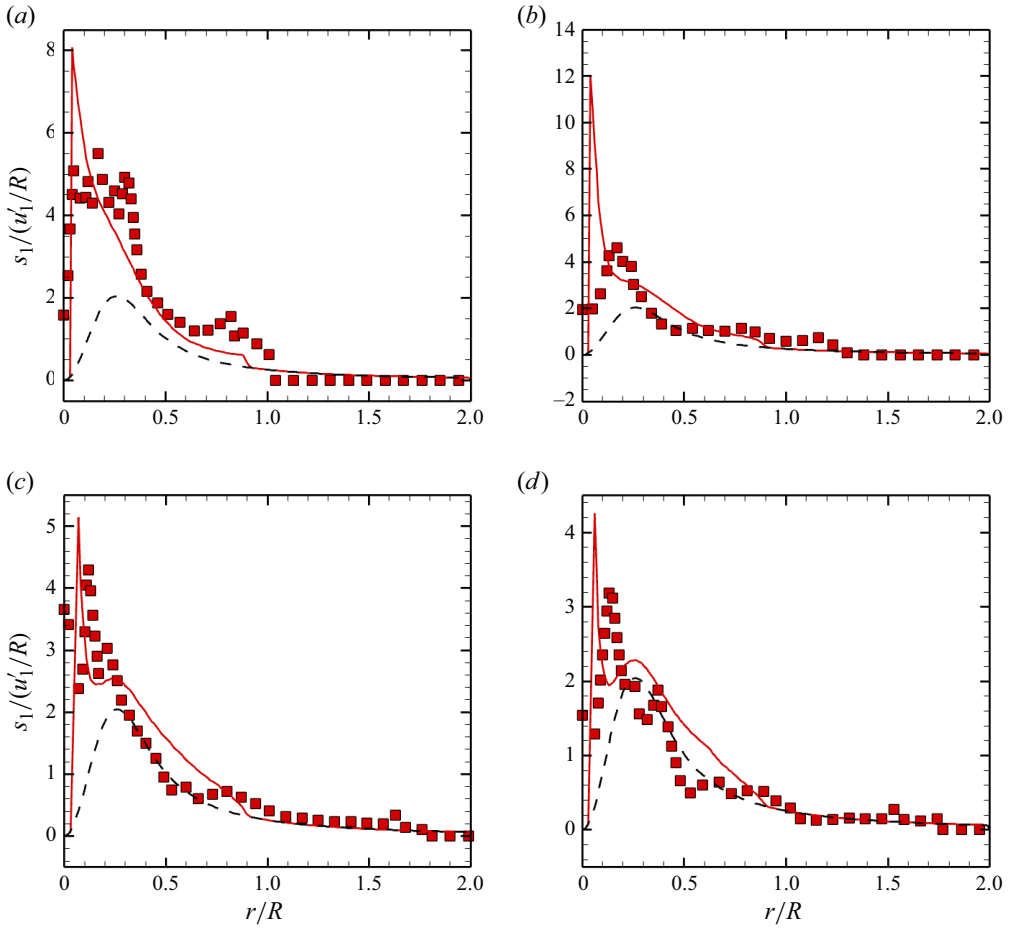


Figure 21. The distribution of the azimuthally averaged principal strain rate s_1 on the radial axis in VD SBI. The moments captured from (*a*) to (*d*) are the same as those of figure 18. The azimuthally averaged principal strain rate is plotted as the red dots, while the prediction of the single-vortex theory for s_1^{ps} in (4.2) is plotted as the black dashed line, and the prediction for s_1 in (5.20) is plotted as the red solid line.

outlined the refined predictions in (5.21). The results confirm that the distribution of $\lambda_{alignment}$ in VD SBI aligns closely with the theoretical prediction by (5.21).

By examining the stretching dynamics from two perspectives, the principal strain s_1 and the alignment of the scalar gradient $\lambda_{alignment}$, it is evident that the effects of the baroclinic term in VD SBI are comprehensively captured by the combination of (5.20) and (5.21). These equations for s_1 and $\lambda_{alignment}$ confirm the preservation of the same algebraic stretching characteristic in VD SBI with that observed in PS SBI, which means that the width of the scalar strip $s(t)$ in VD SBI evolves according to (3.28): $s(t) = s_0/\sqrt{1+\tau^2}$. The only difference between PS SBI and VD SBI lies in the expression for the principal strain s_1, as it appears in the definition of $\tau = \int_0^t 2s_1(t')\mathrm{d}t'$. Based on the description of the scalar strip width in VD SBI, the mixing model incorporating only the secondary baroclinic effect (SBE) on the stretching dynamics is modified as

$$\langle \chi \rangle = \int_0^{\sqrt{2\eta}R} \frac{1+\tau^2}{s_0} \frac{1}{\sqrt{2\pi\tau^{\mathcal{D}}}} \left(1 - \mathrm{e}^{-\frac{1}{8\tau^{\mathcal{D}}}}\right) \mathrm{d}r, \tag{5.22}$$

https://doi.org/10.1017/jfm.2025.11051 Published online by Cambridge University Press

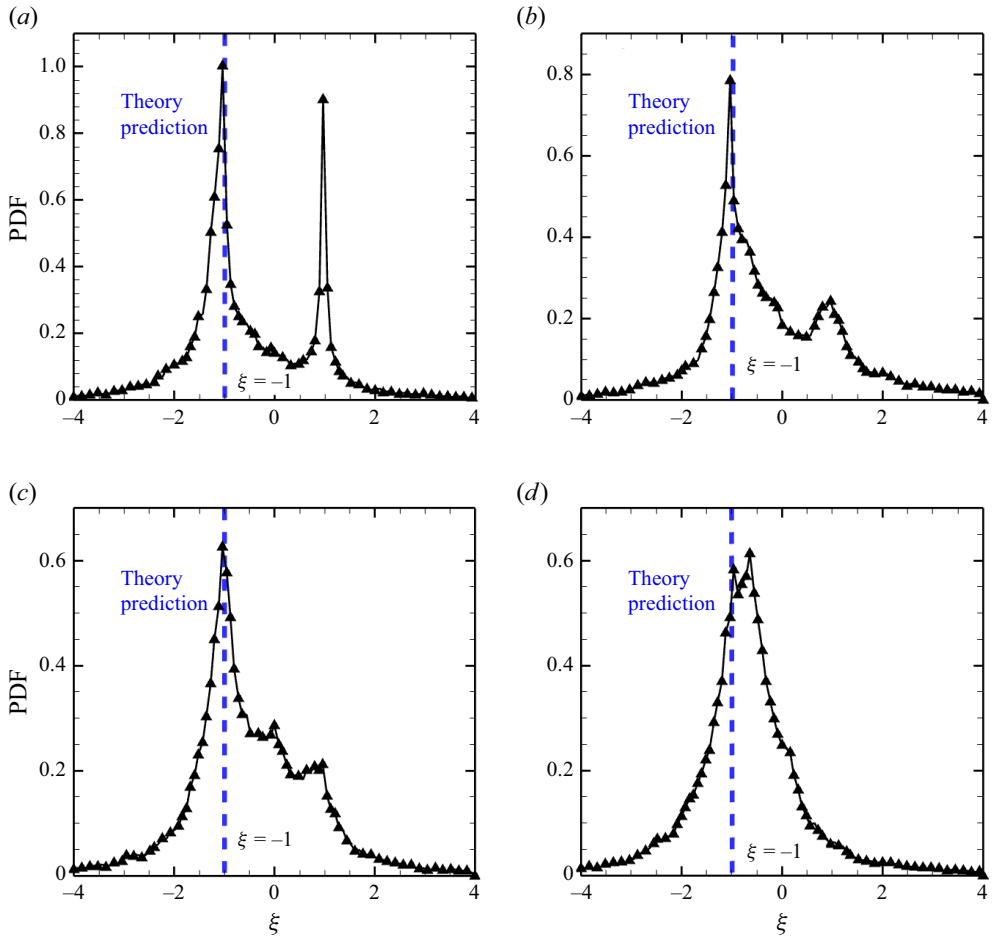


Figure 22. The PDF of the parameter $\xi = (\widetilde{W_{12}} + \omega/2)/((1/2)(s_1 - s_2))$ in VD SBI at the same moments as those of figure 18.

where $\tau = \int_0^t 2s_1(t')\mathrm{d}t'$, $s_1 = s_1^{ps} + s_1^{b,v}$. However, the prediction of the SBE model still does not align with the observed SDR evolution in VD SBI, as will be further discussed in figure 24.

5.2. *Density source effect on diffusion process in VD SBI*

The stretching dynamics in VD SBI has been shown to be affected by the baroclinic effect, while the algebraic stretching characteristic is still retained. The derivation of the VD mixing model for total SDR $\langle\chi\rangle$ should consider another VD mixing feature, specifically transitioning from the advection–diffusion equation used in PS SBI (2.14), to the multi-component transport equation applicable to VD SBI (2.15). In § 2, the density variation in VD SBI introduces a density source term $\mathcal{D}/\rho((\partial\rho/\partial x_j)(\partial Y/\partial x_j))$ in (2.16). This section investigates the impact of this term on the diffusion process.

For the VD advection–diffusion equation (2.16), using the relation between the density gradient $\nabla\rho$ and scalar gradient ∇Y in (5.11), this equation can be reformulated as

$$\frac{\partial Y}{\partial t} + u_j\frac{\partial Y}{\partial x_j} = -\mathcal{D}\,(1-\sigma)\,\frac{\partial Y}{\partial x_j}\frac{\partial Y}{\partial x_j} + \mathcal{D}\frac{\partial^2 Y}{\partial x_j^2}. \tag{5.23}$$

https://doi.org/10.1017/jfm.2025.11051 Published online by Cambridge University Press

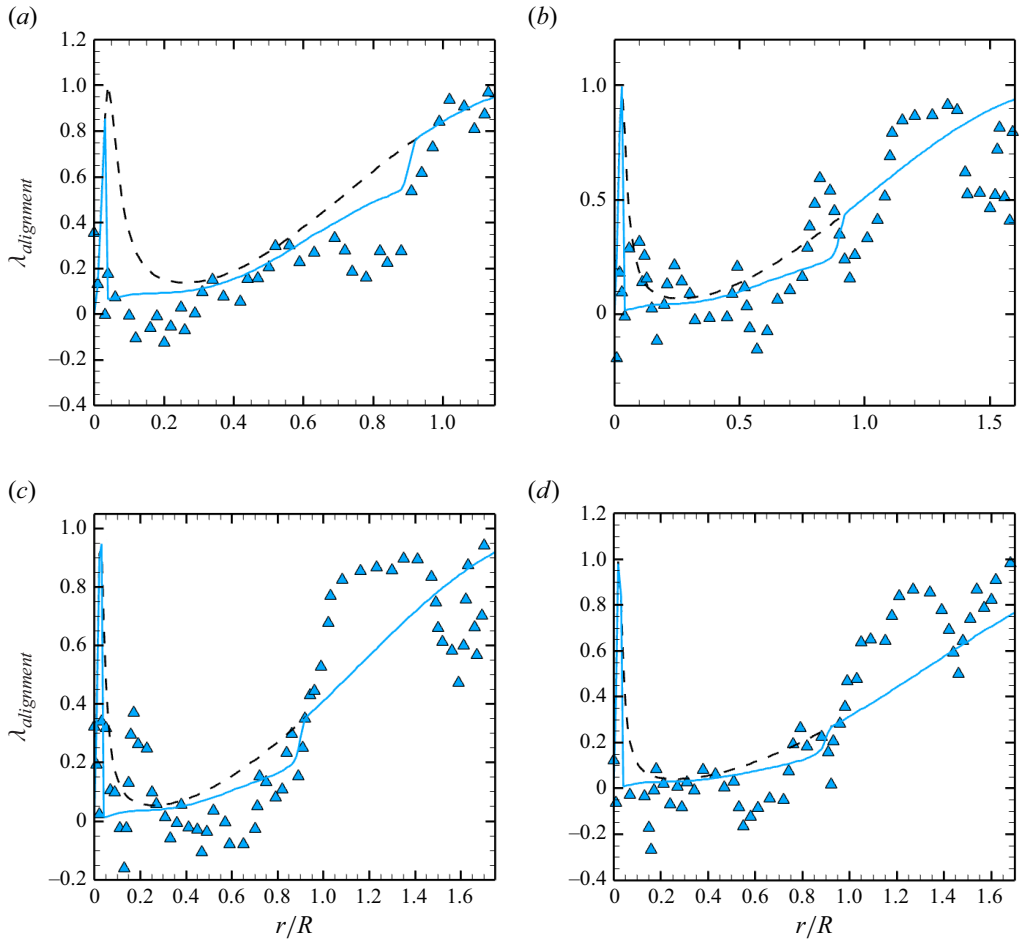


Figure 23. The distribution of the azimuthally averaged alignment of the scalar gradient $\lambda_{alignment}$ on the radial axis in VD SBI. The moments captured from (*a*) to (*d*) are the same as those of figure 18. The azimuthally averaged alignment is plotted as the blue dots, while the prediction of the single-vortex theory in (3.24) is plotted as the black dashed line and the prediction for $\lambda_{alignment}$ in (5.21) is plotted as blue solid line.

Similar to the approach used in the derivation of the PS mixing model described in § 4, assumption PS.(iv) can also be applied to assume the mixing in VD SBI occurs within a compressed semicircle depicted in figure 16. Consequently, (5.23) is transformed into the coordinate system (O, X, Y) that aligns with the deforming scalar strips

$$\frac{\partial Y}{\partial t} + U\frac{\partial Y}{\partial x} = -\mathcal{D}\,(1-\sigma)\,\frac{\partial Y}{\partial x}\frac{\partial Y}{\partial x} + \mathcal{D}\frac{\partial^2 Y}{\partial x^2}, \tag{5.24}$$

where the relatively small component of the scalar gradient $\partial Y/\partial y$ is neglected. Employing the same expression for the relative velocity (U, V) as in (4.5) and utilising the Ranz transformation described in (4.7) as applied in PS SBI, this equation is further simplified into a quasi-Fourier equation

$$\frac{\partial Y}{\partial \tau^{\mathcal{D}}} = -\,(1-\sigma)\,\frac{\partial Y}{\partial \varsigma}\frac{\partial Y}{\partial \varsigma} + \frac{\partial^2 Y}{\partial \varsigma^2}, \tag{5.25}$$

https://doi.org/10.1017/jfm.2025.11051 Published online by Cambridge University Press

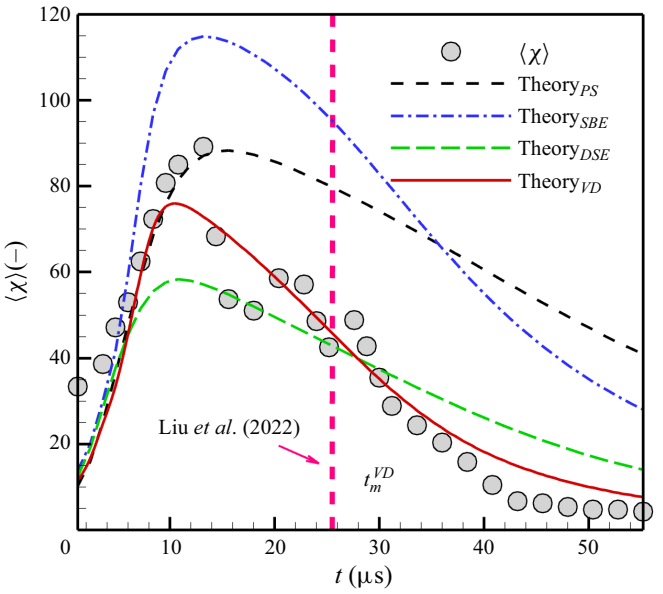


Figure 24. The comparison between the evolution of the total SDR $\langle\chi\rangle$ in VD SBI and the predictions of the mixing models. The prediction of PS mixing model as detailed in (4.11) is plotted as black dotted line, the prediction of VD mixing model as detailed in (5.33) is plotted as red solid line, the prediction of mixing model incorporating only the SBE on the stretching dynamics (5.22) is plotted as blue dash dot line and the prediction of mixing model incorporating only the density source effect (DSE) on the diffusion process (5.22) is plotted as green long dash line. The pink line indicates the VD mixing time t_m^{VD} obtained from the previous research (Liu *et al.* 2022).

the transformed time $\tau^{\mathcal{D}}$ in this equation is given by

$$\begin{cases} \tau^{\mathcal{D}} = \displaystyle\int_0^t \frac{\mathcal{D}}{s_0^2}\left(1+\tau^2\right)\mathrm{d}t', \\ \tau = \displaystyle\int_0^t 2s_1(t')\mathrm{d}t', \\ s_1 = s_1^{ps} + s_1^{b,v}. \end{cases} \tag{5.26}$$

The solution to (5.25) is assumed to take the form $g(\tau^{\mathcal{D}})Y^{ps}(\varsigma, \tau^{\mathcal{D}})$, where $Y^{ps}(\varsigma, \tau^{\mathcal{D}})$ denotes the solution to the Fourier equation without the density source term, thus exhibiting the same expression with PS mixing as described in (4.10). The term $g(\tau^{\mathcal{D}})$ corresponds to the modified function arising from the inclusion of the density source term. Substituting $g(\tau^{\mathcal{D}})Y^{ps}(\varsigma, \tau^{\mathcal{D}})$ into (5.25), the governing equation for the modified function $g(\tau^{\mathcal{D}})$ is derived as

$$\frac{1}{g(\tau^{\mathcal{D}})^2}\frac{\partial g(\tau^{\mathcal{D}})}{\partial \tau^{\mathcal{D}}} = -(1-\sigma)\frac{1}{Y^{ps}}\frac{\partial Y^{ps}}{\partial \varsigma}\frac{\partial Y^{ps}}{\partial \varsigma}. \tag{5.27}$$

In this equation, $(\partial Y^{ps}/\partial\varsigma)(\partial Y^{ps}/\partial\varsigma)$ can be approximated by its averaged value across scalar strips, using an approach analogous to the averaged SDR in (5.15)

$$\left.\frac{\partial Y^{ps}}{\partial \varsigma}\frac{\partial Y^{ps}}{\partial \varsigma}\right|_{\mathrm{avg}} = \begin{cases} \displaystyle\int_{-\infty}^{+\infty}\left(\frac{\partial Y^{ps}}{\partial \varsigma}\right)^2 \mathrm{d}\varsigma, & \text{if } \tau^{\mathcal{D}} < \frac{1}{16}, \\ \displaystyle\int_{-\infty}^{+\infty}\left(\frac{\partial Y^{ps}}{\partial \varsigma}\right)^2 \mathrm{d}\varsigma \Big/ \left(4\sqrt{\tau^{\mathcal{D}}}\right), & \text{if } \tau^{\mathcal{D}} \geqslant \frac{1}{16}. \end{cases} \tag{5.28}$$

https://doi.org/10.1017/jfm.2025.11051 Published online by Cambridge University Press

Simultaneously, Y^{ps} is approximated as half of the maximum value on the scalar strips

$$Y^{ps}\big|_{avg} = \frac{1}{2}\mathrm{erf}\left(\frac{1}{4\sqrt{\tau^{\mathcal{D}}}}\right) = \begin{cases} \dfrac{1}{2}, & \text{if } \tau^{\mathcal{D}} < \dfrac{1}{16}, \\ \dfrac{1}{8\sqrt{\tau^{\mathcal{D}}}}, & \text{if } \tau^{\mathcal{D}} \geqslant \dfrac{1}{16}. \end{cases} \tag{5.29}$$

Using these approximations, the right-hand side of (5.27) is simplified

$$\frac{1}{Y^{ps}}\frac{\partial Y^{ps}}{\partial \varsigma}\frac{\partial Y^{ps}}{\partial \varsigma}\bigg|_{avg} = \begin{cases} \sqrt{\dfrac{2}{\pi}}\tau^{\mathcal{D}\frac{1}{2}}, & \text{if } \tau^{\mathcal{D}} < \dfrac{1}{8}, \\ \dfrac{1}{4\sqrt{2\pi}}\tau^{\mathcal{D}-\frac{3}{2}}, & \text{if } \tau^{\mathcal{D}} \geqslant \dfrac{1}{8}. \end{cases} \tag{5.30}$$

This simplification is validated to be reasonable in the supplementary material. Substituting this result into (5.27), we obtain the expression for the modified function $g(\tau^{\mathcal{D}})$

$$g(\tau^{\mathcal{D}}) = \begin{cases} \dfrac{1}{1+2\sqrt{\frac{2}{\pi}}\,(1-\sigma)\,\tau^{\mathcal{D}\frac{1}{2}}}, & \text{if } \tau^{\mathcal{D}} < \dfrac{1}{8}, \\ \dfrac{1}{1+2\,(1-\sigma)\left(\frac{1}{\sqrt{\pi}} - \frac{\tau^{\mathcal{D}-\frac{1}{2}}}{4\sqrt{2\pi}}\right)}, & \text{if } \tau^{\mathcal{D}} \geqslant \dfrac{1}{8}. \end{cases} \tag{5.31}$$

The mass fraction Y on scalar strips in VD SBI evolves as follows:

$$\begin{cases} Y = g(\tau^{\mathcal{D}})Y^{ps}, \\ Y^{ps} = \dfrac{1}{2}\left[\mathrm{erf}\left(\dfrac{\varsigma+1/2}{2\sqrt{\tau^{\mathcal{D}}}}\right) - \mathrm{erf}\left(\dfrac{\varsigma-1/2}{2\sqrt{\tau^{\mathcal{D}}}}\right)\right]. \end{cases} \tag{5.32}$$

Based on this mass fraction distribution, the VD mixing model for the total SDR $\langle\chi\rangle$ can be proposed as

$$\langle\chi\rangle = \int_0^{\sqrt{2\eta}R} g(\tau^{\mathcal{D}})^2 \frac{1+\tau^2}{s_0}\frac{1}{\sqrt{2\pi\tau^{\mathcal{D}}}}\left(1-\mathrm{e}^{-\frac{1}{8\tau^{\mathcal{D}}}}\right)\mathrm{d}r, \tag{5.33}$$

where

$$\begin{cases} s_1 = s_1^{ps} + s_1^{b,v}, \\ \tau = \displaystyle\int_0^t 2s_1\mathrm{d}t', \\ \tau^{\mathcal{D}} = \displaystyle\int_0^t \frac{\mathcal{D}\mathrm{d}t'}{s(t)^2} = \int_0^t \frac{\mathcal{D}(1+\tau^2)\mathrm{d}t'}{s_0^2}. \end{cases} \tag{5.34}$$

A comparison of the mathematical form of the VD mixing model with the PS mixing model presented in (4.11) reveals that the VD mixing model synthesises two key VD effects on mixing. First, the baroclinic effect on stretching dynamics is reflected in the inclusion of the additional principal strain: $s_1^{b,v}$, which modifies the transformed time τ and $\tau^{\mathcal{D}}$, as defined in (5.26). Second, the influence of the density source on the diffusion process is accounted for by the introduction of the modified function $g(\tau^{\mathcal{D}})$. Similar to the SBE model (5.22), which considers only the SBE on VD mixing, the DSE model is

https://doi.org/10.1017/jfm.2025.11051 Published online by Cambridge University Press

proposed, where only the modified function $g(\tau^{\mathcal{D}})$ representing the DSE is included. The DSE model has the same form as (5.33), but with the secondary baroclinic strain absent: $s_1 = s_1^{ps}$. As with the SBE model (5.22), the absence of the secondary baroclinic strain $s_1^{b,v}$ in the DSE model also leads to an inaccurate prediction of the SDR evolution in VD SBI, as discussed in figure 24.

Figure 24 compares the evolution of the total SDR $\langle\chi\rangle$ with theoretical predictions from the PS mixing model (4.11), the mixing model incorporating only the SBE on the stretching dynamics (5.22), the mixing model incorporating only the DSE on diffusion process and the VD mixing model (5.33). It is evident that the PS mixing model overestimates the total SDR $\langle\chi\rangle$. In comparison, the inclusion of the additional principal strain rate $s_1^{b,v}$ in (5.22) enhances the growth of $\langle\chi\rangle$ during the early stage and accelerates its decay in the later stage. However, the prediction of (5.22) still overestimates the observed evolution of $\langle\chi\rangle$ due to the absence of the modified function $g(\tau^{\mathcal{D}})$. The DSE model predicts the approximate value of total SDR $\langle\chi\rangle$ by including the modified function $g(\tau^{\mathcal{D}})$. However, in the absence of SBE, this model significantly underestimates the principal strain s_1, which leads to a slower growth rate of $\langle\chi\rangle$ in the early stage and a smaller decay rate in the later stage. In contrast, the close agreement between the observed evolution of $\langle\chi\rangle$ and the predictions of the VD mixing model demonstrates that this model, which incorporates both SBE on stretching and DSE on diffusion, accurately captures the underlying mechanisms governing $\langle\chi\rangle$ in VD mixing. Therefore, compared with previous research on the VD mixing time t_m^{VD} (Liu *et al.* 2022), the VD mixing model establishes a quantitative relationship between stretching dynamics and the evolution of the mixing rate in VD SBI.

6. Model validation and scaling behaviour of the SBI mixing rate

In § 5, the VD mixing model for the evolution of SDR detailed in (5.33) is developed based on the characterisation of the stretching dynamics and the mixing process in VD SBI. Since SDR quantifies the mixing rate, this section demonstrates that the increase of mixedness, a measure of the extent of mixing, can also be theoretically predicted using this VD mixing model. The validity of the VD mixing model is further established by its successful application in predicting the evolution of both SDR and mixedness in VD SBI across a broad range of Mach numbers. Additionally, this section presents a scaling analysis of the VD mixing model, which derives the dependence of the time-averaged mixing rate on the dimensionless Péclet number.

6.1. *The VD mixing within a wide range of Mach number*

In figure 6, the initial decrease in the total mixedness $\langle f\rangle$ is attributed to the effect of shock compression, while the monotonic increase in $\langle f\rangle$ is primarily driven by the SDR source term $\langle T_{SDR}^f\rangle$. Consequently, the increase in $\langle f\rangle$ can be theoretically predicted using the time integral of the VD mixing model described in (5.33).

This section focuses on the increase in $\langle f\rangle$, where the effect of shock compression is ignored by redefining the increase in total mixedness through the removal of the velocity-divergence term $\langle T_{divU}^f\rangle$, expressed as

$$\Delta\left\langle f^*\right\rangle = \Delta\left\langle f\right\rangle - \left\langle T_{divU}^f\right\rangle = \left\langle T_{SDR}^f\right\rangle + \left\langle T_{den}^f\right\rangle, \tag{6.1}$$

where the increase in total mixedness $\Delta\langle f^*\rangle$ is decomposed into the SDR source term $\langle T_{SDR}^f\rangle$ and density source term $\langle T_{den}^f\rangle$.

https://doi.org/10.1017/jfm.2025.11051 Published online by Cambridge University Press

According to the definition of these two terms in (3.5), the SDR source term driving the evolution of $\Delta\langle f^*\rangle$ can be modelled based on the VD mixing model for SDR as

$$\left\langle T^f_{SDR}\right\rangle = 8\mathcal{D}\int_0^t\left(\int_0^{\sqrt{2\eta}R} g(\tau^{\mathcal{D}})^2\frac{1+\tau^2}{s_0}\frac{1}{\sqrt{2\pi\tau^{\mathcal{D}}}}\left(1-\mathrm{e}^{-\frac{1}{8\tau^{\mathcal{D}}}}\right)\mathrm{d}r\right)\mathrm{d}t'. \tag{6.2}$$

For the density source term, the relationship between the density gradient $\boldsymbol{\nabla}\rho$ and the scalar gradient $\boldsymbol{\nabla}Y$ (5.11) allows its transformation into the following form:

$$\begin{aligned}\left\langle T^f_{den}\right\rangle &= \int_0^t\left\langle 4\,(1-2Y)\,\frac{\mathcal{D}}{\rho}\frac{\partial\rho}{\partial x_j}\frac{\partial Y}{\partial x_j}\right\rangle\mathrm{d}t'\\ &= \int_0^t\langle -4\mathcal{D}\,(1-2Y)\,(1-\sigma)\,\chi\rangle\,\mathrm{d}t',\end{aligned} \tag{6.3}$$

indicating that the density source term is the product of the mass fraction and SDR. Using the expressions for mass fraction and SDR on scalar strips, the density source term is further modelled as

$$\begin{cases}\left\langle T^f_{den}\right\rangle = \displaystyle\int_0^t\left(\int_0^{\sqrt{2\eta}R} -4\mathcal{D}\,(1-2Y)\,(1-\sigma)\,\chi\,\mathrm{d}r\right)\mathrm{d}t',\\ \chi = g(\tau^{\mathcal{D}})^2\dfrac{1+\tau^2}{s_0}\dfrac{1}{\sqrt{2\pi\tau^{\mathcal{D}}}}\left(1-\mathrm{e}^{-\frac{1}{8\tau^{\mathcal{D}}}}\right),\\ Y\approx\dfrac{1}{2}Y|_{max} = \dfrac{1}{2}g(\tau^{\mathcal{D}})\,\mathrm{erf}\left(\dfrac{1}{4\sqrt{\tau^{\mathcal{D}}}}\right).\end{cases} \tag{6.4}$$

Based on the modelled expressions for the SDR source term $\langle T^f_{SDR}\rangle$ (6.2) and density source term $\langle T^f_{SDR}\rangle$ (6.4), the overall description of the increase in total mixedness $\Delta\langle f^*\rangle$ can be obtained as presented in (6.1). Figure 25 illustrates the small discrepancy between the observed evolution of the increase in total mixedness $\Delta\langle f^*\rangle$ in VD SBI and the theoretical prediction.

The predictive capability of the VD mixing model for both the SDR and the growth of mixedness is also validated in VD SBI across a Mach number range of 1.22∼4.0, with the case set-up detailed in Appendix A. Referring to the structure of the VD mixing model ((5.33)) and the associated expressions for the stretching dynamics ((5.20) and (5.21)) and diffusion process ((5.26) and (5.31)), the undetermined parameters of the VD mixing model include the total circulation Γ_t, the compression rate η, the initial time t_0 for the principal strain rate arising from the primary vortex s_1^{ps}, the emergence time for the SBE t_{sbv} and the post-shock density ratio σ. For VD SBI cases spanning a Mach number range of 1.22 $\sim$ 4.0, these parameters (Γ_t, η, t_0, t_{sbv}, σ) are summarised in the following table 2.

Using these parameters, the predictions of the VD mixing model for the total SDR $\langle\chi\rangle$ and the increase in mixedness $\Delta\langle f^*\rangle$ across the Mach number range are presented in figure 26. As reflected in this figure, the capacity of the VD mixing model is validated to accurate capture the evolution of the mixing rate and mixedness in VD SBI across a wide range of Mach numbers.

Using the VD mixing model, the behaviour of the theoretical predictions for the total SDR $\langle\chi\rangle$ and the increase of total mixedness $\Delta\langle f^*\rangle$ with respect to Mach number can be analysed. For the undetermined parameters (Γ_t, η, t_0, t_{sbv}, σ), the total circulation Γ_t is

https://doi.org/10.1017/jfm.2025.11051 Published online by Cambridge University Press

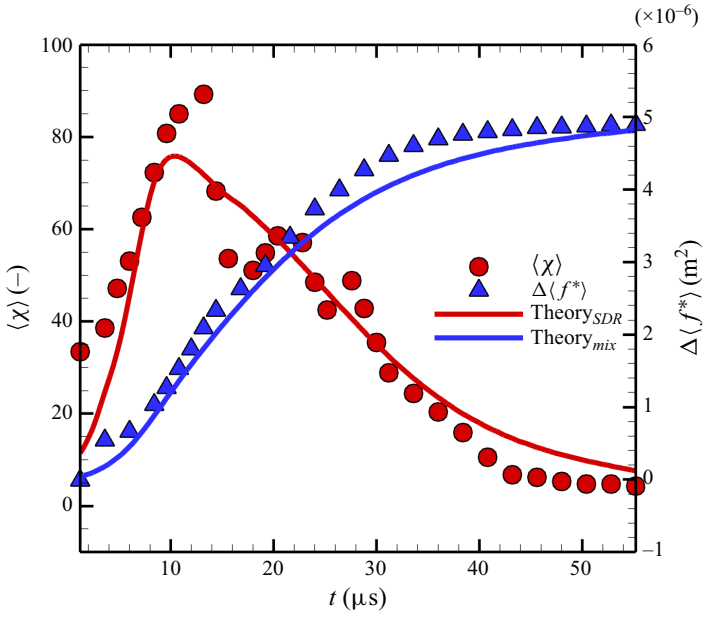


Figure 25. The comparison between the evolution of the total SDR $\langle\chi\rangle$ and increase of the total mixedness $\Delta\langle f^*\rangle$ in VD SBI and the predictions of the mixing models. The prediction of VD mixing model for total SDR $\langle\chi\rangle$ as detailed in (5.33) is plotted as red solid line, while the prediction of VD mixing model for the increase in the total mixedness $\Delta\langle f^*\rangle$ as detailed in (6.1) is plotted as blue solid line.

Ma	Γ_t (m^2 s^{-1})	η	$\sqrt{4\nu t_0}/\sqrt{\eta}R$	$t_{sbv}u_1'/R$	σ
1.22	0.74	0.81	0.58	1.64	0.118
1.8	1.57	0.53	0.59	1.54	0.092
2.4	2.09	0.39	0.43	1.63	0.083
3.0	2.58	0.31	0.48	1.47	0.080
4.0	3.31	0.26	0.49	1.46	0.080

Table 2. Parameters for the VD mixing model applied for the VD SBI across a Mach number range of 1.22 $\sim$ 4.0, including the total circulation Γ_t, the compression rate η, the initial time t_0 for the principal strain rate arising from the primary vortex s_1^{ps}, the emergence time for t_{sbv} and the post-shock density ratio σ.

calculated by Yang's circulation model (Yang *et al.* 1994)

$$\Gamma_t \approx \Gamma_{YKZ} = \frac{4R}{W_i}\frac{p_1' - p_1}{\rho_1'}|At^+|. \tag{6.5}$$

The compression rate η is expressed as a function of Mach number (Yu *et al.* 2021)

$$\eta \approx \frac{\rho_1}{\rho_1'} = \frac{(\gamma-1)\,Ma^2+2}{(\gamma+1)\,Ma^2}. \tag{6.6}$$

The initial time t_0 for s_1^{ps}, the emergence time t_{sbv} and the post-shock density ratio σ are estimated according to table 2 as follows:

$$\frac{\sqrt{4\nu t_0}}{\sqrt{\eta}R} \approx 0.5, \quad \frac{t_{sbv}u_1'}{R} \approx 1.5, \quad \sigma \approx 0.09. \tag{6.7}$$

https://doi.org/10.1017/jfm.2025.11051 Published online by Cambridge University Press

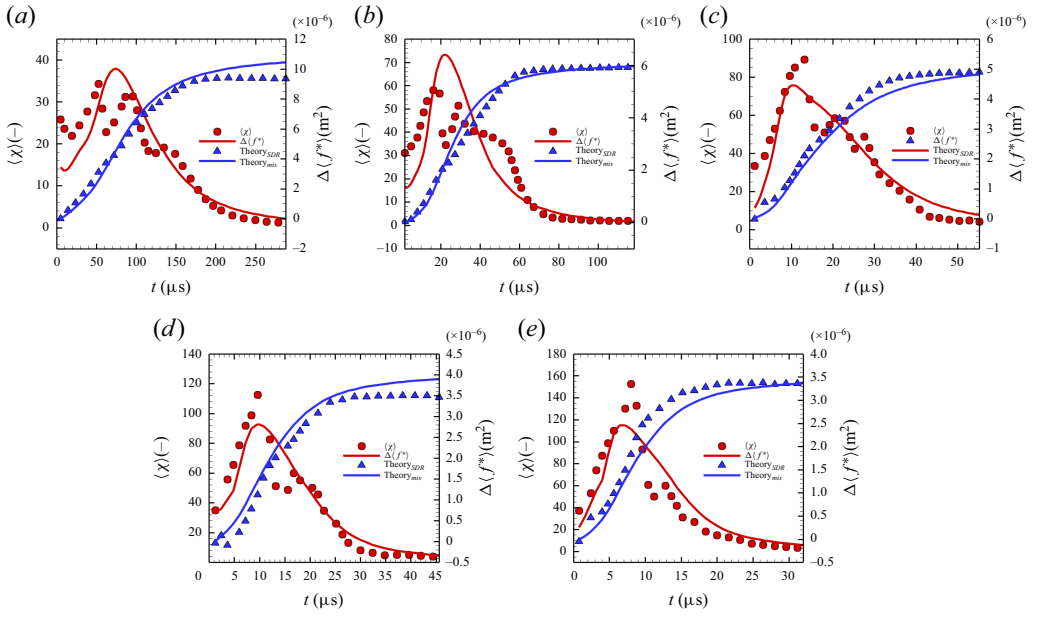


Figure 26. The comparison between the evolution of the total SDR $\langle\chi\rangle$ and increase of the total mixedness $\Delta\langle f^*\rangle$ in VD SBI across a Mach number range of 1.22∼4.0 and the predictions of the mixing models, including (*a*) $Ma = 1.22$, (*b*) $Ma = 1.8$, (*c*) $Ma = 2.4$, (*d*) $Ma = 3.0$ and (*e*) $Ma = 4.0$.

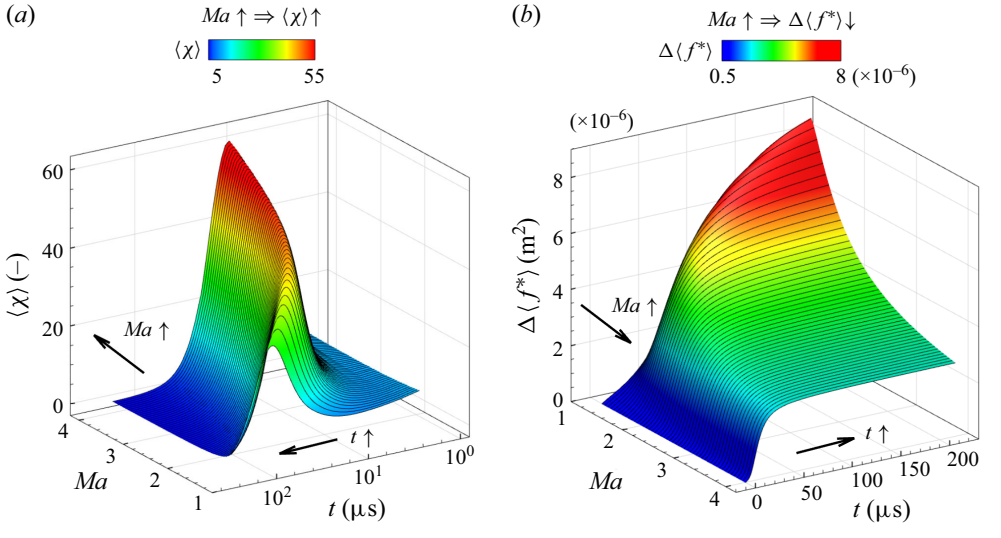


Figure 27. The predictions by VD mixing model (5.33) for (*a*) the total SDR $\langle\chi\rangle$ and increase of total mixedness $\Delta\langle f^*\rangle$ within VD SBI for different Mach numbers.

Once these parameters are determined, the VD mixing model can predict the total SDR $\langle\chi\rangle$ and the increase of total mixedness $\Delta\langle f^*\rangle$, for VD SBI cases across different Mach numbers. These predictions are illustrated in figure 27.

As shown in figure 27, the variation of total SDR and total mixedness with Mach number is evident. As the Mach number increases, the total SDR $\langle\chi\rangle$ increases due to the growth of total circulation Γ_t as predicted by (6.5). However, even with the larger total SDR $\langle\chi\rangle$,

https://doi.org/10.1017/jfm.2025.11051 Published online by Cambridge University Press

the mixing process in SBI cases with higher Mach numbers is completed in a shorter time, leading to a decrease in total mixedness $\Delta\langle f^*\rangle$ with increasing Mach number. These tendencies can be summarised as follows:

$$\begin{cases} Ma\uparrow \Rightarrow \langle\chi\rangle\uparrow, \\ Ma\uparrow \Rightarrow \Delta\left\langle f^*\right\rangle\downarrow, \end{cases} \tag{6.8}$$

which are consistent with the theoretical predictions shown in figure 26. The inherent scaling behaviour of these two mixing indicators will be further examined in the subsequent discussion.

6.2. *Scaling analysis of the mixing rate on Pe*

Based on the VD mixing model applicable to VD SBI across a Mach number range, this section examines the scaling behaviour of the time-averaged mixing rate. As described in § 4, the mixing process in VD SBI can be divided into two distinct stages: the growth stage and the decay stage, separated by the characteristic time $t_{charac} = (3/32)(s_0^2/s_1^2\mathcal{D})^{1/3}$. Without loss of generality, the time interval $0 < t \leqslant t_{charac}$ is defined as the growth stage, while $t_{charac} < t \leqslant 2t_{charac}$ is defined as the decay stage. The time-averaged mixing rate during the mixing process is defined as

$$\overline{\langle\chi\rangle} = \frac{\Delta\left\langle f^*\right\rangle|_0^{2t_{charac}}}{2\mathcal{D}t_{charac}}. \tag{6.9}$$

During the growth stage ($0 < t \leqslant t_{charac}$), to simplify the structure of the VD mixing model (5.33), the principal strain rate induced by the SBE $s_1^{b,\nu}$ is neglected. Under this assumption, (5.33) reduces to

$$\langle\chi\rangle \approx \int_0^{\sqrt{2\eta}R} g\left(\tau^{\mathcal{D}}\right)^2\sqrt{\frac{6}{\pi\mathcal{D}}}s_1 t^{\frac{1}{2}}\mathrm{d}r. \tag{6.10}$$

By estimating the parameters in this equation

$$\int_0^{\sqrt{2\eta}R}\mathrm{d}r \sim \sqrt{\eta}R, \quad s_1 \sim \frac{\Gamma_t}{\eta R^2} \tag{6.11}$$

the expression for $\langle\chi\rangle$ can be approximated as

$$\langle\chi\rangle \sim g\left(\tau^{\mathcal{D}}\right)^2\sqrt{\frac{6}{\pi\mathcal{D}}}\frac{\Gamma_t}{\sqrt{\eta}R}t^{\frac{1}{2}}. \tag{6.12}$$

Arisen from the similar post-shock density ratio listed in table 4, the modified function $g(\tau^{\mathcal{D}})$ is assumed to be nearly identical for the VD SBI across the Mach number range of $1.22 \sim 4.0$. This leads to a further simplification of this estimation

$$\langle\chi\rangle \sim \sqrt{\frac{6}{\pi\mathcal{D}}}\frac{\Gamma_t}{\sqrt{\eta}R}t^{\frac{1}{2}}. \tag{6.13}$$

Using this estimation for the total SDR $\langle\chi\rangle$, the increase of total mixedness $\Delta\langle f^*\rangle$ in the growth stage can be approximated

$$\Delta\left\langle f^*\right\rangle \approx \left\langle T_{SDR}^f\right\rangle \sim 8\mathcal{D}\int_0^{t_{charac}}\sqrt{\frac{6}{\pi\mathcal{D}}}\frac{\Gamma_t}{\sqrt{\eta}R}t^{\frac{1}{2}}\mathrm{d}t = \frac{2}{\sqrt{\pi}}\eta R^2. \tag{6.14}$$

https://doi.org/10.1017/jfm.2025.11051 Published online by Cambridge University Press

Similarly, the approximation for the total SDR $\langle\chi\rangle$ in the decay stage ($t_{charac} < t \leqslant 2t_{charac}$) is presented as

$$\langle\chi\rangle \sim \frac{3}{16}\sqrt{\frac{3}{2\pi}}\frac{\eta^{\frac{5}{2}}R^5}{\mathcal{D}^{\frac{3}{2}}\Gamma_t}t^{-\frac{5}{2}}, \tag{6.15}$$

and the increase of total mixedness $\Delta\langle f^*\rangle$ in this stage is given by

$$\Delta\left\langle f^*\right\rangle \approx \left\langle T^f_{SDR}\right\rangle \sim 8\mathcal{D}\int_{t_{charac}}^{2t_{charac}} \frac{3}{16}\sqrt{\frac{3}{2\pi}}\frac{\eta^{\frac{5}{2}}R^5}{\mathcal{D}^{\frac{3}{2}}\Gamma_t}t^{-\frac{5}{2}}\mathrm{d}t = \frac{2}{\sqrt{\pi}}\left(2-\frac{1}{2\sqrt{2}}\right)\eta R^2. \tag{6.16}$$

Therefore, the growth of the total mixedness throughout the whole mixing process is only in proportion to the compression rate

$$\Delta\left\langle f^*\right\rangle \approx \left\langle T^f_{SDR}\right\rangle = 8\mathcal{D}\int_0^{2t_{charac}} \langle\chi\rangle\,\mathrm{d}t = \frac{2}{\sqrt{\pi}}\left(3-\frac{1}{2\sqrt{2}}\right)\eta R^2 \sim \eta R^2. \tag{6.17}$$

This finding is consist with the conclusion derived from alternative approaches in previous studies (Li *et al.* 2020; Yu *et al.* 2021). Moreover, for the time period associated with the mixing process $2t_{charac} = ((3/16)(s_0^2/(s_1^2\mathcal{D})))^{(1/3)}$, using the estimation for the width of scalar strips and the principal strain

$$s_0 \sim \sqrt{\eta}R, \quad s_1 \sim \frac{\Gamma_t}{\eta R^2}, \tag{6.18}$$

this time period can be approximated as

$$2t_{charac} = \left(\frac{3}{16}\frac{s_0^2}{s_1^2\mathcal{D}}\right)^{\frac{1}{3}} \sim (s_0)^{\frac{2}{3}}(s_1)^{-\frac{2}{3}}\mathcal{D}^{-\frac{1}{3}} \sim \eta R^2\Gamma_t{}^{-\frac{2}{3}}\mathcal{D}^{-\frac{1}{3}}, \tag{6.19}$$

which is similar to the estimation for the mixing time reported in related studies (Jacobs 1992; Tomkins *et al.* 2008; Liu *et al.* 2022), verifying the reliability of this approximation for the time period.

Thus, the scaling of increase of the mixedness and time period during the mixing process can be summarised as follows:

$$\begin{cases} \Delta\left\langle f^*\right\rangle \sim \eta R^2, \\ 2t_{charac} \sim \eta R^2\Gamma_t{}^{-\frac{2}{3}}\mathcal{D}^{-\frac{1}{3}}. \end{cases} \tag{6.20}$$

This leads to the scaling behaviour of the time-averaged mixing rate

$$\overline{\langle\chi\rangle} = \frac{\Delta\langle f^*\rangle}{2\mathcal{D}t_{charac}} \sim \left(\frac{\Gamma_t}{\mathcal{D}}\right)^{\frac{2}{3}}, \quad \text{i.e.} \quad \overline{\langle\chi\rangle} \sim Pe^{\frac{2}{3}}, \tag{6.21}$$

where $Pe = \Gamma_t/\mathcal{D}$ is the dimensionless Péclet number (Meunier & Villermaux 2003). This dimensionless number quantifies the relative strength of the stretching dynamics compared with the diffusion process.

As presented in figures 28 and 29, the scaling suggested by (6.20) and (6.21) provides good collapses for the evolution of the normalised increase of the mixedness and the normalised total SDR over time. The scaling behaviour of the time-averaged mixing rate (6.21) is further validated through figure 30 and table 3. In figure 30, the least-squares fit curve for cases with varying Mach numbers is $\overline{\langle\chi\rangle} \sim Pe^{0.7368}$. This curve closely aligns with the theoretically derived scaling law $\overline{\langle\chi\rangle} \sim Pe^{2/3}$, with small discrepancies likely

https://doi.org/10.1017/jfm.2025.11051 Published online by Cambridge University Press

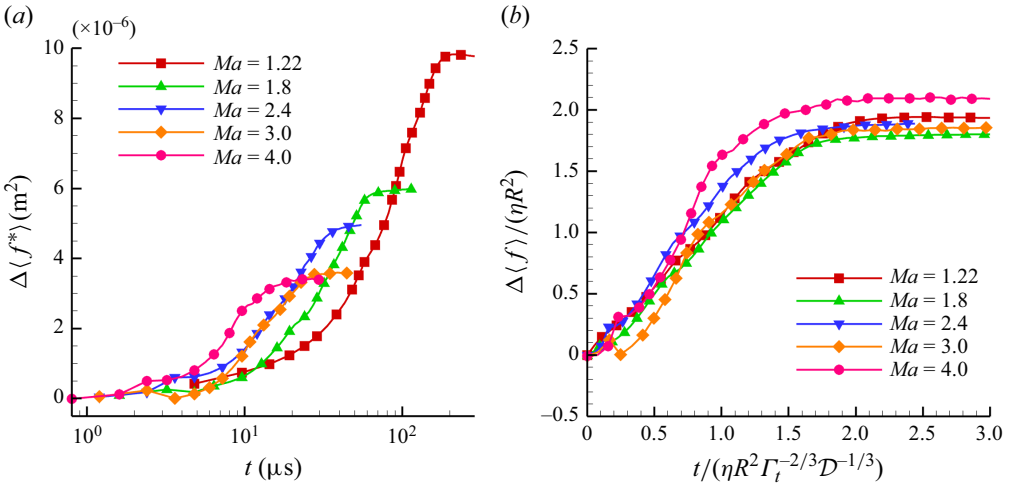


Figure 28. The evolution of (*a*) the increase of total mixedness $\Delta\langle f^*\rangle$ versus time t; (*b*) the normalised increase of total mixedness $\Delta\langle f^*\rangle/(\eta R^2)$ normalised by versus the normalised time $t/(\eta R^2 {\Gamma_t}^{-2/3}\mathcal{D}^{-1/3})$ in the VD SBI cases with different Mach numbers.

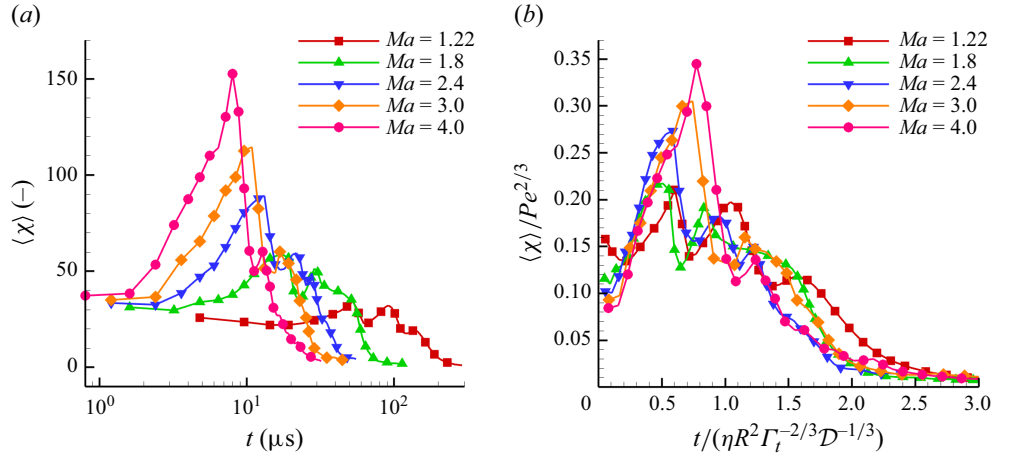


Figure 29. The evolution of (*a*) the total SDR $\langle\chi\rangle$ versus time t; (*b*) the normalised total SDR $\Delta\langle f^*\rangle/Pe^{2/3}$ versus the normalised time $t/(\eta R^2 {\Gamma_t}^{-2/3}\mathcal{D}^{-1/3})$ in the VD SBI cases with different Mach numbers.

arising from oversimplifications made during our derivation. Nevertheless, due to the minimal difference between the least-squares fit curve and the theoretical scaling law, as well as the nearly identical normalised time-averaged total SDR in table 3, (6.21) provides a reasonable description of the dependence of the time-averaged total SDR on the Péclet number. Since the SDR quantifies the mixing rate, and the Péclet number measures the relative strength of the stretching dynamics compared with diffusion, this dependence $\overline{\langle\chi\rangle} \sim Pe^{2/3}$ highlights the critical role of the stretching dynamics in governing the mixing rate within this canonical VD SBI mixing process.

https://doi.org/10.1017/jfm.2025.11051 Published online by Cambridge University Press

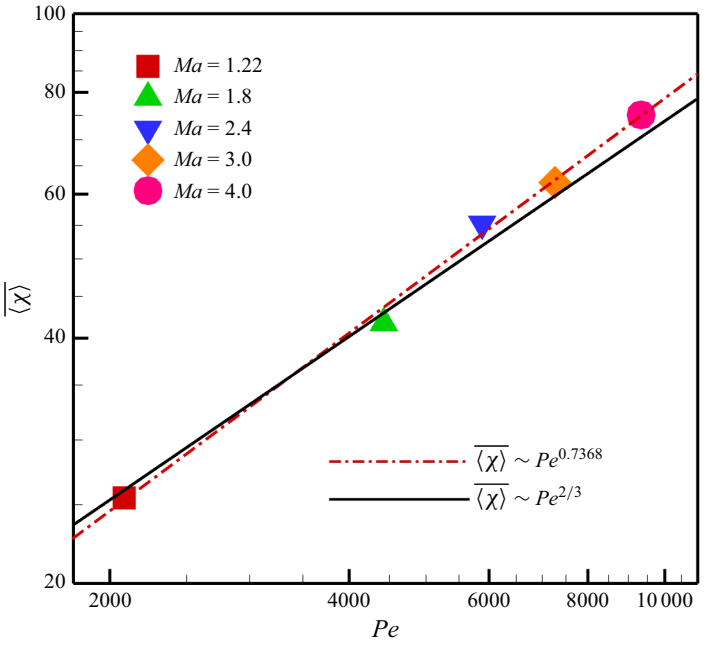


Figure 30. The scaling of the time-averaged mixing rate, i.e. total SDR $\overline{\langle\chi\rangle}$ on the dimensionless Péclet number Pe.

Ma	Pe	$\overline{\langle\chi\rangle}$	$\overline{\langle\chi\rangle}/Pe^{2/3}$
1.22	2084.5	25.49	0.156
1.8	4422.5	41.69	0.155
2.4	5887.3	55.21	0.169
3.0	7267.6	62.07	0.166
4.0	9323.9	75.15	0.170

Table 3. Parameters for validating the scaling law of time-averaged total SDR $\overline{\langle\chi\rangle}$, including Péclet number Pe, time-averaged total SDR $\overline{\langle\chi\rangle}$ and the normalised time-averaged total SDR $\overline{\langle\chi\rangle}/Pe^{2/3}$.

7. Conclusions and future work

This paper begins with the central question in VD mixing research: What is the role of the stretching dynamics in VD mixing within the context of canonical RM-type SBI? Comparing with our previous investigation on the mixing time to predict the time required to reach a steady mixing state, in this study, the relationship between VD mixing and stretching is systematically investigated by a focus on qualitatively characterising the mixing process, as reflected by evolution of the SDR, commonly referred to as the mixing rate, and its time integral, denote as mixedness over time. Employing high-resolution simulations, we examined the interaction of a cylindrical helium bubble with a wide range of shock Mach numbers, spanning from 1.22 to 4.

From the starting point, by analysing the decomposition of the total SDR $\langle\chi\rangle$, we identified the stretching term $\langle T^{\chi}_{stretch}\rangle$ as the primary driver of SDR growth, while the strictly negative diffusion term $\langle T^{\chi}_{diff}\rangle$ predominantly contributes to the reduction of SDR. This observation reveals that mixing primarily originates from the diffusion process

https://doi.org/10.1017/jfm.2025.11051 Published online by Cambridge University Press

and is substantially enhanced by the stretching dynamics, thus preliminarily highlighting the significance of stretching in the mixing process. Furthermore, the stretching rate is defined rigorously originating from the expression of stretching term $\langle T^{\chi}_{stretch}\rangle$: $R_{stretch} = 2s_1\lambda_{alignment}$, which is determined by the principal strain rate s_1 and scalar gradient alignment $\lambda_{alignment}$. By focusing on the governing equations for the principal strain rate s_i (SDGE-s_i) and scalar gradient alignment λ_i (SDGE-λ_i) within the strain-rate eigenframe, we comprehensively established a framework for analysing the stretching dynamics through the integration of SDGE-s_i and SDGE-λ_i. Motivated by the nearly steady single vortex following the shock's interaction with the bubble, the single-vortex stretching dynamics is researched by solving this stretching dynamics framework analytically in a cylindrical coordinate system (r, φ) under the assumptions for PS mixing. The solutions of SDGE-s_i and SDGE-λ_i illustrate the algebraic stretching characteristic, which is further confirmed by the Lagrangian particle movement results.

Before investigating the role of the stretching dynamics on mixing in VD SBI, we initially explore the relatively simple scenario of PS SBI, where density differences are ignored, as the foundation for understanding VD mixing. By setting the origin of the cylindrical coordinate system (r, φ) at the vortex centre, the azimuthal velocity distribution indicates that mixing in PS SBI is predominantly governed by the large-scale main vortex. Further, by comparing the distribution of the azimuthally averaged principal strain rate s_1 and scalar gradient alignment $\lambda_{alignment}$ with single-vortex theoretical solutions, we assert that the stretching dynamics in PS SBI exhibits a single-vortex algebraic stretching characteristic. According to the fact that the evolution of SDR is also influenced by molecular diffusion, the diffusion process is incorporated by solving the advection–diffusion equation on a series of scalar strips based on the analytical expressions of the single-vortex stretching dynamics. Combining the single-vortex stretching expressions and the modelled diffusion process, we propose a PS mixing model for the total SDR $\langle\chi\rangle$, which has good capacity to accurately predict the evolution of $\langle\chi\rangle$ in PS SBI, therefore the mixing in PS SBI is proved to be governed by the single-vortex algebraic stretching rate. The two stage approximations of this model reveal the existence of a characteristic time t_{charac} and identify two distinct mixing stages divided by this characteristic time: the SDR growth stage and the SDR decay stage.

In the context of VD SBI, we identify that the presence of density variations introduces two significant density-gradient effects that challenge the extension of the PS mixing model to VD mixing. The first effect is a SBE observed in the governing equations for the principal strain rate s_1. This effect amplifies the magnitude of s_1, while maintaining the algebraic stretching characteristic observed in single-vortex scenarios. The second effect is the emergence of the density-gradient source term in the VD advection–diffusion equation, which suppresses the diffusion process due to its strictly negative value. We model the SBE as an additional principal strain $s_1^{b,v}$ and the density source effect as a modified function $g(\tau^{\mathcal{D}})$. Based on these modifications, we propose a VD mixing model for the total SDR $\langle\chi\rangle$ on the basis of the PS mixing model. This model is validated to accurately describe the total SDR $\langle\chi\rangle$ and its time integral, specifically the increment of total mixedness $\Delta\langle f^*\rangle$ in VD SBI cases across a wide range of Mach numbers from 1.22 to 4. Consequently, a qualitative relationship between the stretching dynamics and VD mixing is established by this model. To further explain the essential role of the stretching dynamics in VD mixing, we conduct a scaling analysis on the time-averaged mixing rate $\overline{\langle\chi\rangle}$. We derive that the time-averaged mixing rate $\overline{\langle\chi\rangle}$ is directly proportional to $Pe^{2/3}$ as: $\overline{\langle\chi\rangle} \sim Pe^{2/3}$. Here, the dimensionless Péclet number $Pe = \Gamma_t/\mathcal{D}$ serves as a measure of the relative strength of

https://doi.org/10.1017/jfm.2025.11051 Published online by Cambridge University Press

the stretching dynamics compared with the diffusion process, thus highlighting the crucial role of stretching dynamics in mixing through this scaling behaviour.

In conclusion, this paper systematically explores the stretching dynamics and its effects on VD mixing within the context of the typical single-vortex scenario in VD SBI. The established relationship between the stretching dynamics and the evolution of the mixing rate provides a novel perspective on the fundamental mechanism by which the flow governs the mixing process. The proposed VD mixing model serves as a rapid estimation tool for predicting the mixing rate and the extent of mixing in VD SBI. Furthermore, the findings of this study will pave the way for future research on VD mixing in practical engineering applications, such as oblique shock/jet interactions. Recent studies have successfully interpreted RMI phenomena from the perspectives of the vortex dynamics, particularly in the context of fill tube jet mixing during ICF implosions (Kuczek & Haines 2023; Wadas *et al.* 2023) and vortex instabilities (Wadas *et al.* 2024; Yan *et al.* 2025). These investigations confirm that vortex rings are the dominant structures governing RMI-induced flows. In light of these findings, future work will focus on extending the current VD mixing model to capture vortex ring-dominated VD mixing, with the goal of elucidating fill tube jet mixing mechanisms and mixed mass growth in ICF implosion environments.

Supplementary material and movies. Supplementary material and movies are available at https://doi.org/10.1017/jfm.2025.11051.

Funding. Thanks to the Postdoctoral Fellowship Program (Grade C) of China Postdoctoral Science Foundation (Grant Number GZC20231566), Sichuan Science and Technology Program (2025ZNSFSC0834), Natural Science Foundation of Shanghai (Youth Projects 25ZR1402273) and Natural Science Foundation of China (nos. 91941301) for funding and supporting this research.

Declaration of interests. The authors report no conflict of interest.

Appendix A. Initial conditions for VD SBI across a wide range of Mach numbers

This section outlines the case settings for the VD SBI across a range of Mach numbers, spanning from 1.22 to 4. The initial conditions for the VD SBI cases are depicted in figure 1, which are identical to those specified for the $Ma = 2.4$ case in § 2. The primary distinction among the cases with varying shock strengths lies in the post-shock conditions (u_1', ρ_1', P_1', T_1'). According to the Rankine–Hugoniot equation, the post-shock air conditions for the VD SBI cases are summarised in table 4. The simulation results for these SBI cases are also analysed by the total circulation Γ_t and compression rate η.

Figure 31 presents the time evolution of these two parameters across different shock Mach numbers. It is observed that, following the shock interaction with the bubble, both the total circulation Γ_t and the compression rate η approximate constant values, indicating the formation of a nearly steady single vortex. With increasing shock Mach number, the total circulation Γ_t increases, while the compression rate η decreases, consistent with previous research findings (Niederhaus *et al.* 2008).

Appendix B. Grid resolution study

The sensitivity of the mixing indicator SDR to mesh resolution necessitates careful selection of the grid size to ensure the resolution of numerical results. In this study, four mesh resolutions with consistent refinement ratio are evaluated: $\Delta = 5.0 \times 10^{-5}$, $\Delta = 2.5 \times 10^{-5}$, $\Delta = 1.25 \times 10^{-5}$ and $\Delta = 0.625 \times 10^{-5}$ m. The interaction of a $Ma = 2.4$ shock with a helium bubble is selected as the representative case. Qualitative comparisons

https://doi.org/10.1017/jfm.2025.11051 Published online by Cambridge University Press

Ma	p_1' (Pa)	T_1' (K)	u_1' (m s^{-1})	W_t (m s^{-1})	At^+ (−)	$\mathcal{D}$ (m^2 s^{-1})	Γ_t (m^2 s^{-1})	Re (−)	Pe (−)
1.22	159036.9	334.06	114.74	1121.89	−0.789	355×10^{-6}	0.74	5083.3	2084.5
1.8	366015.0	448.28	356.58	1440.00	−0.831	355×10^{-6}	1.57	20975.1	4422.5
2.4	667391.3	596.87	568.31	1678.08	−0.845	355×10^{-6}	2.10	38446.2	5887.3
3.0	1046646.5	783.41	768.11	1958.78	−0.852	355×10^{-6}	2.58	57473.6	7267.6
4.0	1873802.9	1182.91	1074.53	2439.15	−0.852	355×10^{-6}	3.31	95307.9	9323.9

Table 4. Parameters of VD SBI cases within a wide range of Ma number, including the post-shock air pressure p_1', post-shock air temperature T_1', post-shock air velocity u_1', the transmitted shock wave speed W_t, which are calculated from the Rankine–Hugoniot equation. The post-shock Atwood number, which presents the difference between the helium bubble density following the shock action ρ_2' and the post-shock ambient air density ρ_1', is defined as $At^+ = (\rho_2' - \rho_1')/(\rho_2' + \rho_1')$. Here, $\mathcal{D}$ is the constant Fickian diffusivity. The total circulation Γ_t and the Péclet $Pe = \Gamma_t/\mathcal{D}$ are also demonstrated in this table to reflect the strength of stretching for different cases. While the Reynolds number is defined as $Re = \Gamma_t/\nu$, where $\nu = \mu/\overline{\rho'}$ is the kinematic viscosity, $\overline{\rho'} = (\rho_1' + \rho_2')/2$ is the average density of the post-shock bubble and ambient air.

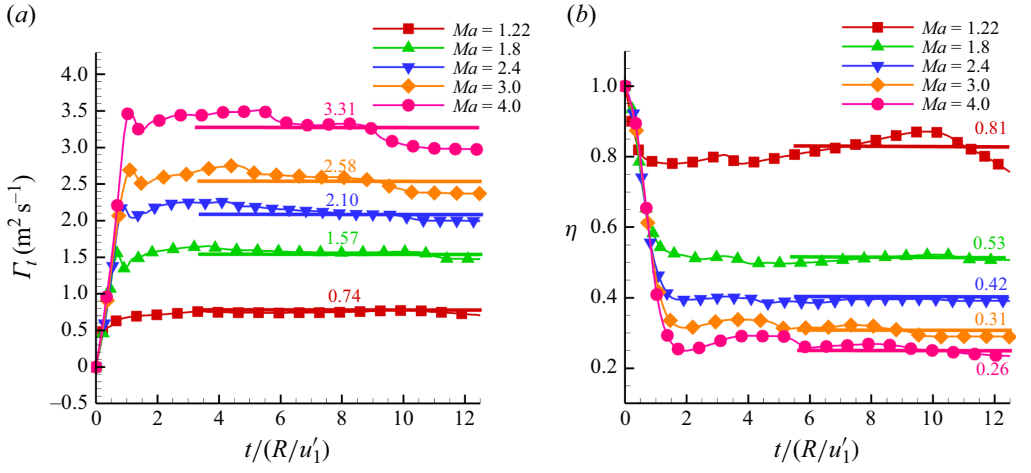


Figure 31. Time evolution of (a) the total circulation Γ_t and (b) the compression rate η for different shock Mach number cases.

among these mesh resolutions are presented in figure 32. By comparing the mass fraction contour of four different resolutions, it is evident that that small-scale flow structures are significantly smeared by numerical viscosity and diffusivity in coarser meshes, specifically for grid sizes $\Delta = 5.0 \times 10^{-5}$ and $\Delta = 2.5 \times 10^{-5}$ m. In contrast, these structures are well captured in finer meshes, with grid sizes $\Delta = 1.25 \times 10^{-5}$ and $\Delta = 0.625 \times 10^{-5}$ m. Additionally, it can also be found that a high degree of consistency exists in flow structures between the two finest resolutions, mesh-3 and mesh-4, indicating sufficient convergence.

Figure 33 presents a comparison of qualitative parameters across different mesh resolutions. Regarding flow characteristics, figures 33(a) and 33(b) demonstrate that both total circulation Γ_t and positive circulation Γ^+ exhibit similar trends for mesh-3 and mesh-4. The mixing characteristics observed in different meshes are evaluated by comparing the total SDR $\langle\chi\rangle$ and total mixedness $\langle f\rangle$ in figures 33(c) and 33(d), respectively. The close alignment in the evolution of these mixing indicators between mesh-3 and mesh-4 confirms the grid independence of the mixing process. Taking into account computational cost and simulation accuracy, we select the mesh resolution of

https://doi.org/10.1017/jfm.2025.11051 Published online by Cambridge University Press

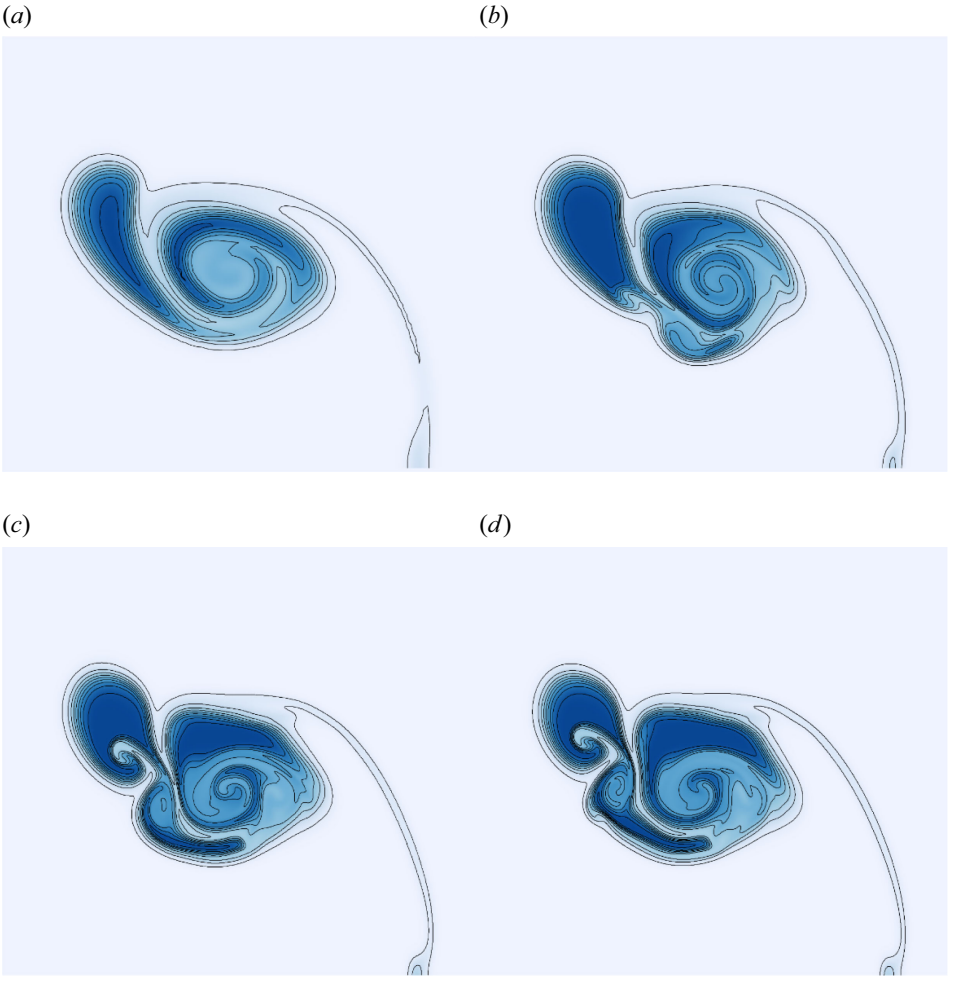


Figure 32. Grid resolution study on the mass fraction contour at $t = 21.6$ µs. (*a*) Mesh-1: $\Delta = 5.0 \times 10^{-5}$ m, (*b*) mesh-2: $\Delta = 2.5 \times 10^{-5}$ m, (*c*) mesh-3: $\Delta = 1.25 \times 10^{-5}$ m, (*d*) mesh-4: $\Delta = 0.625 \times 10^{-5}$ m.

$\Delta = 1.25 \times 10^{-5}$ m for the present study. This resolution appropriately captures the dynamics of flow evolution and the mixing process with quantitative accuracy.

Appendix C. Validation of the SDGE-s_i (3.7) and SDGE-λ_i (3.10)

This section validates the stretching dynamics framework, which consists of the SDGE-s_i ((3.7)) and SDGE-λ_i (3.10), by using Lagrangian methods. A cylindrical bubble interacting with a $Ma = 1.22$ shock wave is selected as the representative case. At the initial time, approximately $n = 80,600$ passive particles are seeded within the bubble, and their trajectories are computed by solving the advection ODE (C1) using a fourth-order Runge–Kutta integrator

$$\frac{\mathrm{d}\boldsymbol{x}}{\mathrm{d}t} = \boldsymbol{u}\,(\boldsymbol{x}, t), \boldsymbol{x} = (x, y), \boldsymbol{u} = (u, v), \tag{C1}$$

where the evolution of the passive particles is illustrated in figure 34.

https://doi.org/10.1017/jfm.2025.11051 Published online by Cambridge University Press

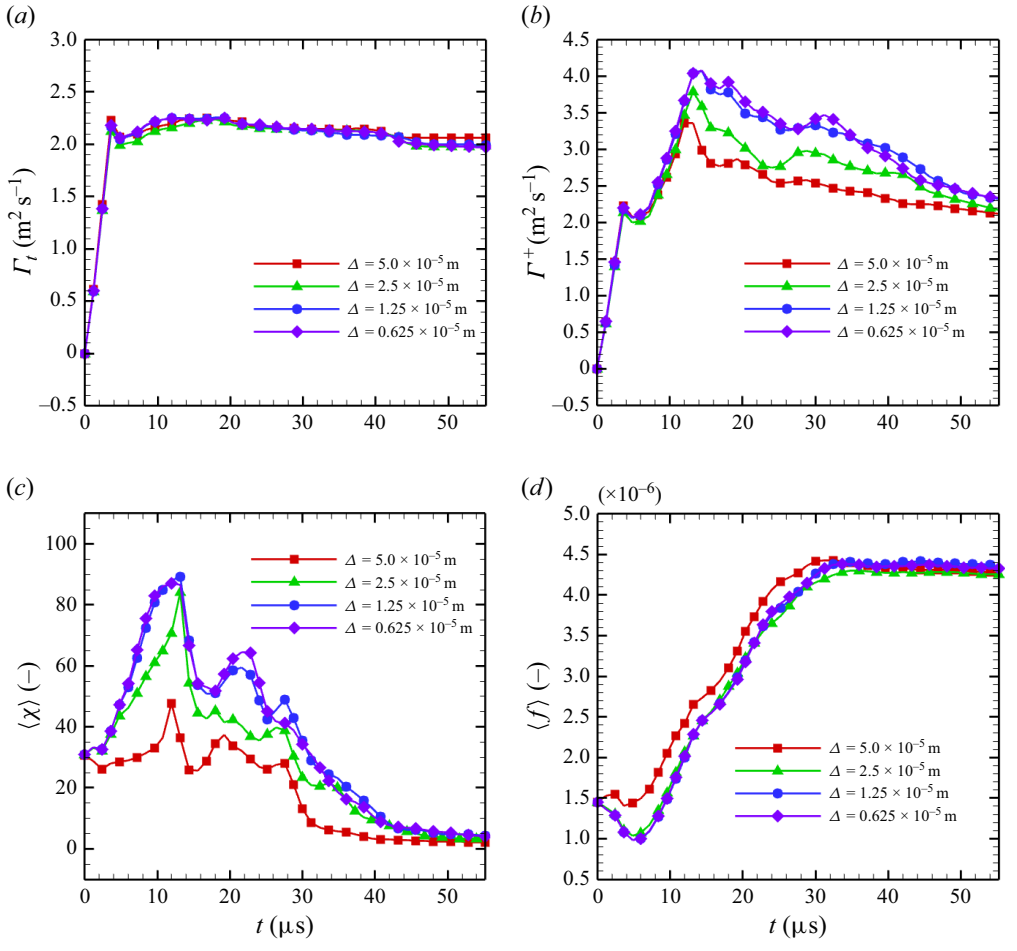


Figure 33. Comparison of qualitative parameters from different mesh resolutions. (*a*) Total circulation Γ_t, (*b*) positive circulation Γ^+, (*c*) total SDR $\langle\chi\rangle$, (*d*) total mixedness $\langle f\rangle$.

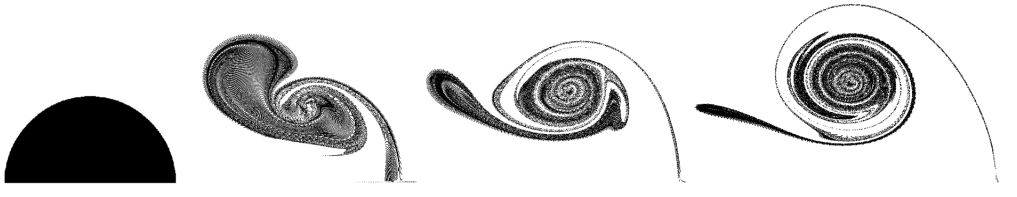


Figure 34. The results of the Lagrangian particle movement at the moment $t = 0$, $t = 47$, $t = 94$ and $t = 141$ μs for the case with a shock strength of $Ma = 1.22$.

For the SDGE-s_i (3.7), we first validate the governing equation for the principal strain rate s_1 in two-dimensional VD SBI

$$\frac{\mathrm{d}s_1}{\mathrm{d}t} = -s_1^2 + \frac{1}{4}\omega^2 + \widetilde{H_{11}^p} + \widetilde{H_{11}^b} + \widetilde{H_{11}^v}, \tag{C2}$$

where $T_{self} = -s_1^2 + (1/4)\omega^2$ represents the self-interaction term. On the left-hand side, the material derivative is computed along the trajectories of the passive particles as

https://doi.org/10.1017/jfm.2025.11051 Published online by Cambridge University Press

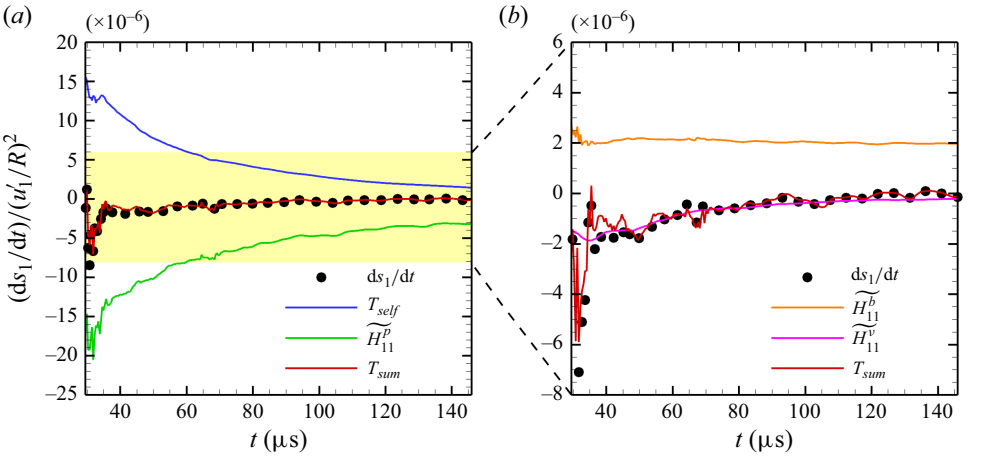


Figure 35. Comparison of the material derivative of the principal strain s_1, obtained from Lagrangian particle movement results, with the terms on the right-hand side of (C2). Panel (*a*) shows the terms with large magnitudes, while (*b*) presents the terms with small magnitudes.

$$\frac{\mathrm{d}s_1}{\mathrm{d}t} = \frac{1}{n}\sum_{i=1}^{n} \frac{s_1(\boldsymbol{x}_i(t+\mathrm{d}t), t+\mathrm{d}t) - s_1(\boldsymbol{x}_i(t), t)}{\mathrm{d}t}, \tag{C3}$$

while the terms on the right-hand side are evaluated using cubic spline interpolation (Chian *et al.* 2014; Hang *et al.* 2020). Figure 35 presents the temporal evolution of the material derivative $\mathrm{d}s_1/\mathrm{d}t$ and the individual terms on the right-hand side of (C2). The small discrepancy between the black symbols, representing $\mathrm{d}s_1/\mathrm{d}t$, and the red line, corresponding to the summation of the right-hand side terms (T_{sum}), confirms the validity of (C2).

Next, the governing equation for the rotation rate of eigenvectors $\widetilde{W_{12}} = (\mathrm{d}\boldsymbol{e_2}/\mathrm{d}t)\cdot\boldsymbol{e_1}$ is considered. Since $\widetilde{W_{12}}$ is not directly measurable, the governing equation for $\widetilde{W_{12}}$ in two-dimensional VD SBI,

$$(s_2 - s_1)\,\widetilde{W_{12}} = \widetilde{H_{12}^{p}} + \widetilde{H_{12}^{b}} + \widetilde{H_{12}^{v}}, \tag{C4}$$

cannot be directly validated. However, as $\widetilde{W_{12}}$ appears in SDGE-λ_i (3.10), the validation of (C4) is conducted indirectly by verifying SDGE-λ_i. Specifically, according to the derivation of SDGE-λ_i in the supplementary materials, the verification of SDGE-λ_i is equivalent to validating the governing equation for the projection of the scalar gradient $\widetilde{g_1}^2 = (\nabla Y\cdot\boldsymbol{e_1})^2$, which is given by

$$\frac{\mathrm{d}\widetilde{g_1}^2}{\mathrm{d}t} = -2s_1\widetilde{g_1}^2 - 2\widetilde{W_{12}}\widetilde{g_1}\widetilde{g_2} - \omega\widetilde{g_1}\widetilde{g_2} + 2\widetilde{g_1}\widetilde{T_1^{diff}} = T_{s_1} + T_{\omega} + T_{W_{12}} + T_{others}, \tag{C5}$$

where T_{others} accounts for diffusion effect on scalar gradient alignment, and $\widetilde{W_{12}}$ is computed as

$$\widetilde{W_{12}} = \frac{\widetilde{H_{12}^{p}} + \widetilde{H_{12}^{b}} + \widetilde{H_{12}^{v}}}{s_2 - s_1}. \tag{C6}$$

Figure 36 shows the close agreement between the black symbols, representing $\mathrm{d}g_1^2/\mathrm{d}t$, and the red line, representing the summation of terms on the right-hand side (T_{sum}).

https://doi.org/10.1017/jfm.2025.11051 Published online by Cambridge University Press

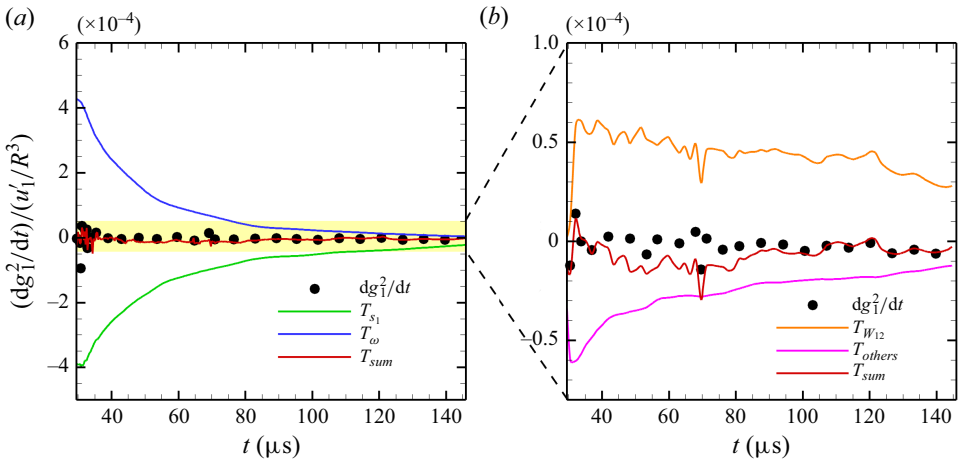


Figure 36. Comparison of the material derivative of the projection of the scalar gradient g_1^2, which is obtained from Lagrangian particle movement results, with the terms in the right side of (C5). Panel (*a*) presents the terms with large magnitude, while (*b*) presents the terms with small magnitude.

This agreement confirms the validity of both (C4) and (C5). Moreover, it is also evident that the diffusion effect on scalar gradient alignment reflected by T_{others} can be nearly neglected.

At this stage, both SDGE-s_i (3.7) and SDGE-λ_i (3.10) in two-dimensional VD SBI have been successfully validated.

References

Ashurst, W.T., Kerstein, A.R., Kerr, R.M. & Gibson, C.H. 1987 Alignment of vorticity and scalar gradient with strain rate in simulated navier–stokes turbulence. *Phys. Fluids* **30** (8), 2343–2353.

Aslangil, D., Livescu, D. & Banerjee, A. 2020 Variable-density buoyancy-driven turbulence with asymmetric initial density distribution. *Phys. D: Nonlinear Phenomena* **406**, 132444.

Batchelor, G.K. 1952 The effect of homogeneous turbulence on material lines and surfaces. *Proc. R. Soc. Lond. Series A.Math. Phys. Sci.* **213** (1114), 349–366.

Batchelor, G.K. 1959 Small-scale variation of convected quantities like temperature in turbulent fluid Part 1. General discussion and the case of small conductivity. *J. Fluid Mech.* **5** (1), 113–133.

Boukharfane, R., Bouali, Z. & Mura, A. 2018 Evolution of scalar and velocity dynamics in planar shock-turbulence interaction. *Shock Waves* **28** (6), 1117–1141.

Brethouwer, G., Hunt, J.C.R. & Nieuwstadt, F.T.M. 2003 Micro-structure and lagrangian statistics of the scalar field with a mean gradient in isotropic turbulence. *J. Fluid Mech.* **474**, 193–225.

Brouillette, M. 2002 The richtmyer-meshkov instability. *Annu. Rev. Fluid Mech.* **34** (1), 445–468.

Buaria, D., Clay, M.P., Sreenivasan, K.R. & Yeung, P.K. 2021 Turbulence is an ineffective mixer when schmidt numbers are large. *Phys. Rev. Lett.* **126** (7), 074501.

Buch, K.A. & Dahm, W.J.A. 1996 Experimental study of the fine-scale structure of conserved scalar mixing in turbulent shear flows. Part 1. sc [gt] 1. *J. Fluid Mech.* **317**, 21–71.

Caulfield, C.P. 2021 Layering, instabilities, and mixing in turbulent stratified flows. *Annu. Rev. Fluid Mech.* **53**, 113–145.

Cetegen, B.M. & Mohamad, N. 1993 Experiments on liquid mixing and reaction in a vortex. *J. Fluid Mech.* **249**, 391–414.

Chian, A.C.-L., Rempel, E.L., Aulanier, G., Schmieder, B., Shadden, S.C., Welsch, B.T. & Yeates, A.R. 2014 Detection of coherent structures in photospheric turbulent flows. *Astrophys. J.* **786** (1), 51.

Cocke, W.J. 1969 Turbulent hydrodynamic line stretching: consequences of isotropy. *Phys. Fluids* **12** (12), 2488–2492.

Corrsin, S. 1953 Remarks on turbulent heat transfer. In *Proceeding of the Thermodynamics Symposium*, pp. 5–30. University of Iowa Iowa City.

https://doi.org/10.1017/jfm.2025.11051 Published online by Cambridge University Press

DANISH, M., SUMAN, S. & GIRIMAJI, S.S. 2016 Influence of flow topology and dilatation on scalar mixing in compressible turbulence. *J. Fluid Mech.* **793**, 633–655.
DIMOTAKIS, P.E. 2005 Turbulent mixing. *Annu. Rev. Fluid Mech.* **37**, 329–356.
DING, J., LIANG, Y., CHEN, M., ZHAI, Z., SI, T. & LUO, X. 2018 Interaction of planar shock wave with three-dimensional heavy cylindrical bubble. *Phys. Fluids* **30** (10), 106109.
DING, J., SI, T., CHEN, M., ZHAI, Z., LU, X. & LUO, X. 2017 On the interaction of a planar shock with a three-dimensional light gas cylinder. *J. Fluid Mech.* **828**, 289–317.
DRESSELHAUS, E. & TABOR, M. 1992 The kinematics of stretching and alignment of material elements in general flow fields. *J. Fluid Mech.* **236**, 415–444.
DUPLAT, J., INNOCENTI, C. & VILLERMAUX, E. 2010 A nonsequential turbulent mixing process. *Phys. Fluids* **22** (3), 035104.
DUPLAT, J. & VILLERMAUX, E. 2008 Mixing by random stirring in confined mixtures. *J. Fluid Mech.* **617**, 51–86.
FERNANDO, H.J.S. 1991 Turbulent mixing in stratified fluids. *Annu. Rev. Fluid Mech.* **23**, 455–493.
GAO, X., BERMEJO-MORENO, I. & LARSSON, J. 2020 Parametric numerical study of passive scalar mixing in shock turbulence interaction. *J. Fluid Mech.* **895**, A21.
GIRIMAJI, S.S. & POPE, S.B. 1990 Material-element deformation in isotropic turbulence. *J. Fluid Mech.* **220**, 427–458.
GUPTA, S., ZHANG, S. & ZABUSKY, N.J. 2003 Shock interaction with a heavy gas cylinder: emergence of vortex bilayers and vortex-accelerated baroclinic circulation generation. *Laser Part. Beams* **21** (03), 443–448.
HAAS, J.-F. & STURTEVANT, B. 1987 Interaction of weak shock waves with cylindrical and spherical gas inhomogeneities. *J. Fluid Mech.* **181**, 41–76.
HAN, X., YU, B. & LIU, H. 2024 Mixing mechanisms in the view of mixing indicators: from passive-scalar mixing to variable-density mixing. *Metasci. Aerospace* **1** (1), 1–37.
HANG, H., YU, B., XIANG, Y., ZHANG, B. & LIU, H. 2020 An objective-adaptive refinement criterion based on modified ridge extraction method for finite-time lyapunov exponent (ftle) calculation. *J. Visual.* **23**, 81–95.
HAWLEY, J.F. & ZABUSKY, N.J. 1989 Vortex paradigm for shock-accelerated density-stratified interfaces. *Phys. Rev. Lett.* **63** (12), 1241.
IGRA, D. & IGRA, O. 2018 Numerical investigation of the interaction between a planar shock wave with square and triangular bubbles containing different gases. *Phys. Fluids* **30** (5), 056104.
JACOBS, J.W. 1992 Shock-induced mixing of a light-gas cylinder. *J. Fluid Mech.* **234**, 629–649.
JIANG, G. & SHU, C. 1996 Efficient implementation of weighted eno schemes. *J. Comput. Phys.* **126** (1), 202–228.
JOSSY, J.P. & GUPTA, P. 2025 Mixing of active scalars due to random weak shock waves in two dimensions. *J. Fluid Mech.* **1007**, A25.
KEE, R.J., RUPLEY, F.M., MEEKS, E. & MILLER, J.A. 1996 Chemkin-iii: a fortran chemical kinetics package for the analysis of gas-phase chemical and plasma kinetics. *Tech. Rep*. No. SAND-96-8216. Sandia National Lab. (SNL-CA).
KIFONIDIS, K., PLEWA, T., SCHECK, L., JANKA, H.-T. & MÜLLER, E. 2006 Non-spherical core collapse supernovae-ii. The late-time evolution of globally anisotropic neutrino-driven explosions and their implications for sn 1987 a. *Astron. Astrophys.* **453** (2), 661–678.
KLEIN, R.I., MCKEE, C.F. & COLELLA, P. 1994 On the hydrodynamic interaction of shock waves with interstellar clouds. 1: nonradiative shocks in small clouds. *Astrophys. J.* **420**, 213–236.
KUCZEK, J.J. & HAINES, B.M. 2023 Simulated impact of fill tube geometry on recent high-yield implosions at the national ignition facility. *Phys. Plasmas* **30** (9), 092706.
KUMAR, S., ORLICZ, G., TOMKINS, C., GOODENOUGH, C., PRESTRIDGE, K., VOROBIEFF, P. & BENJAMIN, R. 2005 Stretching of material lines in shock-accelerated gaseous flows. *Phys. Fluids (1994-present)* **17** (8), 082107.
LAPEYRE, G., HUA, B.L. & KLEIN, P. 2001 Dynamics of the orientation of active and passive scalars in two-dimensional turbulence. *Phys. Fluids* **13** (1), 251–264.
LAPEYRE, G., KLEIN, P. & HUA, B.L. 1999 Does the tracer gradient vector align with the strain eigenvectors in 2d turbulence? *Phys. Fluids* **11** (12), 3729–3737.
LE BORGNE, T., DENTZ, M. & VILLERMAUX, E. 2013 Stretching, coalescence, and mixing in porous media. *Phys. Rev. Lett.* **110** (20), 204501.
LI, Y., WANG, Z., YU, B., ZHANG, B. & LIU, H. 2020 Gaussian models for late-time evolution of two-dimensional shock–light cylindrical bubble interaction. *Shock Waves* **30** (2), 169–184.
LIANG, G., YU, B., ZHANG, B., XU, H. & LIU, H. 2019 Hidden flow structures in compressible mixing layer and a quantitative analysis of entrainment based on lagrangian method. *J. Hydrodyn.* **31** (2), 256–265.

https://doi.org/10.1017/jfm.2025.11051 Published online by Cambridge University Press

LIANG, Y., ZHAI, Z. & LUO, X. 2018 Interaction of strong converging shock wave with sf 6 gas bubble. *Sci. China Phys. Mechan. Astronomy* **61**, 1–9.
LINDL, J.D., MCCRORY, R.L. & CAMPBELL, E.M. 1992 Progress toward ignition and burn propagation in inertial confinement fusion. *Phys. Today* **45** (9), 32–40.
LIU, H.-C., YU, B., CHEN, H., ZHANG, B., XU, H. & LIU, H. 2020 Contribution of viscosity to the circulation deposition in the Richtmyer–Meshkov instability. *J. Fluid Mech.* **895**, A10.
LIU, H., YU, B., ZHANG, B. & XIANG, Y. 2022 On mixing enhancement by secondary baroclinic vorticity in a shock–bubble interaction. *J. Fluid Mech.* **931**, A17.
LIU, X., OSHER, S. & CHAN, T. 1994 Weighted essentially non-oscillatory schemes. *J. Comput. Phys.* **115** (1), 200–212.
MARBLE, F.E. 1985 Growth of a diffusion flame in the field of a vortex. In *Recent Advances in the Aerospace Sciences*, pp. 395–413. Springer.
MARBLE, F.E., ZUKOSKI, E.E., JACOBS, J.W., HENDRICKS, G.J. & WAITZ, I.A. 1990 Shock enhancement and control of hypersonic mixing and combustion. *AIAA paper* 1990–1981.
MESHKOV, E.E. 1969 Instability of the interface of two gases accelerated by a shock wave. *Fluid Dyn.* **4** (5), 101–104.
MEUNIER, P. & VILLERMAUX, E. 2003 How vortices mix. *J. Fluid Mech.* **476**, 213–222.
MÜLLER, B. 2020 Hydrodynamics of core-collapse supernovae and their progenitors. *Living Rev. Comput. Astrophys.* **6** (1), 3.
NIEDERHAUS, J.H.J., GREENOUGH, J.A., OAKLEY, J.G., RANJAN, D., ANDERSON, M.H. & BONAZZA, R. 2008 A computational parameter study for the three-dimensional shock–bubble interaction. *J. Fluid Mech.* **594**, 85–124.
NOMURA, K.K. & POST, G.K. 1998 The structure and dynamics of vorticity and rate of strain in incompressible homogeneous turbulence. *J. Fluid Mech.* **377**, 65–97.
OHKITANI, K. & KISHIBA, S. 1995 Nonlocal nature of vortex stretching in an inviscid fluid. *Phys. Fluids* **7** (2), 411–421.
PENG, G., ZABUSKY, N.J. & ZHANG, S. 2003 Vortex-accelerated secondary baroclinic vorticity deposition and late-intermediate time dynamics of a two-dimensional richtmyer–meshkov interface. *Phys. Fluids (1994-present)* **15** (12), 3730–3744.
PENG, N., YANG, Y., WU, J. & XIAO, Z. 2021*a* Mechanism and modelling of the secondary baroclinic vorticity in the Richtmyer–Meshkov instability. *J. Fluid Mech.* **911**, A56.
PENG, N., YANG, Y. & XIAO, Z. 2021*b* Effects of the secondary baroclinic vorticity on the energy cascade in the Richtmyer–Meshkov instability. *J. Fluid Mech.* **925**, A39.
PETROPOULOS, N., COLM-CILLE, P.C., MEUNIER, P. & VILLERMAUX, E. 2023 Settling versus mixing in stratified shear flows. *J. Fluid Mech.* **974**, R1.
PICONE, J.M. & BORIS, J.P. 1988 Vorticity generation by shock propagation through bubbles in a gas. *J. Fluid Mech.* **189**, 23–51.
RANJAN, D., NIEDERHAUS, J., MOTL, B., ANDERSON, M., OAKLEY, J. & BONAZZA, R. 2007 Experimental investigation of primary and secondary features in high-mach-number shock-bubble interaction. *Phys. Rev. Lett.* **98** (2), 024502.
RANJAN, D., OAKLEY, J. & BONAZZA, R. 2011 Shock-bubble interactions. *Annu. Rev. Fluid Mech.* **43**, 117–140.
RANZ, W.E. 1979 Applications of a stretch model to mixing, diffusion, and reaction in laminar and turbulent flows. *AIChE J.* **25** (1), 41–47.
RAYLEIGH Investigation of the character of the equilibrium of an incompressible heavy fluid of variable density, *Proc. Lond. Math. Soc.* **1** (1), 170–177.
RICHTMYER, R.D. 1960 Taylor instability in shock acceleration of compressible fluids. *Commun. Pure Appl. Math.* **13** (2), 297–319.
SAFFMAN, P.G. 1970 The velocity of viscous vortex rings. *Stud. Appl. Math.* **49** (4), 371–380.
SANDOVAL, D.L. 1995 The dynamics of variable-density turbulence. PhD thesis, University of Washington.
SHARIFF, K. & LEONARD, A. 1992 Vortex rings. *Annu. Rev. Fluid Mech.* **24** (1), 235–279.
SHE, Z.-S., JACKSON, E. & ORSZAG, S.A. 1991 Structure and dynamics of homogeneous turbulence: models and simulations. *Proc. R. Soc. Lond. Series A: Math. Phys. Sci.* **434** (1890), 101–124,
SOUZY, M., ZAIER, I., LHUISSIER, H., LE BORGNE, T. & METZGER, B. 2018 Mixing lamellae in a shear flow. *J. Fluid Mech.* **838**.
SWAMINATHAN, N. & GROUT, R.W. 2006 Interaction of turbulence and scalar fields in premixed flames. *Phys. Fluids* **18** (4), 045102.
TAYLOR, G.I. 1950 The instability of liquid surfaces when accelerated in a direction perpendicular to their planes. i. *Proc. R. Soc. Lond. Series A. Math. Phys. Sci.* **201**(,1065), 192–196.

https://doi.org/10.1017/jfm.2025.11051 Published online by Cambridge University Press

TIAN, Y., JABERI, F.A., LI, Z. & LIVESCU, D. 2017 Numerical study of variable density turbulence interaction with a normal shock wave. *J. Fluid Mech.* **829**, 551–588.
TIAN, Y., JABERI, F.A. & LIVESCU, D. 2019 Density effects on post-shock turbulence structure and dynamics. *J. Fluid Mech.* **880**, 935–968.
TOM, J., CARBONE, M. & BRAGG, A.D. 2021 Exploring the turbulent velocity gradients at different scales from the perspective of the strain-rate eigenframe. *J. Fluid Mech.* **910**, A24.
TOMKINS, C., KUMAR, S., ORLICZ, G. & PRESTRIDGE, K. 2008 An experimental investigation of mixing mechanisms in shock-accelerated flow. *J. Fluid Mech.* **611**, 131–150.
TOWNSEND, A.A. 1951 The diffusion of heat spots in isotropic turbulence. *Proc. R. Soc. Lond. Series A. Math. Phys. Sci.* **209**(,1098), 418–430.
VILLERMAUX, E. 2019 Mixing versus stirring. *Annu. Rev. Fluid Mech.* **51**, 245–273.
VILLERMAUX, E. & DUPLAT, J. 2003 Mixing is an aggregation process. *C. R. Méc.* **331** (7), 515–523.
VINCENT, A. & MENEGUZZI, M. 1991 The spatial structure and statistical properties of homogeneous turbulence. *J. Fluid Mech.* **225**, 1–20.
WADAS, M., LEFEVRE, H., ELMORE, Y., XIE, X., WHITE, W., KURANZ, C. & JOHNSEN, E. 2024 Feasibility of an experiment on clumping induced by the crow instability along a shocked cylinder. *Phys. Plasmas* **31** (6), 062103.
WADAS, M.J., KHIEU, L.H., CEARLEY, G.S., LEFEVRE, H.J., KURANZ, C.C. & JOHNSEN, E. 2023 Saturation of vortex rings ejected from shock-accelerated interfaces. *Phys. Rev. Lett.* **130** (19), 194001.
WANG, Z., YU, B., CHEN, H., ZHANG, B. & LIU, H. 2018 Scaling vortex breakdown mechanism based on viscous effect in shock cylindrical bubble interaction. *Phys. Fluids* **30** (12), 126103.
WARHAFT, Z. 2000 Passive scalars in turbulent flows. *Annu. Rev. Fluid Mech.* **32** (1), 203–240.
WUNSCH, C. & FERRARI, R. 2004 Vertical mixing, energy, and the general circulation of the oceans. *Annu. Rev. Fluid Mech.* **36** (1), 281–314.
YAN, Z., CHEN, Z., LI, Z., WU, J., FAN, Z., YU, C., LI, X. & WANG, L. 2025 The role of double-layer vortex rings with the local swirl in the rapid transition to turbulent flows in richtmyer–meshkov instability with reshock. *J. Fluid Mech.* **1003**, A36.
YANG, J., KUBOTA, T. & ZUKOSKI, E.E. 1993 Applications of shock-induced mixing to supersonic combustion. *AIAA J.* **31** (5), 854–862.
YANG, J., KUBOTA, T. & ZUKOSKI, E.E. 1994 A model for characterization of a vortex pair formed by shock passage over a light-gas inhomogeneity. *J. Fluid Mech.* **258**, 217–244.
YU, B., HE, M., ZHANG, B. & LIU, H. 2020 Two-stage growth mode for lift-off mechanism in oblique shock-wave/jet interaction. *Phys. Fluids* **32** (11), 116105.
YU, B., LI, L., XU, H., ZHANG, B. & LIU, H. 2022 Effects of Reynolds number and schmidt number on variable density mixing in shock bubble interaction. *Acta Mech. Sinica* **38** (6), 121256.
YU, B., LIU, H. & LIU, H. 2021 Scaling behavior of density gradient accelerated mixing rate in shock bubble interaction. *Phys. Rev. Fluids* **6** (6), 064502.
ZABUSKY, N.J. & ZENG, S.M. 1998 Shock cavity implosion morphologies and vortical projectile generation in axisymmetric shock–spherical fast/slow bubble interactions. *J. Fluid Mech.* **362**, 327–346.
ZENG, W.-G., PAN, J.-H., REN, Y.-X. & SUN, Y.-T. 2018 Numerical study on the turbulent mixing of planar shock-accelerated triangular heavy gases interface. *Acta Mech. Sinica* **34** (5), 855–870.
ZHAI, Z., WANG, M., SI, T. & LUO, X. 2014 On the interaction of a planar shock with a light polygonal interface. *J. Fluid Mech.* **757**, 800–816.
ZHANG, B., LIU, H., YU, B., WANG, Z., HE, M. & LIU, H. 2022 Numerical investigation on combustion-enhancement strategy in shock–fuel jet interaction. *AIAA J.* **60** (1), 393–410.
ZHANG, W., ZOU, L., ZHENG, X. & WANG, B. 2019 Numerical study on the interaction of a weak shock wave with an elliptic gas cylinder. *Shock Waves* **29** (2), 273–284.
ZHAO, S., ER-RAIY, A., BOUALI, Z. & MURA, A. 2018 Dynamics and kinematics of the reactive scalar gradient in weakly turbulent premixed flames. *Combust. Flame* **198**, 436–454.
ZHOU, Y. 2017*a* Rayleigh–taylor and richtmyer–meshkov instability induced flow, turbulence, and mixing. ii. *Phys. Rep.* **723**, 1–160.
ZHOU, Y. 2017*b* Rayleigh–taylor and richtmyer–meshkov insta*b*ility induced flow, turbulence, and mixing. i. *Phys. Rep.* **720-722**, 1–136.

https://doi.org/10.1017/jfm.2025.11051 Published online by Cambridge University Press